CENTRO DE INVESTIGACIÓN Y DE ESTUDIOS AVANZADOS DEL INSTITUTO POLITÉCNICO NACIONAL

UNIDAD MÉRIDA

DEPARTAMENTO DE FÍSICA APLICADA

Caracterización óptica de películas delgadas de absorción y emisión selectiva, basadas en óxidos metàlicos de Ni, Ti y V, mediante el uso de espectroscopía fototérmica y elipsometría

Tesis que presenta

Jorge Andrés Ramírez Rincón

Para obtener el grado de

Doctor en Ciencias

en la especialidad de Física Aplicada

Directores

Dr. Juan José Alvarado Gil

Dr. Oscar Eduardo Arés Muzio

Mérida, Yucatán, México.   Junio 2019

CENTRO DE INVESTIGACIÓN Y DE ESTUDIOS AVANZADOS DEL INSTITUTO POLITÉCNICO NACIONAL

UNIDAD MÉRIDA

DEPARTMENT OF APPLIED PHYSICS

Optical characterization of selective absorber and emitter thin films based on metal oxides of Ni, Ti and V using photothermal and ellipsometric spectroscopies.

Thesis presented by

Jorge Andrés Ramírez Rincón

To obtain the title of

Doctor of Science

in the speciality of Applied Physics

Supervised by

Dr. Juan José Alvarado Gil

Dr. Oscar Eduardo Arés Muzio

Mérida, Yucatán, México.   June 2019

Para Martín.

Agradecimientos

A mi madre y a mi hermana por su apoyo incondicional en este proceso.

A mi esposa Lorena, por compartir conmigo esta aventura.

A mi hijo Martín, que desde su inocencia me fortaleció para intentar ser cada día mejor.

A mis directores de tesis, Dr. Juan José Alvarado y Dr. Oscar Ares Muzio por su apoyo, enseñanzas y valiosos aportes durante mi estancia en el Cinvestav.

Al Dr. José Ordóñez por su invaluable asesoría para el buen término de mis estudios de doctorado.

A los miembros de Institut Pprime en la Univeritè de Poitiers, por su apoyo durante nuestra estancia.

A todos los miembros del laboratorio de Espectroscopia Óptica y Térmica, por su amistad y ayuda diaria.

Al grupo de nanomateriales del Cinvestav-IPN unidad Mérida, lidereado por el Dr. Gerko Oskam, por la elaboración de muchas de las muestras analizadas en este trabajo.

Al departamento de Física Aplicada por hacer de este lugar nuestro hogar.

Resumen

La caracterización de películas delgadas es uno de los más grandes retos de la física experimental actual. Una gran variedad de fenómenos físicos ocurre en estos sistemas, los cuales ocurren a la microescala y nanoescala, involucrando comportamiento clásico y cuántico simultáneamente. Este tipo de estructuras son la base de los desarrollos en electrónica, optolectrónica y de la industria energética para la conversión, almacenamiento y manejo de diversas fuentes de energía, y en particular de la energía térmica. En este trabajo se presentan dos metodologías experimentales relacionadas con las técnicas de espectroscopia fototérmica y elipsometría, utilizadas para la caracterización óptica de óxidos metálicos de absorción y emisión selectiva.

En la primera parte, la conocida teoría de Rosencwaig-Gersho para el campo de ondas térmicas, es utilizada para resolver la ecuación de conducción de calor en coordenadas cilíndricas mediante el uso de la transformada de Hankel, considerando como fuente de calor un láser gaussiano. A partir de simulaciones del modelo matemático para propagación 3D y 1D del calor, se encontró que las películas delgadas depositadas sobre sustratos gruesos introducen efectos puramente ópticos (absorción y emisión) en las señales fototérmicas. Por lo tanto, estos modelos junto con las técnicas de radiometría fototérmica y espectroscopia fotoacústica, PTR y PAS por sus siglas en inglés respectivamente, son utilizadas para obtener experimentalmente la eficiencia de conversión de luz en calor y la emisividad de recubrimientos solares basados en electrodepósitos delgados de óxido de níquel - níquel en acero inoxidable y cobre, y el recubrimiento comercial TiNOX de la marca Almeco, depositado en aluminio. Con esto se demuestra que la combinación de PTR y PAS puede dar valores para la emisividad que concuerdan con los obtenidos usando la espectroscopia infrarroja por transformada de Fourier (FTIR).

En la segunda parte del trabajo, la técnica de radiometría se usa para analizar las señales de fase de los sustratos metalicos en el régimen de propagación de calor 3D, las cuales se han visto modificadas por efectos ópticos anómalos introducidos por los recubrimientos selectivos. Este comportamiento también se observa en mediciones en tiempo real de la transision estructural de películas delgadas de dióxido de vanadio (VO_2) depositadas sobre zafiro, y se asocia a

efectos de dispersión en la emisión infraroja de la superficie, los cuales, basados en análisis SEM, dependen fuertemente de la morfología estructural y composición de la película depositada. En el caso de VO_2, esto además se ascocia a la coexistencia de dominios aislantes y metálicos durante la transicion de fase, por lo tanto, la caracterización óptica de este material se realizó mediante el uso de elipsometría espectroscópica.

La parte real e imaginaria de la función dieléctrica de películas delgadas de VO_2 depositadas en zafiro plano-r y plano-c mediante la técnica de depósito por láser pulsado (PLD), son obtenidas usando elipsometría en el rango de longitudes de onda de 0.4 a 15 μm y temperaturas dentro de su transición de fase. Tanto en la transición de aislante a metal (calentamiento) como metal a aislante (enfriamiento), se muestra que las dos señales elipsométricas tienen tres comportamientos diferentes a medida que cambia la temperatura de la muestra. Estos comportamientos se pueden describir de buena forma con la combinación apropiada de los modelos de oscilador de Tauc-Lorentz, Gauss y Drude. Ajustando el modelo de medio efectivo de Bruggeman para la función dieléctrica, junto con los valores obtenidos experimentalmente, y usando como parámetro la fracción volumétrica de metal dentro de la muestra para cada valor de temperatura, se encontró que este modelo es útil para describir la función dieléctrica espectral del rango visible al infrarrojo cercano (~0.4 a ~3.0 μm), pero generalmente falla para longitudes de onda más largas. Además, se determina el ciclo de histéresis del VO_2 para la emisividad promedio sobre un intervalo amplio de longitudes de onda, con una variación desde 0.49, desde el estado aislante, a 0.16 en el metálico. Estos valores, basados en los resultados para la función dieléctrica, concuerdan con mediciones previas reportadas en la literatura.

Abstract

Characterization of thin films is one of the great challenges in modern experimental physics. A large variety of physical phenomena occurs in those systems, involving simultaneously classical and quantum behavior. This type of structures forms the basis for electronics, optoelectronics and, in the energy industry, for conversion, storage and management of diverse energy sources, particularly thermal energy. In this work, two methodologies are presented, which involve photothermal and ellipsometry spectroscopic techniques, for the optical characterization of the absorption and selective thermal emission properties of metal oxides.

In the first part, the well-known Rosencwaig-Gersho theory of thermal wave fields, is used to solve the heat conduction equation in cylindrical coordinates considering an incident Gaussian laser beam, by using the Hankel transform. Based on simulations of the mathematical model for 3D and 1D heat propagation, it is shown that thin films deposited on thick substrates introduce purely optical effects in the photothermal signals. Therefore, these models along with photothermal radiometry (PTR) and photoacoustic spectroscopy (PAS) techniques are used to obtain experimentally the light-into-heat conversion efficiency and emissivity of solar selective coatings based on electrodeposited nickel oxide - nickel thin films on both stainless steel and copper substrates, as well as commercial TiNOX coatings on aluminum. We show that a combination of PTR and PAS can successfully provide values for the emissivity that are in agreement with values obtained by Fourier transform infrared spectroscopy.

In the second part of the work, the PTR technique is used to analyze anomalous optical effects induced by selective coatings deposited on metallic substrates, on the phase of the PTR signals considering a 3D heat propagation regime. This behavior has also been observed during real time monitoring of structural transition of vanadium dioxide (VO_2) thin films deposited on sapphire substrates, which can be associated to effects of scattered emission. These effects depend strongly on the morphology and composition of the deposited layer, in which dielectric and metallic domains coexist across the metal-to-insulator transition.

The real and imaginary parts of the dielectric function of VO_2 thin films, deposited on r-plane and c-plane sapphire via pulsed laser deposition, are measured by means of visible-IR

ellipsometry for wavelengths ranging from 0.4 to 15 μm and temperatures within its phase transition. For both the insulator-to-metal (heating) and metal-to-insulator (cooling) transitions, it is shown that the two ellipsometric signals exhibit three temperature-driven behaviors, which are well described by appropriate combinations of the Tauc-Lorentz, Gaussian, and Drude oscillator models. By fitting Bruggeman's effective medium model for the dielectric function to the corresponding measured experimental values, using the volumetric fraction of the VO_2 metallic domains as a fitting parameter for different temperatures within the VO_2 phase transition, we have found that this model is suitable for describing the dielectric function in visible and near-infrared wavelengths (~0.4 to ~3.0 μm), but it generally fails for longer infrared ones. Furthermore, the hysteresis loop of the VO_2 emissivity, averaged over a relevant interval of wavelengths, is determined and shown to vary from ~0.49, in the insulator phase, to ~0.16, in the metallic phase. These values, based on the VO_2 dielectric function, are consistent with previous measurements reported in the literature.

Index

Introduction

The characterization of materials by means of non-invasive methods has been developed based on robust theoretical and experimental methodologies since the middle of the twentieth century. The optimization of these techniques has generated substantial progress for its use under extreme environmental conditions, as well as to obtain optical, electrical and thermal properties of composed materials, nano-structured and thin films. Additionally, the technological advances have allowed the development of electronic devices of high accuracy, which have been increasing the utility of the classic techniques to obtain new information on the latest generation materials.

Based on the work developed by Rosencgwaig and Gersho in 1970's about the propagation of heat in materials, photothermal techniques have been consolidated as a good alternative to characterize the thermal and optical properties of solids. They introduced the concept of thermal wave to associate the light-into-heat conversion in a surface illuminated with an energy flux, and the heat propagation through it. This theory along with the work developed in the following years, opened a research field known today as photothermal spectroscopy, in which the photothermal radiometry (PTR) and photoacoustic spectroscopy (PAS) are some of the most useful techniques, due to its versatility to monitoring in real time the evolution of structural, optical, and thermal properties of different types of materials.

Photothermal radiometry consists in the measurement of changes of the light emitted by a surface, when it is heated up with a modulated heat source (regularly a laser). The direct dependence of the infrared emission on the surface emissivity, can allow using this technique to optically characterize selective coatings with application in solar energy industry. Additionally, PTR has been used to obtain the thermal diffusivity and thermal conductivity of

resins, solid thick layers and composite materials. On the other hand, photoacoustic spectroscopy measures the pressure changes of a gas layer in thermal contact with a surface heated up by means of a modulated heat source. It has been widely used to obtain the thermal properties of liquids and solids, as well its spectral absorption, and could also provide the light into-heat conversion efficiency.

The optical properties, obtained by means of the photothermal techniques, are mainly associated to processes of optical absorption, light-into-heat conversion (visible spectra) and thermal emission. Those proceses can also be partially analized using conventional optical spectroscopy. Therefore, the combination of optical and photothermal methodologies arises as a good alternative in the optical characterization of complex thin film samples, like those presenting absorption bands and/or structural changes.

Spectroscopic ellipsometry is a technique widely used to obtain structural and optical characteristics of dielectric materials, metals and semiconductors. Ellipsometry is based on the fact that the light reflected by a surface changes its polarization from linear to elliptical, after an oblique incidence. These changes can be associated to the surface properties through multilayer optical models, which describe the interaction of the incident light with the sample. Therefore, ellipsometry can be assumed as the optical equivalent of photothermal techniques. The usefulness of both spectroscopies will be explored in this document.

The main objective of this work is the characterization of thin films deposited on dielectric and metallic substrates. To achieve this goal, photothermal spectroscopy and ellipsometry are used and their results are analyzed independently to determine the dependence of each technique on the thermal and optical properties of solar energy coatings and vanadium dioxide thin films.

In chapter 1, the theoretical photothermal and optical principles, on which the present work is based are detailed and summarized.

In chapter 2, the heat conduction equation is solved taking into account the effects of three-dimensional heat propagation induced by a heat source of Gaussian profile. These results are compared with the one-dimensional solution, and the effects of thin films on the photothermal signals are evaluated.

In chapter 3, metal oxide thin films of high absorption coefficient across the solar radiation spectrum and a very low emission in the infrared range (solar selective coatings), deposited on substrates of high and low thermal diffusivity, are optically characterized combining the PTR and PAS techniques.

In the chapter 4, photothermal radiometry signals and SEM micrographs are used to analyze the thermal profiles of samples with internal structures and non-homogeneous composition, such as polyester resin, solar selective coatings and VO_2 thin films.

Finally, in chapter 5 the spectroscopic ellipsometry technique is used to obtain the dielectric function of two vanadium dioxide thin films in the spectral range of 0.4 to 15 μm. From these results, the volumetric metallic fraction in the sample has been calculated. This was done along the semiconductor metal phase transition by using the effective medium theory, and the emissivity through Kirchhoff's law.

1. Theoretical Framework

1.1. Photothermal spectroscopy

Photothermal techniques are based on generation and heat transfer in a material, governed by processes of light-into-heat conversion when the surface is illuminated and heated up by an energy source. A. Rosencwaig and A. Gersho in 1976 introduced the concept of thermal wave (TW), which represents spatial-temporal oscillations of the temperature generated by a modulated energy source, to solve the conduction heat transfer equation shown in Eq. (1.1), which describes heat diffusion in terms of the thermal and optical properties of the material [1].

$$\nabla^2 \theta(r,t) - \frac{1}{\alpha} \frac{\partial \theta(r,t)}{\partial t} = -\frac{Q(r,t)}{k}, \tag{1.1}$$

Where k [Wm^{-1}K^{-1}] is the thermal conductivity, related to the amount of energy transferred, and α [m^{2}s^{-1}] is the thermal diffusivity and represents the velocity of the heat transfer. $Q(r,t)$ is the heat energy source [Wm^{-2}] and $\theta(r,t)$ [K] is the modulated temperature, which has a dependence on the spatial coordinates (r) and time (t).

Several theoretical and experimental studies based on the Rosencwaig and Gersho theory [2,3,4] have reported the usefulness of the photothermal techniques for the thermal and optical characterization of different materials [5,6,7]. This work will be focused in the use of

photothermal radiometry (PTR) and photoacoustic spectroscopy (PAS) for the optical characterization of thin films [8,9,10], with applications in clean energy generation systems.

1.1.1. Photothermal Radiometry (PTR)

This technique is based on the measurement of the infrared radiation emitted by a surface heated by an oscillatory heat source. The modulated component of the temperature is related with the emission of the surface trough the Stefan Boltzmann law, which establishes that any material at temperature $T > 0\ K$ will emit electromagnetic radiation whose emitted power is given by

$$W = \epsilon \sigma_B T^4,$$
(1.2)

where ϵ is the emissivity of the surface (for a black body $\epsilon = 1$), σ_B [Wm^{-2}K^{-4}] the Stefan-Boltzmann constant and T [K] the surface`s absolute temperature. Moreover, the spectral distribution of the electromagnetic radiation emitted, has a dependence on the temperature T [K] through the Wien law given by

$$\lambda = 2897.6\ /T,$$
(1.3)

where λ [μm] is the wavelength of the emitted radiation, which has a maximum value of around 10 μm at 300 K.

Considering a small change of the sample temperature by means of a modulated heat source, the changes of the power emitted by the surface (ΔW) at temperature T are given by [9]

$$\Delta W = 4\epsilon \sigma_B (T + \theta_{dc})^3 \theta,$$
(1.4)

where θ_{dc} is the non-modulated increase of the temperature, calculated experimentally to be less than 3 K [8], and θ is the modulated temperature, which dependence on the optical and thermal properties is given by solving Eq. (1.1).

1.1.2. Photoacoustic Spectroscopy (PAS)

Photoacoustic spectroscopy is based on the fact that the periodic heating of a sample also generates changes in the temperature of the surrounding medium (normally air), producing a periodic expansion of the air layer in contact with the surface of the sample. This effect is known as thermal piston (see Fig. 1.1). According to Rosencwaig and Gersho theory [2], the displacement of the air layer is given by

$$\Delta x = \frac{\mu_{air}}{\sqrt{2}} \frac{\theta}{(T + \theta_{dc})},$$

(1.5)

where $\mu_{air} = \sqrt{\alpha_{air}/\pi f}$ [m] is the thermal diffusion length, which represents the distance traveled by the TW before being attenuated. In this case, the thermal diffusivity of the air is α_{air} (2.26 $\times 10^{-5}$ m^{2}s^{-1}) [11], and f is the modulation frequency of the heat source.
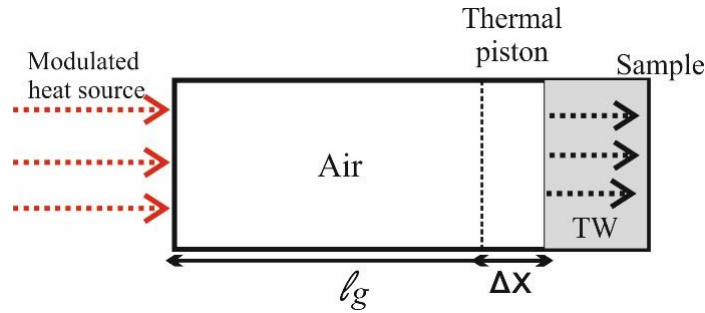
Fig. 1.1. Scheme of the basic Rosencgwaig photoacoustic cell.

Considering an adiabatic interaction between the thermal piston and the gas (air) that fills up the cell, a small change in the pressure, according with the relation $PV^{\gamma} = cte$ [2], is given by

$$\Delta P = \gamma \frac{P_0}{V_0} \Delta V,$$

(1.6)

where P_0 and V_0 are the initial pressure and volume of the cell, and γ is the ratio of specific heat.

If the spot of the laser illuminates all the surface of the sample in contact with air, and $\mu_{air} \gg l_g$ (length of the cell), the TW will propagate almost perpendicularly to the surface (one-dimensional), then Eq. (1.6) reduces to

$$\Delta P = \gamma \frac{P_0}{l_g} \Delta x, \tag{1.7}$$

Therefore, the changes of pressure inside the photoacoustic cell, in terms of the properties of the illuminated sample, are obtained combining Eq. (1.5) and Eq. (1.7).

$$\Delta P = \gamma \frac{P_0}{l_c} \frac{\mu_{air}}{\sqrt{2}} \frac{\theta}{(T + \theta_{dc})} \tag{1.8}$$

Eqs. (1.4) and (1.8) for the PTR and PAS techniques respectively, allow to relate the experimentally measured quantities, with the thermal and optical properties of a sample using the modulated temperature θ, which is solution of the heat conduction equation shown in Eq. (1.1).

1.2. Spectroscopic Ellipsometry

Spectroscopic Ellipsometry is a non-invasive and non-destructive measurement technique used to determine the optical properties of a sample by means of polarized light. The method basically measures the relative change in the polarization state of incident light beam when it is reflected by a surface [12]. At sufficiently small power of the incident light, in a large variety of materials, this methodology does not depend on the intensity of the incident light, making the measurements highly accurate and reproducible.
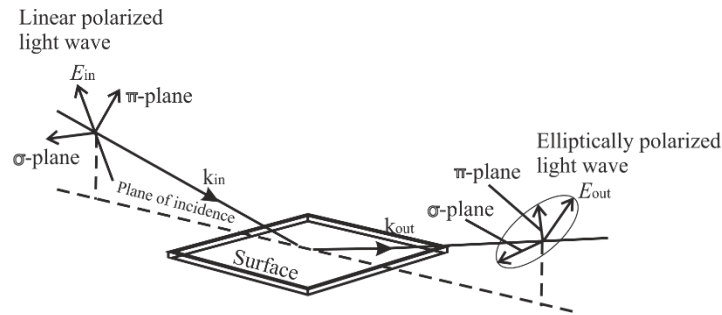
Fig. 1.2. Scheme of the ellipsometry principle for oblique incidence of linearly polarized light, and its reflection becoming elliptically polarized. Imagen adapted from Ref [13].

The plane of incidence of the incident (reflected) electromagnetic radiation is defined as the plane perpendicular to the sample surface, which contains the vector $\mathbf{k_{in}}$ ($\mathbf{k_{out}}$) that represents the direction of propagation of light, while the electric field $\mathbf{E_{in}}$ ($\mathbf{E_{out}}$) is chosen as the vector that defines its polarization (see Fig. 1.2) [14]. The $\mathbf{E}$-vector has two components $\mathbf{E_\pi}$ and $\mathbf{E_\sigma}$ named according to Greek symbols for the words "Parallel" π and "Senkrecht" σ in German, that represent the parallel and perpendicular components. These components are perpendicular between them and to the $\mathbf{k}$-vector.

The electric field vector of the incident light ($\mathbf{E_{in}}$), because of its linear polarization, moves in a straight line in the plane of the π and σ components. After reflection, the polarization state change to elliptical, which modifies $\mathbf{E_\pi}$ and $\mathbf{E_\sigma}$ causing that $\mathbf{E_{out}}$ moves in an ellipse.

As is shown in Fig. 1.2, ellipsometry uses the fact that linearly polarized light at an oblique incidence to a surface, changes its polarization state to elliptical one after the reflection, thereby the name "ellipsometry". The angles Ψ and Δ are defined as the ellipsometric parameters that describe the spectral behavior of the reflected light. In the next section it be will be shown how these quantities can be related with the optical properties of the sample.

1.2.1.   Ellipsometry parameters: Ψ and Δ

The factor ρ is defined as the ratio between the components of the electric field ($\mathbf{E_\pi}$ and $\mathbf{E_\sigma}$) of the incident (in) and reflected (out) light [14]

$$\frac{\rho_{in}}{\rho_{out}} = \frac{\frac{E_{in,\sigma}}{E_{in,\pi}}}{\frac{E_{out,\sigma}}{E_{out,\pi}}}, \qquad (1.9a)$$

$$\frac{\rho_{in}}{\rho_{out}} = \frac{E_{in,\sigma}E_{out,\pi}}{E_{in,\pi}E_{out,\sigma}}. \qquad (1.9b)$$

By means of the Jones vector ($E_q = A_q e^{j\phi_q}$) [15], the electric field vector of Eq. (1.9b) can be rewritten as

$$\frac{\rho_{in}}{\rho_{out}} = \frac{A_{in,\sigma}\, e^{j\phi_{in,\sigma}}}{A_{in,\pi}e^{j\phi_{in,\pi}}} \frac{A_{out,\pi}e^{j\phi_{out,\pi}}}{A_{out,\sigma}e^{j\phi_{out,\sigma}}}, \qquad (1.10)$$

where A_q and ϕ_q represents the q-component of the amplitude and phase respectively.

For an incident linearly polarized light beam, $A_{in,\sigma} = A_{in,\pi}$ and $\phi_{in,\sigma} = \phi_{in,\pi}$, therefore Eq. (1.10) reduces to

$$\frac{\rho_{in}}{\rho_{out}} = \rho = \frac{A_{out,\pi}}{A_{out,\sigma}} e^{j(\phi_{out,\pi} - \phi_{out,\sigma})}. \qquad (1.11)$$
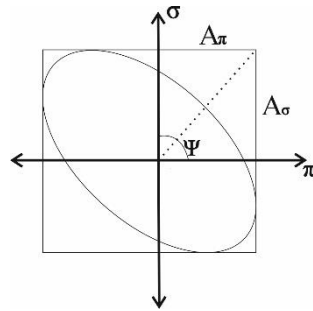
Fig. 1.3. Geometrical scheme of the electric field amplitude, for elliptically polarized light.

For elliptical polarization, the ratio between the amplitudes of each component of the electric field, based on Fig. 1.3, can be written as $\tan(\Psi) = A_{out,\pi}/A_{out,\sigma}$, therefore Eq. (1.11) becomes,

$$\rho = \tan(\Psi)\, e^{j\Delta}, \tag{1.12}$$

where $\Delta = \phi_{out,\pi} - \phi_{out,\sigma}$ is the difference of phase between the components of the reflected electric field.

The Eq. (1.12) is known as the general ellipsometry equation [12,13], which relates the ratio between the components of the incident and reflected electric field, with the ellipsometry parameters Ψ and Δ.

On the other hand, the Fresnel reflection coefficients relates de amplitude of the incident and reflected electric field, for the parallel and perpendicular components as follows,

$$\frac{E_{out,\pi}}{E_{out,\sigma}} = \frac{\tilde{n}_1 \cos\varphi_0 - \tilde{n}_0 \cos\varphi_1}{\tilde{n}_0 \cos\varphi_0 - \tilde{n}_1 \cos\varphi_1}, \tag{1.13}$$

where $\tilde{n}_1$ ($\tilde{n}_0$) is the complex refraction index of incident (transmitted) medium and φ_0 (φ_1) is the incident (transmission) angle of the light beam.

Comparing Eq. (1.9a) and Eq. (1.13) with Eq. (1.12), the ellipsometry parameters are related with the optical properties of the sample by

$$\tan(\Psi)\, e^{j\Delta} = \frac{\tilde{n}_1 \cos\varphi_0 - \tilde{n}_0 \cos\varphi_1}{\tilde{n}_0 \cos\varphi_0 - \tilde{n}_1 \cos\varphi_1}. \tag{I.14}$$

The parameters Ψ and Δ contains all the information of the optical properties of the layers that compose the sample (see Fig. 1.4), as well as the process of interaction light-matter, which varies dramatically wih the type of material (dielectric, semiconductor, metal, polymer, etc.) and the spectral range considered (UV, Visible, NIR, IR, etc.) [16,17,18]. Therefore, in order to obtain the right optical parameters of thin films, the correct interpretation of ellipsometry signals require the use of optical multilayers models.
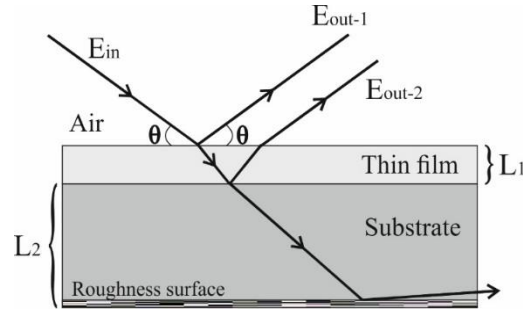
Fig. 1.4. Scheme of a typical sample formed by a thin layer of thickness L1 on a substrate of thickness L2 with a rough back surface. The trayectory of the light due to reflection, transmission and scattering is indicated.

1.2.2. Optical constants

The dielectric function (ε) describes the material's response to electromagnetic radiation, i.e. the processes that control the absorption and reemission when a surface is illuminated with a light source. The relation between the ε and the complex refraction index $\tilde{n}$ of Eq. (1.14) is given by [19]

$$\tilde{n}(\lambda) = \sqrt{\varepsilon(\lambda)} \tag{1.15a}$$

$$\tilde{n}(\lambda) = n(\lambda) + ik(\lambda) = \sqrt{\varepsilon_R(\lambda) + i\varepsilon_I(\lambda)} \tag{1.15b}$$

$$\varepsilon_R(\lambda) = n^2(\lambda) - k^2(\lambda) \tag{1.15c}$$

$$\varepsilon_I(\lambda) = 2n(\lambda)k(\lambda), \tag{1.15d}$$

where n and k are the refractive index and extinction coefficient, and ε_R, ε_I the real and imaginary part of the dielectric function, respectively; λ represents the spectral dependence of these properties.

The most common optical models to describe the interaction light-matter will be shown below. The mathematical steps to obtain these is out side of the objectives of this work; however, its use along with the experimental values of Ψ and Δ to calculate the optical constants (n y k) will be studied in detail in chapter 5.

1.2.3. Tauc-Lorentz oscillator

Jellison and Modine developed the Tauc-Lorentz (TL) model in 1996 using the Tauc joint density of states and the Lorentz oscillator to describe the optical properties of amorphous films [13]. The imaginary part of the dielectric function is given by

$$\varepsilon_I(E) = \frac{1}{E} \frac{AE_0B(E - E_g)^2}{(E^2 - E_0^2)^2 + C^2E^2},$$ (1.16)

where A is the amplitude (oscillator strength), E_0 the peak central energy, B the broadening of the amplitude term, C is the broadening term of the peak and E_g the optical band gap. Notice that Eq. (1.16) is a function of the photon energy (E), which is related with the wavelength (λ) through Planck's constant and the vacuum light velocity by $E = hc/\lambda$.

The real part of the dielectric function is derived from the expression of $\varepsilon_I(E)$ by using the Kramers-Kronig (KK) integration formula [17]:

$$\varepsilon_R(E) = \varepsilon_I(\infty) + \frac{2P}{\pi} \int_{E_g}^{\infty} \frac{\xi \cdot \varepsilon_I(\xi)}{\xi^2 - E^2} d\xi,$$ (1.17)

where P is the Cauchy principal part of the integral, and the parameters A, E_0, B, E_g and $\varepsilon_R(\infty)$ can be obtained by fitting to the experimental data.

1.2.4. Drude oscillator model

The classical Drude model based on the kinetic theory for electrons in a metal describes free carrier effects on the dielectric function response. It was constructed in order to explain the transport properties of conduction electrons due to intra-band transitions, in metals, conductive oxides and heavily doped semiconductors [20,21]

$$\varepsilon_{Drude}(E) = \frac{-\hbar^2}{\varepsilon_0\rho(\tau E^2 + i\hbar E)}.$$ (1.18)

The Drude model of Eq. (1.18) is equivalent to the Lorentz oscillator when the center energy is equal to zero. It depends on Planck's constant ($\hbar$), vacuum dielectric constant (ε_0) and the fitting parameters: resistivity (ρ) and scattering time (τ).

References

[1] Almond, D. P., & Patel, P. M. (1996). Photothermal Science and Techniques in Physics and its Applications vol 10, ed ER Dobbs and SB Palmer.

[2] Rosencwaig, A., & Gersho, A. (1976). Theory of the photoacoustic effect with solids. *Journal of Applied Physics*, *47*(1), 64-69.

[3] Helander, P., Lundström, I., & McQueen, D. (1980). Light scattering effects in photoacoustic spectroscopy. *Journal of Applied Physics*, *51*(7), 3841-3847.

[4] Mandelis, A. (2013). Green Functions of One-Dimensional Thermal-Wave Fields. In *Diffusion-wave fields: mathematical methods and Green functions*. Springer Science & Business Media.

[5] Vales-Pinzon, C., Ordonez-Miranda, J., & Alvarado-Gil, J. J. (2012). Photothermal characterization of the thermal properties of materials using four characteristic modulation frequencies in two-layer systems. *Journal of Applied Physics*, *112*(6), 064909.

[6] Zambrano-Arjona, M. A., Ordonez-Miranda, J., Medina-Esquivel, R. A., Penunuri, F., Martinez, P., & Alvarado-Gil, J. J. (2012). Effect of the multiple reflections of a light beam on the thermal wave field of a sample of finite thickness. *Journal of Applied Physics*, *111*(9), 094915.

[7] Tabasco-Novelo, C., May-Crespo, J., Ramírez-Rincón, J. A., Forero-Sandoval, I. Y., Rodríguez-Gattorno, G., Quintana, P., & Alvarado-Gil, J. J. (2018). Effects of Sintering on the Thermal and Optical Properties of Zinc Oxide Ceramic. International Journal of Thermophysics, 39(2), 22.

[8] Ramírez-Rincón, J. A., Ares-Muzio, O., Macias, J. D., Estrella-Gutiérrez, M. A., Lizama-Tzec, F. I., Oskam, G., & Alvarado-Gil, J. J. (2018). On the use of photothermal techniques for the characterization of solar-selective coatings. *Applied Physics A*, *124*(3), 252.

[9] Othonos, A., Nestoros, M., Palmerio, D., Christofides, C., Bes, R. S., & Traverse, J. P. (1998). Photothermal radiometry on nickel (pigmented aluminium oxide) selective solar absorbing surface coatings. *Solar energy materials and solar cells*, *51*(2), 171-179.

[10] Mandelis, A., Vanniasinkam, J., Budhudu, S., Othonos, A., & Kokta, M. (1993). Absolute nonradiative energy-conversion-efficiency spectra in $Ti_{3+}:Al_2O_3$ crystals measured by noncontact quadrature photopyroelectric spectroscopy. *Physical Review B*, *48*(10), 6808

[11] Gomez-Heredia, C. L., Macias, J., Ordonez-Miranda, J., Ares, O., & Alvarado-Gil, J. J. (2017). Diffusive-to-ballistic transition of the modulated heat transport in a rarefied air chamber. *AIP Advances*, *7*(1), 015032.

[12] Tompkins H. G., and Irene E. A., *Handbook of ellipsometry* (William Andrew, New York, 2005).

[13] Jawoollam (2004), http://www.jawoollam.com/Tutorial_index.html.

[14] Cox, L. J. (1978). Ellipsometry and Polarized Light. Optica Acta: International Journal of Optics, 25(3), 270-271.

[15] Jones, R. C. (1941). A new calculus for the treatment of optical systems. I. Description and discussion of the calculus. JOSA, 31(7), 488-493.

[16] Houska, J., Kolenaty, D., Rezek, J., & Vlcek, J. (2017). Characterization of thermochromic VO_2 (prepared at 250^0C) in a wide temperature range by spectroscopic ellipsometry. Applied Surface Science, 421, 529-534.

[17] Orava, J., Wágner, T., Šik, J., Přikryl, J., Frumar, M., & Beneš, L. (2008). Optical properties and phase change transition in $Ge_2Sb_2Te_5$ flash evaporated thin films studied by temperature dependent spectroscopic ellipsometry. Journal of Applied Physics, 104(4), 043523.

[18] Pop, S. D., Hinrichs, K., Wenmackers S., Cobet C., Esser N., and Zahn D. R., in Ellipsometry of Functional Organic Surfaces and Films, edited by K. Hinrichs, and K. Eichhorn (Springer, Berlin, 2018).

[19] Herzinger, C. M., Johs, B., McGahan, W. A., Woollam, J. A., & Paulson, W. (1998). Ellipsometric determination of optical constants for silicon and thermally grown silicon dioxide via a multi-sample, multi-wavelength, multi-angle investigation. Journal of Applied Physics, 83(6), 3323-3336.

[20] Nazari, M., Zhao, Y., Kuryatkov, V. V., Fan, Z. Y., Bernussi, A. A., & Holtz, M. (2013). Temperature dependence of the optical properties of VO_2 deposited on sapphire with different orientations. Physical Review B, 87(3), 035142.

[21] Seal, K., Sharoni A., Messman, J. M., Lokitz, B. S., Shaw, R. W., Shuller I. K., Snijders, P. C. & Ward, T. Z. Sci. Rep. 4, 6529 (2014).

2. Three-dimensional heat propagation model in one and two-layer samples

2.1. Introduction

Most of the solar thermal energy conversion and storage technologies are based on thin films of selective optical absorption deposited on bulk substrates, which promote the fast heat conduction (high thermal diffusivity, α) from the surface to the back face [1,2]. The photothermal characterization of this kind of substrates (mostly metals) at low modulation frequencies range (< 1 KHz) it is not a simple task, due to its high thermal diffusion properties (diffusivity and conductivity) which generate three-dimensional (3D) heat propagation inside the material [3]. Three-dimensional (3D) heat propagation modelling has been explored previously by Beck et.al. and Mandelis using the Green functions formalism and Fourier transform [4,5] to solve the heat equation in Cartesian coordinates, which requires the solution of a volume integral (i.e. three integrals), that allows to obtain numerical results and permits the complete thermal characterization of the material.

In this chapter, based on the geometry of the energy source, the heat equation will be solved in cylindrical coordinates by using the Hankel transform [6], which reduces the thermal characterization to a linear integral, which can be easily solved numerically. Moreover, the three-dimensional heat propagation solution allows to compare the thermal profiles with those obtained with the one-dimensional approach. This procedure permits to obtain the limits where

both models match for single layer samples. Finally, the limits of the models to predict the thermal and optical properties of thin films deposited on bulk substrates are explored.

2.2. Heat conduction equation: Solution by means of Hankel transform

Let's consider an opaque layer of thickness L, thermal diffusivity α and thermal conductivity k, which is heating up with a laser beam of modulated intensity I and spot size d (2a), as is shown in Fig. 2.1(a).
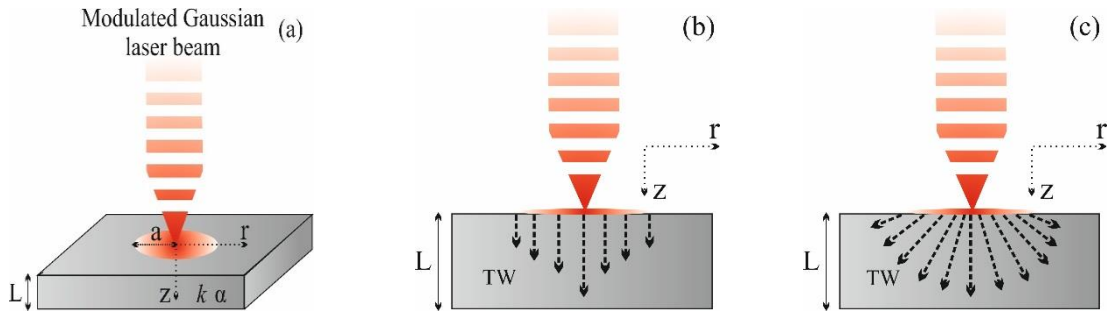
Fig. 2.1. (a) Scheme of a Gaussian laser beam modulated in amplitude, heating up a sample of a homogeneous material with thickness L, thermal diffusivity α and thermal conductivity k. (b). For sufficiently thin samples depending on its thermal diffusivity, it can be assumed that the thermal waves travel only along the thickness of the sample. (c) The light energy flux generates thermal waves (TW) in the material that travel in all directions from the source.

It has been shown for a plate-shaped sample that heat diffusion can be considered as one dimensional, when the modulation frequency of the laser (f), the thickness (d) and the thermal diffusivity (α) satisfy the condition $10 \leq d/\mu$ [7], where $\mu = \sqrt{\alpha/\pi f}$ is the thermal diffusion length. In this case heat transfer is predominantly happening in the perpendicular direction to the incidence plane [see Fig. 2.1(b)]. In the opposite case, in which $10 > d/\mu$, the thermal wave has an additional parallel component [see Fig. 2.1(c)] and the heat propagation becomes three-dimensional.

Considering a laser of energy flux I [Wm^{-2}], with a Gaussian profile as follows [8],

$$I(r) = 2I_0(1 - R)\eta_{NR}e^{-2\left(\frac{r}{a}\right)^2}, \tag{2.1}$$

where R and η_{NR} are the optical reflectance and light into heat conversion efficiency of the illuminated surface at the incident wavelength respectively [9], a is the radius at which the laser intensity falls to e^{-2} of its maximum value measured from the central axis (I_0). The temperature profile across a material in the coordinates space $T(r, \phi, z, t)$ can be obtained from the heat transfer equation [10],

$$\nabla^2 T(r, \phi, z, t) - \frac{1}{\alpha}\frac{\partial T(r, \phi, z, t)}{\partial t} = -\frac{Q}{k}, \tag{2.2}$$

where the heat source is $Q = I(r)(1 + e^{i\omega t})$, $\omega = 2\pi f$ and f is the modulation frequency.

The temperature $T(r, z, t)$ is composed of two parts, the steady state (ψ) and modulated (θ) components as $T(r, \phi, z, t) = \psi(r, z, \phi) + \theta(r, z, \phi)e^{i\omega t}$. Moreover, from the angular symmetry of the Gaussian spot ($\phi = cte$), the modulated temperature profile $\theta(r, z)$ using Eq. (2.2) is given by

$$\frac{1}{r}\frac{\partial}{\partial r}\left(r\frac{\partial\theta(r, z)}{\partial r}\right) + \frac{\partial^2\theta(r, z)}{\partial z^2} - \frac{i\omega\theta(r, z)}{\alpha} = -\frac{Q}{k}. \tag{2.3}$$

The radial component of Eq. (2.3) can be conveniently solved using the Hankel transform $\tilde{\theta}(\lambda, z) = \int_0^\infty \theta(r, z) J_0(\lambda r) r dr$ [6], therefore in terms of $\tilde{\theta}(\lambda, z)$ the heat diffusion equation can be rewritten as

$$\frac{\partial^2\tilde{\theta}(\lambda, z)}{\partial z^2} - \sigma^2(\lambda)\tilde{\theta}(\lambda, z) = -\frac{\tilde{I}(\lambda)}{k}, \tag{2.4}$$

where $\sigma(\lambda) = \sqrt{\lambda^2 + \frac{i\omega}{\alpha}}$ and $\tilde{I}(\lambda) = H[I(r)]$ is the Hankel transform of the energy flux defined in Eq. (2.1). Eq. (2.4) has the conventional form of the differential equation for one-dimensional heat propagation [10], in the Hankel space in this case.

2.2.1. Heat propagation model for an opaque layer of thickness L
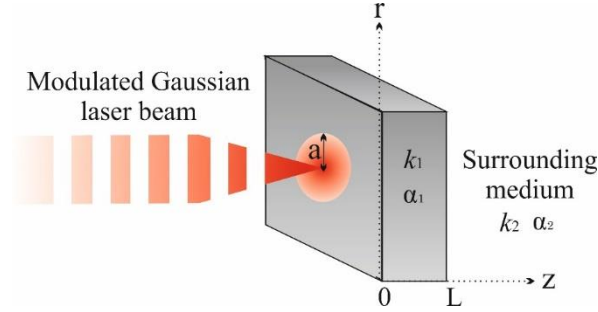
Fig. 2.2. Scheme of a laser beam of modulated amplitude heating up a sample of thickness L and thermal properties α_1 and k_1, in thermal contact with a thermally thick medium of thermal properties α_2 and k_2.

The scheme of one opaque layer of thickness L and thermal properties α_1 and k_1 in thermal contact with a thermally thick medium ($\mu_2 > 2L_2$) [11], of thermal properties α_2 and k_2 is given in Fig. 2.2. To solve the heat transport equation associated to this geometry, the conventional boundary conditions for the temperature and flux continuity are given in Eq. (2.5a-c) [5,10].

$$\tilde{\theta}_1(L1) = \tilde{\theta}_2(L1) \tag{2.5a}$$

$$-k_1 \frac{\partial \tilde{\theta}_1}{\partial z} /_{z=0} = \tilde{I}(\lambda) \tag{2.5b}$$

$$k_1 \frac{\partial \tilde{\theta}_1}{\partial z} /_{z=L1} = k_2 \frac{\partial \tilde{\theta}_2}{\partial z} /_{z=L1.} \tag{2.5c}$$

The solution to Eq. (2.4) for each layer is

$$\tilde{\theta}_1(\lambda, z) = A e^{\sigma_1(\lambda)z} + B e^{-\sigma_1(\lambda)z}$$

$$\tilde{\theta}_2(\lambda, z) = C e^{-\sigma_2(\lambda)z}, \tag{2.6a}$$

where $\sigma_j(\lambda) = \sqrt{\lambda^2 + \frac{i\omega}{\alpha_j}}$ and A, B, C are constants to be determined from the boundary conditions.

The solution of the heat diffusion equation at the first layer, at the illuminated surface ($z = 0$) is similar to the well-known heat propagation model for the one-dimensional case [3,5,12], but in this case $\tilde{\theta}_1$ shown in Eq. (2.7) is defined in the Hankel space

$$\tilde{\theta}_1(\lambda, 0) = \frac{\tilde{I}(\lambda)}{k_1 \sigma_1(\lambda)} \left[\frac{(1 + e_{21})e^{\sigma_1(\lambda)L_1} + (1 - e_{21})e^{-\sigma_1(\lambda)L_1}}{(1 + e_{21})e^{\sigma_1(\lambda)L_1} - (1 - e_{21})e^{-\sigma_1(\lambda)L_1}} \right]. \tag{2.7a}$$

Considering that most of the applications are developed under ambient conditions, it is possible to assume that medium 2 is air, and taking into account that for solid materials (semiconductors and metals) $k_2 = k_{air} \ll k_1$, $e_{21} = \frac{k_2 \sigma_2(\lambda)}{k_1 \sigma_1(\lambda)} \ll 1$, Eq. (2.7a) is

$$\tilde{\theta}_1(\lambda, 0) = \frac{\tilde{I}(\lambda)}{k_1 \sigma_1(\lambda)} \left[\frac{1 + e^{-2\sigma_1(\lambda)L_1}}{1 - e^{-2\sigma_1(\lambda)L_1}} \right], \tag{2.7b}$$

where $\tilde{I}(\lambda) = H[I(r)]$ is the Hankel transform of the Gaussian energy flux given by Eq. (2.1).

$$\tilde{I}(\lambda) = H[I(r)] = 2I_0(1 - R)\eta_{NR} \int_0^\infty e^{-2\left(\frac{r}{a}\right)^2} J_0(\lambda r) r \, dr \tag{2.8a}$$

$$\tilde{I}(\lambda) = \frac{a^2 I_0(1 - R)\eta_{NR}}{2} e^{-(a\lambda/\sqrt{8})^2}. \tag{2.8b}$$

Once Eq. (2.4) is solved for the sample under study, the inverse Hankel transform should be used to obtain the temperature field in the physical space [13]

$$\theta(r, z) = \int_0^\infty \tilde{\theta}_1(\lambda, z) J_0(\lambda r) \lambda \, d\lambda. \tag{2.9}$$

Therefore, the modulated temperature at the front face in a point r on sample's surface [$\theta(r, z = 0)$] for an opaque single layer in thermal contact with air, using the Eq. (2.7b) and Eq. (2.8b) yields

$$\theta(r,0) = \frac{a^2 I_0 (1-R)\eta_{NR}}{2} \int_0^\infty e^{-(a\lambda/\sqrt{8})^2} \frac{1}{k_1 \sigma_1(\lambda)} \left(\frac{1+e^{-2\sigma_1(\lambda)L_1}}{1-e^{-2\sigma_1(\lambda)L_1}} \right) J_0(\lambda r) \lambda d\lambda. \tag{2.10}$$

2.2.2. Heat propagation model for a semi-transparent layer of thickness L_1 resting on an opaque substrate (L_2)
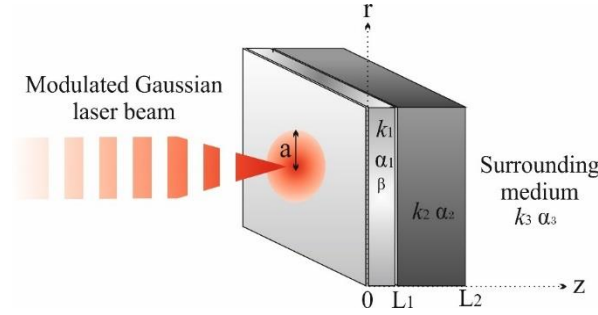
Fig. 2.3. Scheme of a laser beam of modulated amplitude heating up a two layers sample of thickness L_1 and L_2 and thermal properties α_1, k_1 and α_2, k_2 in contact with a thermally thick medium (α_3, k_3). The first layer (non-opaque) has an optical absorption coefficient β.

In this section heat diffusion in a two layers system, in which the front layer has an optical absorption coefficient β, is considered. The incident light illuminates a layer of thickness L_1, thermal diffusivity α_1, and thermal conductivity k_1. Layer 2 has a thickness L_2, thermal diffusivity α_2, and thermal conductivity k_2. The layers are surrounded by a thermally thick medium with thermal diffusivity and thermal conductivity α_3, k_3 respectively.

In order to take the non-opaqueness condition of the first layer to the incident light into account, the heat source must be modified to [14,15],

$$Q = I(r)\beta e^{-\beta z + i\omega t}. \tag{2.11a}$$

The heat equation equation to be solved is,

$$\frac{\partial^2 \tilde{\theta}(\lambda,z)}{\partial z^2} - \sigma^2 \tilde{\theta}(\lambda,z) = -\tilde{I}(\lambda)\frac{\beta}{k}e^{-\beta z}. \tag{2.11b}$$

The modulated temperaure is obtained using the following boundary conditions for the flux Eq. (2.12a-c) and temperature Eq. (2.12d-e) [16]

$$-k_1 \frac{\partial \tilde{\theta}_1}{\partial z} \Big/_{z=0} = 0 \qquad (2.12a)$$

$$-k_1 \frac{\partial \tilde{\theta}_1}{\partial z} \Big/_{z=L_1} = -k_2 \frac{\partial \tilde{\theta}_2}{\partial z} \Big/_{z=L_1} \qquad (2.12b)$$

$$-k_2 \frac{\partial \tilde{\theta}_2}{\partial z} \Big/_{z=L_1+L_2} = -k_3 \frac{\partial \tilde{\theta}_3}{\partial z} \Big/_{z=L_1+L_2} \qquad (2.12c)$$

$$\tilde{\theta}_1(L_1) = \tilde{\theta}_2(L_1) \qquad (2.12d)$$

$$\tilde{\theta}_2(L_1 + L_2) = \tilde{\theta}_3(L_1 + L_2). \qquad (2.12e)$$

The solution to Eq. (2.11) for the first layer has the form $\tilde{\theta}_1(\lambda, z) = \tilde{\theta}_h + \tilde{\theta}_p$ where $\tilde{\theta}_h$ and $\tilde{\theta}_p$ are the homogeneous and particular solutions, respectively.

$$\tilde{\theta}_1(\lambda, z) = \tilde{\theta}_h + \tilde{\theta}_p = A e^{\sigma_1(\lambda)z} + B e^{-\sigma_1(\lambda)z} + C e^{-\beta z}. \qquad (2.13)$$

In this equation, A, B, C are constants to be determined from the boundary conditions, along with the solutions for the second $\tilde{\theta}_2(\lambda, z) = D e^{\sigma_2(\lambda)(z-L_1)} + E e^{-\sigma_2(\lambda)(z-L_1)}$ and third $\tilde{\theta}_3(\lambda, z) = F e^{-\sigma_3(\lambda)(z-L_1-L_2)}$ layer.

After some algebraic work, the modulated temperature at the front face ($z = 0$) in the Hankel space for a two layers system in thermal contact with a thermally thick substrate is given by

$$\tilde{\theta}_1(\lambda, 0) = \frac{\tilde{I}(\lambda)\beta}{k_1(\sigma_1^2(\lambda) - \beta^2)} \left[\frac{\beta}{\sigma_1(\lambda)} + 1 \right.$$

$$\left. + \frac{\frac{k_2\sigma_2(\lambda)}{k_1}\left(\frac{\beta}{\sigma_1(\lambda)}e^{\sigma_1(\lambda)L_1} + e^{-\beta L_1}\right) - \gamma(\lambda)\,\beta(e^{\sigma_1(\lambda)L_1} - e^{-\beta L_1})}{\gamma(\lambda)\,\sigma_1(\lambda)\sinh(\sigma_1(\lambda)L_1) - \frac{k_2\sigma_2(\lambda)}{k_1}\cosh(\sigma_1(\lambda)L_1)} \right], \qquad (2.14a)$$

where the thermal-wave reflection coefficient at the interface between the medium 2 and 3 is $R_{32} = \frac{1-e_{32}(\lambda)}{1+e_{32}(\lambda)}$, with $e_{32}(\lambda) = \frac{k_3\sigma_3(\lambda)}{k_2\sigma_2(\lambda)}$ and $\gamma(\lambda) = \left(\frac{e^{-2\sigma_2(\lambda)L_2}R_{32}+1}{e^{-2\sigma_2(\lambda)L_2}R_{32}-1}\right)$. If the medium 3 is air, $k_3 = k_{air} \ll k_2$, and Eq. (2.14a) is reduced to

$$\tilde{\theta}_1(\lambda, 0) = \frac{\tilde{I}(\lambda)\rho(\lambda)}{k_1\sigma_1(\lambda)\big(1 - \rho^2(\lambda)\big)}\Bigg[\rho(\lambda) + 1$$
$$- 2\frac{e_{21}(\lambda)\big(\rho(\lambda) + e^{-\sigma_1(\lambda)L_1(1+\rho(\lambda))}\big)\tanh(\sigma_2(\lambda)L_2) + \rho(\lambda)\big(1 - e^{-\sigma_1(\lambda)L_1(1+\rho(\lambda))}\big)}{1 - e^{-2\sigma_1(\lambda)L_1} + e_{21}(\lambda)(1 + e^{-2\sigma_1(\lambda)L_1})\tanh(\sigma_2(\lambda)L_2)}\Bigg],$$

$$(2.14b)$$

where $\rho(\lambda) = \beta/\sigma_1(\lambda)$, $e_{21}(\lambda) = \frac{k_2\sigma_2(\lambda)}{k_1\sigma_1(\lambda)}$ and $\sigma_j(\lambda) = \sqrt{\lambda^2 + \frac{i\omega}{\alpha_j}}$.

Eq. (2.14b) is the three-dimensional heat propagation model for the modulated temperature in the Hankel space, for a two layers sample in thermal contact with a medium of low thermal conductivity (air). It is easy to verify that in the limit in which $L_2 \to \infty$, $k_2 = k_{air}$ and $\beta \to \infty$ (opaque layer), Eq. (2.14b) reduces to Eq. (2.7b) as is expected.

The inverse Hankel transform of Eq. (2.9) allows to obtain the temperature field in the physical space.

$$\theta(r, 0) = \frac{a^2 I_0(1 - R)\eta_{NR}}{2}\int_0^\infty e^{-(a\lambda/\sqrt{8})^2} g(\lambda)J_0(\lambda r)\lambda d\lambda, \qquad (2.15)$$

where,

$$g(\lambda) = \frac{\rho(\lambda)}{k_1\sigma_1(\lambda)(1 - \rho^2)}\Bigg[\rho(\lambda) + 1$$
$$- 2\frac{e_{21}(\lambda)\big(\rho(\lambda) + e^{-\sigma_1(\lambda)L_1(1+\rho(\lambda))}\big)\tanh(\sigma_2(\lambda)L_2) + \rho(\lambda)\big(1 - e^{-\sigma_1(\lambda)L_1(1+\rho(\lambda))}\big)}{1 - e^{-2\sigma_1(\lambda)L_1} + e_{21}(\lambda)(1 + e^{-2\sigma_1(\lambda)L_1})\tanh(\sigma_2(\lambda)L_2)}\Bigg]. \quad (2.16)$$

2.2.3. General solutions

The experimental photothermal signals as a consequence of deteccion area of the transductor used (IR sensor, microphone, pirolectric, e.t.c.), provide information about average temperature on sample's surface. Then, to include this condition in the models developed in Sec. 2.2.2, it is necessary add all contributions along the spot diameter ($r = a$) through the area integral as follows

$$\langle\theta(z)\rangle = \frac{1}{\pi a^2}\int_0^a \theta(r, z)2\pi r dr. \qquad (2.17a)$$

For the single opaque layer, the average temperature of $\theta(r, z)$ at $z = 0$ is obtained by using Eq. (2.10) in the integral Eq. (2.17a)

$$\langle \theta(0) \rangle = \frac{I_0(1-R)\eta_{NR}}{k_1} \int_0^a \int_0^\infty e^{-(a\lambda/\sqrt{8})^2} \frac{1}{\sigma_1(\lambda)} \left(\frac{1 + e^{-2\sigma_1(\lambda)L_1}}{1 - e^{-2\sigma_1(\lambda)L_1}} \right) J_0(\lambda r)\lambda d\lambda \, rdr, \qquad (2.17b)$$

$$\langle \theta(0) \rangle = \frac{aI_0(1-R)\eta_{NR}}{k_1} \int_0^\infty e^{-(a\lambda/\sqrt{8})^2} \frac{1}{\sigma_1(\lambda)} \left(\frac{1 + e^{-2\sigma_1(\lambda)L_1}}{1 - e^{-2\sigma_1(\lambda)L_1}} \right) J_1(a\lambda)d\lambda, \qquad (2.18)$$

while for the two layers system the average of the temperature is

$$\langle \theta(0) \rangle = aI_0(1-R)\eta_{NR} \int_0^\infty e^{-(a\lambda/\sqrt{8})^2} g(\lambda)J_1(a\lambda)d\lambda, \qquad (2.19)$$

where $J_1(a\lambda)$ is the first order Bessel`s function in the Hankel space, and $g(\lambda)$ has been defined in Eq. (2.16).

Eqs. (2.18) and (2.19) are the general solutions of the modulated temperature for a medium that presents three-dimensional heat propagation. Similar results have been reported by Fabbri et.al. where the analysis has been done considering the size of detection area instead the illumination spot size [17]. These implies that the one-dimesional heat propagation condition must be evaluated for each experimental setup.

2.3. One-dimensional heat propagation limits

The general mathematical model obtained in Sec. 2.2 allows describing the photothermal signals of high, medium and low thermal diffusivity materials for any modulation frequency. In this section will analyze the limits under which these models predict the well-known behavior of the one-dimensional heat propagation.

2.3.1. Uniform laser beam

The mathematical modelling developed in Sec. 2.2 describes the heat propagation in a solid material, from an energy source of Gaussian geometry which generates a cylindrical heating.

In the simplest case, if a uniform beam $I(r) = I_0(1 - R)\eta_{NR}$ is considered, Eq. (2.8) modifies as

$$\tilde{I}(\lambda) = H[I(r)] = I_0(1 - R)\eta_{NR} \int_0^\infty J_0(\lambda r) r \, dr$$

$$\tilde{I}(\lambda) = I_0(1 - R)\eta_{NR} \frac{\delta(\lambda - 0)}{\lambda}, \tag{2.20}$$

therefore, the Eq. (2.15) for the two layer model, the modulated temperature reduces to

$$\theta(r, 0) = I_0(1 - R)\eta_{NR} \int_0^\infty \frac{\delta(\lambda - 0)}{\lambda} \, g(\lambda) J_0(\lambda r) \lambda d\lambda \tag{2.21a}$$

$$\theta(0) = I_0(1 - R)\eta_{NR} \, g(0) J_0(0) \tag{2.21b}$$

$$\theta(0) = I_0(1 - R)\eta_{NR} \frac{\rho}{k_1 \sigma_1 (1 - \rho^2)} \left[\rho + 1 \right.$$
$$\left. - 2 \frac{e_{21}\left(\rho + e^{-\sigma_1 L_1 (1+\rho)}\right) \tanh(\sigma_2 L_2) + \rho(1 - e^{-\sigma_1 L_1 (1+\rho)})}{1 - e^{-2\sigma_1 L_1} + e_{21}(1 + e^{-2\sigma_1 L_1}) \tanh(\sigma_2 L_2)} \right], \tag{2.22c}$$

where $\sigma_j = (1 + i)/\mu_j$ is the thermal wave number of the one-dimensional heat propagation model [5,17].

This result indicates that: (1) 3D effects can be described under the Hankel transform methodology while the energy source presents non-uniform geometry, and (2) the one-dimensional heat propagation model can be obtained directly from the solution of Eqs. (2.18-2.19), which for an opaque single layer is given by

$$\theta(0) = \frac{I_0(1 - R)\eta_{NR}}{k_1 \sigma_1} \left[\frac{1 + e^{-2\sigma_1 L_1}}{1 - e^{-2\sigma_1 L_1}} \right]. \tag{2.23}$$

2.3.2. Frequency scan

According to the one-dimensional heat propagation condition $10 \leq d/\mu$, for a solid material of high thermal diffusivity, experimentally the lateral propagation can be avoiding if the

modulation frequency is high enough [3], therefore, there exists a limit from where the three-dimensional models of Eq. (2.18) and (2.19) should describe the same behavior as 1D propagation of Eq. (2.22c) and (2.23) respectively.

For a silicon single layer of thermal diffusivity (96 mm^{2}s^{-1}), thermal conductivity (147 W m^{-1} K^{-1}) and thickness 525 μm [19], illuminated with a Gaussian spot of 5 mm ($2a$), the amplitude and phase of the modulated temperature predicted by the three-dimensional heat propagation model (black lines) of Eq. (2.18) is shown and compared in Fig. 2.4, with the temperature expected using the one-dimensional model of Eq. (2.23).

Fig. 2.4. (a) Amplitude and (b) phase temperature components of a silicon (Si) bulk, obtained by using the three-dimensional (black lines) and one dimensional (red lines) heat propagation models given in Eq. (2.18) and (2.23) respectively. The factor $I_0(1-R)\eta_{NR}$ has been set equal to 1 Wm^{-2}. The values of the thermal properties of silicon were taken from Ref [19].

Under the experimental conditions described above, the 3D heat propagation model developed in this work, according to the phase component, falls to 1D propagation values expected for a silicon sample for modulation frequencies greater than 125 Hz (f_{min}), same value to predicted by the condition $10 \leq d/\mu$. In order to verify this, similar simulations have been carried out for other two materials of high thermal diffusivity, and the results are shown in Figs. 2.5 and 2.6.

The phase component [Fig. 2.5(b) and 2.6(b)] of the modulated temperature for copper ($\alpha = 147$ mm^{2}s^{-1}, $k = 401$ Wm^{-1}K^{-1}) and silver ($\alpha = 174$ mm^{2}s^{-1}, $k = 429$ Wm^{-1}K^{-1}) layers [19], show that the minimum frequency values from where both models (3D and 1D) match increases as the thermal diffusivity is higher (as expected), and still similar to the predicted by the relation $10 \leq d/\mu$, 150 Hz for copper and 220 Hz for silver.
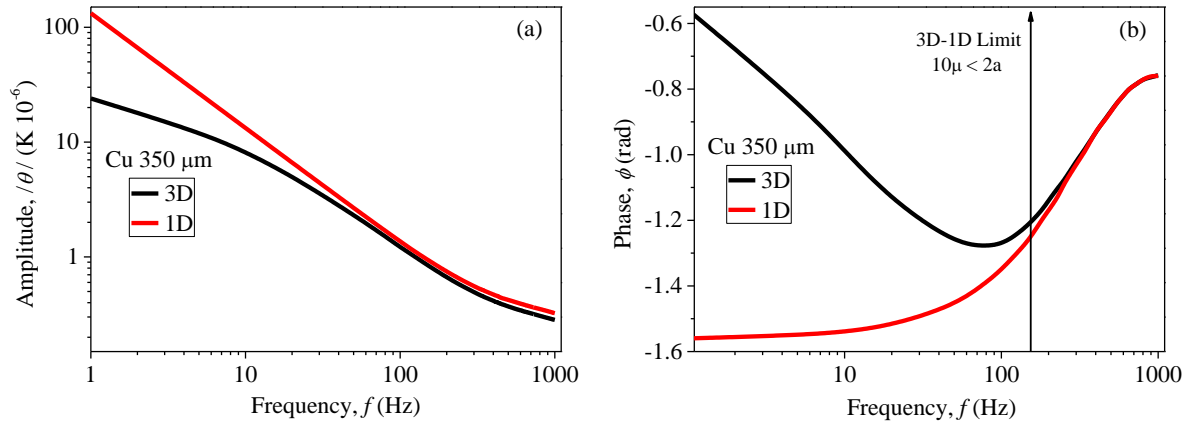
Fig. 2.5. (a) Amplitude and (b) phase delay temperature components of a copper (Cu) plate, obtained by using the three (black lines) and one (red lines) dimensional heat propagation models of Eq. (2.18) and (2.23) respectively. The factor $I_0(1-R)\eta_{NR}$ has been taken equal to $1\ Wm^{-2}$. The values of the thermal properties of copper were taken from Ref [19].
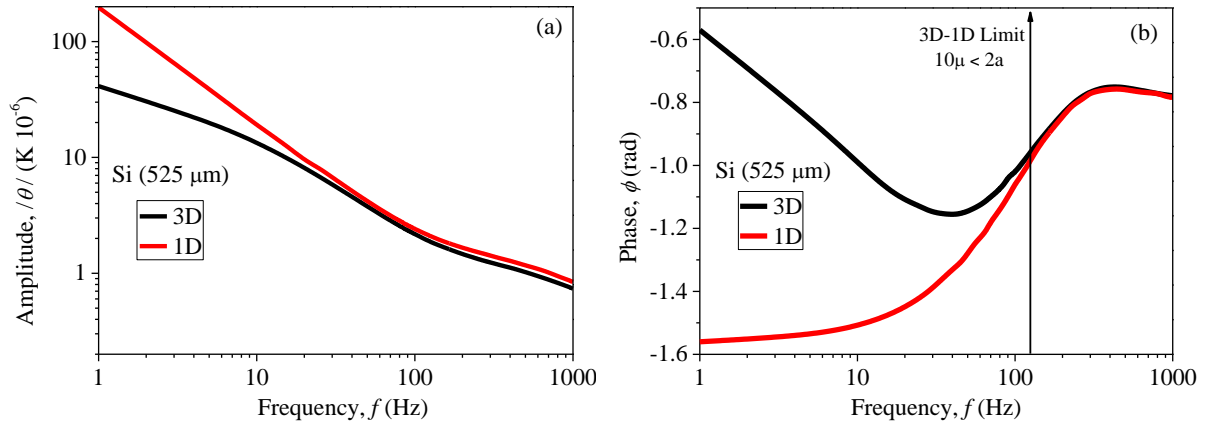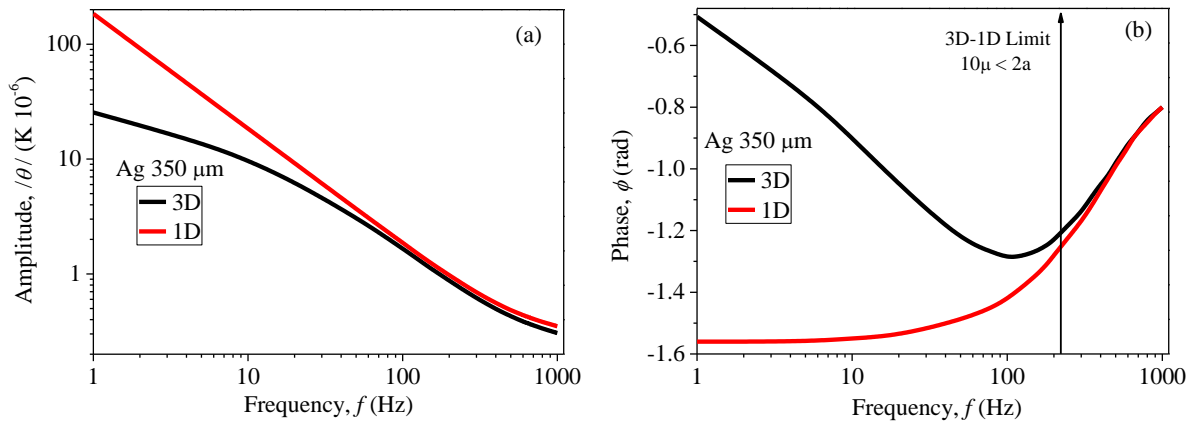

Fig. 2.6. (a) Amplitude and (b) phase delay temperature components of a silver (Ag) bulk, obtained by using the three (black lines) and one (red lines) dimensional heat propagation model given in Eqs. (2.18) and (2.23) respectively. The factor $I_0(1-R)\eta_{NR}$ has been taken equal to $1\ W/m^2$. The values of the thermal properties of silver were taken from Ref [19].

The amplitude of the modulated temperature for the silicon, copper and silver samples showed in Fig. 2.4(a), 2.5(a) and 2.6(a) predict lower values of f_{min} for the three cases. This means that the optical dependence through the factor $I_0(1-R)\eta_{NR}$, taken equal to $1\ Wm^{-2}$ for the three materials, is stronger than the thermal one in this component. Then, the heat propagation characteristics should be obtained from the phase signal. In chapter 3, will be shown experimentally how this condition is satisfy for ASIS 304, copper and aluminum substrates.

2.4. Thin film analysis

One of the most restrictive problems of the conventional photothermal techniques (PTR, PAS, TWRC) corresponds to the analysis of heat propagation in thin films, i.e. layers where the thermal diffusion length is much larger than the thickness, $\mu \gg L$ [11]. In this section, we perform the analysis of the temperature profile and the physical and geometrical conditions that can allow to determine the optical and thermal properties of a thin film deposited on a thermally thick substrate.

2.4.1. Thermal properties

The solution of the heat propagation Eq. (2.4) is based on exponential functions such as $e^{-\sigma_j L}$, where $\sigma_j = \frac{1+i}{\mu_j}$ for the one-dimensional propagation case [3,12,17], or $\sigma_j = \sqrt{\lambda^2 + \frac{i\omega}{\alpha_j}}$ for the three-dimensional one, and L is the layer thickness. This kind of dependences introduces strong restrictions for the analysis of thin films (thickness from nanometers to micrometers) in modulation frequencies ranges that can be measured and controlled via lock-in (below 100 KHz). Specifically, a thin layer could be analyzed by using these heat propagation models if $Re[\sigma L] \sim 1$, i.e. when the real part of the argument in the exponential is large enough to avoid that $e^{-\sigma_j L} \sim 1$ [3].

Additional to the modulation frequency (f) and thermal diffusivity (α), the three-dimensional propagation modelling presented in Sec. 2.2, has the integration limits (x) as potential parameter to guarantee that $Re[\sigma L] \gg 0$. Fig. 2.7 shows a comparison between the predicted modulated temperature by using the 3D and 1D heat propagation models of Eq. (2.19) and (2.22c) respectively, for a dielectric thin film of vanadium dioxide (VO$_2$) deposited on a silicon substrate at low modulation frequencies [20].
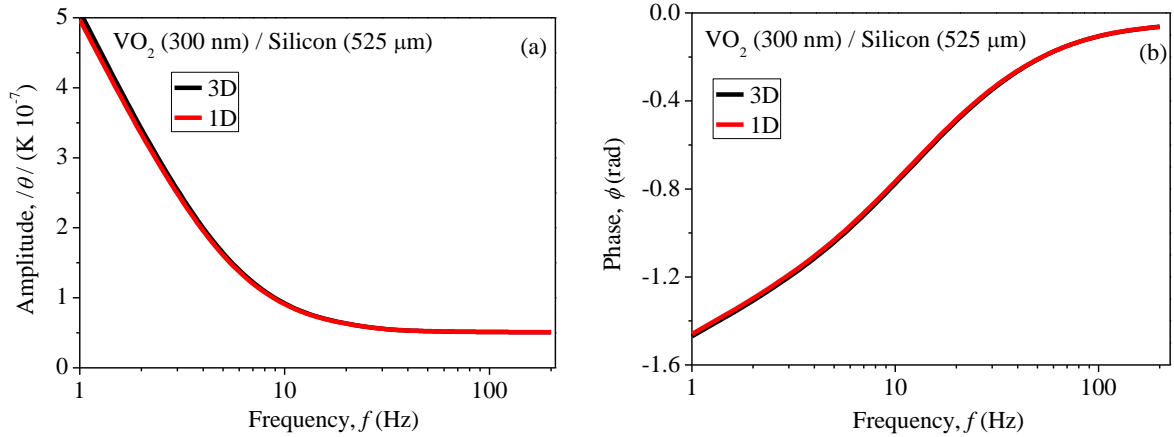
Fig. 2.7. (a) Amplitude and (b) phase delay components of the temperature of a two layers sample (VO$_2$+Silicon), obtained by using the three (black lines) and one (red lines) dimensional heat propagation models of Eq. (2.19) and (2.22c) respectively. The factor $I_0(1-R)\eta_{NR}$ has been set to $1\mathrm{Wm}^{-2}$.

In this case, in contrast to the result obtained previously for a single layer (see Fig. 2.4), both models present the same values for the amplitude and phase components of the temperature, therefore as for the 1D propagation case, the three-dimensional model of Eq. (2.19) is only valid if each layer satisfies the condition $L/\mu \geq 1$ [21].

From the results of Fig. 2.7 it can be concluded that the thermal characterization of thin films deposited on bulk substrates can be achieved only in two cases: (1) if the modulation frequency used is higher than 1 MHz (10^9 Hz) [22], or (2) for a film of thermal diffusivity (α_1) around $\sim 10^{-4}$ mm^2 s^{-1}, much smaller than the reported values for solid state materials [23].

2.4.2. Optical properties

Taking into account that thermal characterization of thin films by using the mathematical model of Eq. (2.22c) can be achieved in the high modulation frequencies regimen, it is possible to guarantee that in the opposite range ($f < 3$ kHz) the heat propagation in a multi-layered sample (thin film+substrate) is given by the thermal properties of the substrate [3], which is described based on the mathematical model of Eq. (2.18) for 3D heat propagation or Eq. (2.23) for the one-dimensional case.

On the other hand, according to Figs. (2.4 to 2.6), it can be observed that optical properties have dependence only on the amplitude component of the temperature through the relation

$I_0(1 - R)\eta_{NR}$, which is associated to the incident energy flux absorption of the illuminated surface. Therefore, the difference in the amplitude signal between the substrate and thin film+substrate will be directly associated to the optical reflectance R and the light into-heat conversion efficiency η_{NR} of each surface [3,24]. The experimental details in the optical characterization of different thin films deposited on metallic substrates will be developed in chapters 3 and 4.

2.5. Conclusions

A simple methodology to consider the effects of three-dimensional heat propagation in materials of high thermal diffusivity has been shown, considering a modulated Gaussian energy source. Aditionally, the one-dimensional heat propagation limits have been explored, concluding from amplitude and phase components, that both models predict the same behavior under the following conditions: (1) For a uniform laser beam, or/and (2) when the modulation frequency satisfy that $10 \leq d/\mu$.

By means of the mathematical models developed, the photothermal signals of thin films ($<$ 1000 nm) deposited on thick substrate have been studied. From there it was found that the thermal characterization can be only achieved if the modulation frequency used is sufficiently high to satisfy that $L/\mu \geq 1$, which for typical solid-state thin films requires modulation frequencies higher than 1 MHz (10^9 Hz).

References

[1] Kalogirou, S. A. (2004). Solar thermal collectors and applications. *Progress in energy and combustion science*, *30*(3), 231-295.

[2] Valleti, K., Krishna, D. M., & Joshi, S. V. (2014). Functional multi-layer nitride coatings for high temperature solar selective applications. *Solar Energy Materials and Solar Cells*, *121*, 14-21.

[3] Ramírez-Rincón, J. A., Ares-Muzio, O., Macias, J. D., Estrella-Gutiérrez, M. A., Lizama-Tzec, F. I., Oskam, G., & Alvarado-Gil, J. J. (2018). On the use of photothermal techniques for the characterization of solar-selective coatings. *Applied Physics A*, *124*(3), 252.

[4] Beck, J. V., Cole, K. D., Haji-Sheikh, A., & Litkouhi, B. (1992). *Heat conduction using Green's functions* (p. 151). New York: Hemisphere Publishing Corporation.

[5] Mandelis, A. (2013). Green Functions of One-Dimensional Thermal-Wave Fields. In *Diffusion-wave fields: mathematical methods and Green functions*. Springer Science & Business Media.

[6] Poularikas, A. D. (2010). *Transforms and applications handbook* Chapter 9. CRC press.

[7] Paoloni, S., & Walther, H. G. (1997). Photothermal radiometry of infrared translucent materials. *Journal of applied physics*, *82*(1), 101-106.

[8] Mandelis, A. (2013). Cartesian Thermal-Wave Fields in Three and Two Dimensions. In *Diffusion-wave fields: mathematical methods and Green functions*. Springer Science & Business Media.

[9] Mandelis, A., Vanniasinkam, J., Budhudu, S., Othonos, A., & Kokta, M. (1993). Absolute nonradiative energy-conversion-efficiency spectra in $Ti_{3+}{:}Al_2O_3$ crystals measured by noncontact quadrature photopyroelectric spectroscopy. *Physical Review B*, *48*(10), 6808.

[10] Almond, D. P., & Patel, P. M. (1996). Photothermal Science and Techniques in Physics and its Applications vol 10, ed ER Dobbs and SB Palmer.

[11] Gomez-Heredia, C. L., Macias, J., Ordonez-Miranda, J., Ares, O., & Alvarado-Gil, J. J. (2017). Diffusive-to-ballistic transition of the modulated heat transport in a rarefied air chamber. *AIP Advances*, *7*(1), 015032.

[12] Pichardo, J. L., & Alvarado-Gil, J. J. (2001). Open photoacoustic cell determination of the thermal interface resistance in two layers systems. *Journal of Applied Physics*, *89*(7), 4070-4075.

[13] Poularikas, A. D. (2010). *Transforms and applications handbook* Chapter 17. CRC press.

[14] Helander, P., Lundström, I., & McQueen, D. (1980). Light scattering effects in photoacoustic spectroscopy. *Journal of Applied Physics*, *51*(7), 3841-3847.

[15] Helander, P. (1983). Theoretical aspects of photoacoustic spectroscopy with light scattering samples. *Journal of Applied Physics*, *54*(6), 3410-3414.

[16] Ordonez-Miranda, J., & Alvarado-Gil, J. J. (2013). Infrared emissivity determination using a thermal-wave resonant cavity: comparison between the length-and frequency-scan approaches. *International Journal of Thermal Sciences*, *74*, 208-213.

[17] Fabbri, L., & Cernuschi, F. (1997). Finite laser beam size effects in thermal wave interferometry. *Journal of applied physics*, *82*(11), 5305-5311.

[18] Rosencwaig, A., & Gersho, A. (1976). Theory of the photoacoustic effect with solids. *Journal of Applied Physics*, *47*(1), 64-69.

[19] Touloukian, Y. S., & Ho, C. Y. (1970). Specific heat. Nonmetallic solids. *Thermophysical properties of matter-The TPRC Data Series, New York: IFI/Plenum, 1970-, edited by Touloukian, YS e (series ed.); Ho, CY e (series tech. ed.).*

[20] Leahu, G. L., Li Voti, R., Larciprete, M. C., Belardini, A., Mura, F., Fratoddi, I. & Bertolotti, M. (2014, June). Semiconductor-metal phase transition of vanadium dioxide nanostructures on silicon substrate: Applications for thermal control of spacecraft. In *AIP Conference Proceedings* (Vol. 1603, No. 1, pp. 62-70). AIP.

[21] Martínez-Torres, P., & Alvarado-Gil, J. J. (2011). Photoacoustic monitoring of thermal wave interference effects during the formation of polymeric thin films from solutions. *Applied Physics A*, *105*(4), 975-986.

[22] Hamaoui, G., Horny, N., Gomez-Heredia, C. L., Ramirez-Rincon, J. A., Ordonez-Miranda, J., Champeaux, C., Dumas-Bouchiat, F., Alvarado-Gil, J. J., Ezzahri, Y., Joulain, K., Chirtoc, M., Thermophysical characterisation of VO_2 thin films hysteresis and its application in thermal rectification, *Under review.*

[23] Salazar, A., Sanchez-Lavega, A., & Terrón, J. M. (1998). Effective thermal diffusivity of layered materials measured by modulated photothermal techniques. *Journal of applied physics*, *84*(6), 3031-3041.

[24] Pawlak, M., Gibkes, J., Fotsing, J. L., Zakrzewski, J., Malinski, M., Bein, B. K. & Marasek, A. (2004, October). Study of optical properties of Zn-Be-Te mixed crystals by means of combined modulated IR radiometry and photoacoustics. In *Journal de Physique IV (Proceedings)* (Vol. 117, pp. 47-56). EDP sciences.

3. Optical properties of solar selective coatings by using photothermal techniques

3.1. Introduction

Solar energy is the most abundant renewable energy source, and the two most common technologies are based on the capture of sunlight and conversion into either electricity (photo-electron conversion) or heat (thermal conversion). The best-known solar-thermal collector systems are solar water heaters for domestic use [1], however, significant advances in new materials have expanded the application of solar-thermal devices to a large variety of applications in industry. For example, solar-generated thermal energy can also be applied to evaporate water in a steam turbine and generate electricity [2]. The main feature of the latest generation of solar collectors is the increase in efficiency for converting solar radiation into heat, which has generally been achieved by a careful design of a multi-layered system to capture and convert solar energy [3]. A highly efficient coating must possess a high absorption coefficient across the solar radiation spectrum and very low emission in the infrared range [4], thus maximizing the energy available for heating of the substrate. Selective coatings have functions of adhesion, absorption and protection [5], and the characterization of the thermal and optical properties of these coatings is critical in the design and application in solar collector systems. Energy losses in solar collectors are mainly due to convection, conduction and

radiation. The energy lost by radiation is directly related to the emissivity of the selective coating, therefore, the determination of this coefficient is vital for the design of high efficiency solar collectors. Several methodologies have been devised to measure the emissivity, with the most commonly used method being infrared reflectance spectroscopy [6].

Photothermal techniques are attractive for the characterization of selective coatings due to direct dependence on thermal and optical properties. Photothermal radiometry (PTR) is based on the illumination of a surface with a modulated light source resulting in heating of the surface; as a consequence, the surface emits infrared radiation with a maximum wavelength corresponding to the black body radiation spectrum at the temperature of the sample. PTR has been used extensively in the thermal characterization of a large variety of materials and in the study of surfaces [7,8]. Based on these considerations, PTR would be expected to be a technique especially suited to measure the emissivity of selective coatings. Othonos et al reported the use of PTR in the study of a nickel (pigmented aluminum oxide) selective solar coating, relating the PTR signal size with the amount of radiation emitted by the sample surface; however, they were not able to obtain unambiguous, quantitative results for the emissivity [9]. Photoacoustic spectroscopy (PAS) is also a technique widely used in the determination of thermal and optical properties [10]. In this case, the modulated surface temperature caused by the absorption of the modulated light results in acoustic waves transmitted to the surrounding air and detected using a microphone.

In the first part of chapter 3, the photothermal signals obtained experimentally by using PTR and PAS will be analyzed with three different metallic samples (stainless steel AISI 304, copper and aluminum), which change its optical absorption and emission properties as a consequence of the selective coatings (thin films) deposited on the surface. At low modulation frequencies, two of the substrates (copper and aluminum) present the three-dimensional heat propagation described by the model developed in the chapter 2, while AISI 304 has only 1D heat propagation across the frequency range considered. Based on the results of chapter 2, because of the characteristics of the thin films (thermally thin $\mu \gg L$), the phase component of the modulated temperature (phase signal) only depends on the thermal properties of the substrate, while the signal amplitude changes with the factor $(1 - R)\eta_{NR}$. This last observation will be used at the end of the chapter to optically characterize the solar selective thin films.

3.2. Solar selective coatings based on metal-oxides

Three different types of sample will be studied by using the photothermal techniques: 1) a bilayer selective coating consisting of a 200 nm black nickel absorber film deposited on 1 µm of metallic nickel, both prepared by electrodeposition onto a stainless steel (AISI 304) substrate, denominated BN-Ni-SS; 2) the same selective coating electrodeposited on a copper substrate, BN-Ni-Cu; and 3) a commercial sample of a few microns of TiNOX [11,12] on aluminum, TiNOX-Al. All samples have an area of 2 cm x 2 cm as shown in Fig. 3.1.
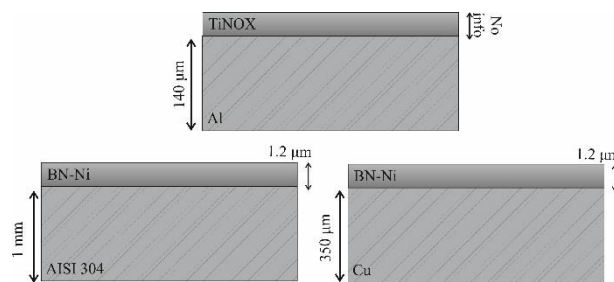
Fig. 3.1. Scheme of the samples analyzed: TiNOX-Al (Almeco solar group [11,12]) and BN-Ni-SS, BN-Ni-Cu (Cinvestav-Mérida [12]).

Samples of BN-Ni were deposited on substrates of stainless steel (SS) and Cu via an electrochemical process. This procedure consists of two steps, the first one uses the substrate as cathode and a sheet of nickel as anode, with a solution of nickel sulfate hexahydrate ($NiSO_4·6H_2O)$, potassium chloride (KCl) and boric acid (H_3BO_3) at pH 4.5, to deposit a layer of nickel of 1 µm thickness on the cathode. The second step consists of depositing a layer of black nickel on the nickel film, for which the Ni-SS or Ni-Cu substrate is used as the cathode and a sheet of stainless steel as anode. In this case, a solution of nickel chloride hexahydrate ($NiCl_2·6H_2O)$ and sodium chloride ($NaCl$) at pH 6.5 is used, obtaining a black nickel layer of 200 nm thickness. A more detailed description of the electrodeposition and characterization of these coatings in Cinvestav Unidad Merida, can be found in the work developed by Lizama *et.al.* and presented in Ref [12].

3.3. Photothermal radiometry (PTR) signals

Photothermal radiometry technique (PTR) is based on the measurement of the changes in the power emitted by a surface, as a consequence of the periodically heating up generated by a modulated heat source, given by the relation [see Eq. (2.4)]

$$\Delta W = 4\epsilon \sigma_B (T + \theta_{dc})^3 \theta, \tag{3.1}$$

where ϵ is the emissivity of the surface, σ_B ($5.67 \times 10^{-8}\,\mathrm{Wm^{-2}K^{-4}}$) is the Stefan-Boltzmann constant, T is the sample temperature, θ_{dc} is the dc temperature rise of the surface due to modulated energy source, and θ is the modulated temperature, which depends on the absorption and light-into-heat conversion efficiency and thermal properties of the layers that compose the sample [13] (see chapter 2). The dependence on the emissivity makes photothermal radiometry an attractive technique for determining this parameter. However, the dependence on the optical reflectance and the light-into-heat conversion factor does not allow a direct determination of the emissivity [9].
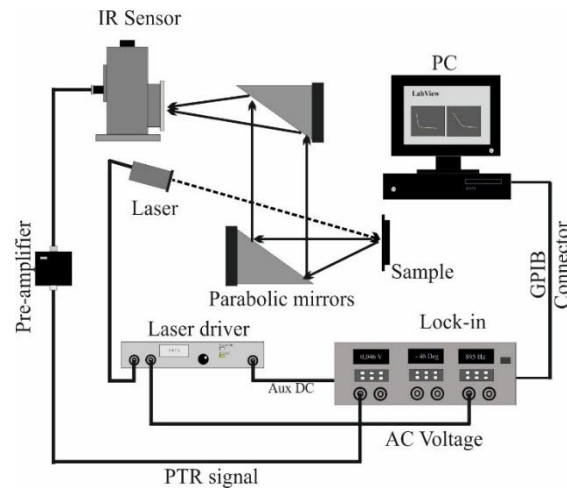
Fig. 3.2. Experimental setup of the photothermal radiometry technique (PTR).

The PTR setup, shown in Fig. 3.2, is composed by a laser modulated in amplitude (heating source) of 500mW, wavelength 808 nm and spot diameter (*d*) 5 mm, controlled by a driver (Melles Griot 06DLD205) and lock-in amplifier (SR830) connected to a PC. The emitted radiation by the sample is focused and sent via two parabolic mirrors of 90º to an IR sensor (HgCdTe-JUDSON J15D12), of detection area 1 mm^2 and spectral range 2 to 12 μm. The

electrical signal obtained from the IR sensor is fed into a low-noise preamplifier connected to the the lock-in amplifier, which sends the results of the measurements to a PC via an IEEE interface using a virtual instrument developed in Lab-View™.
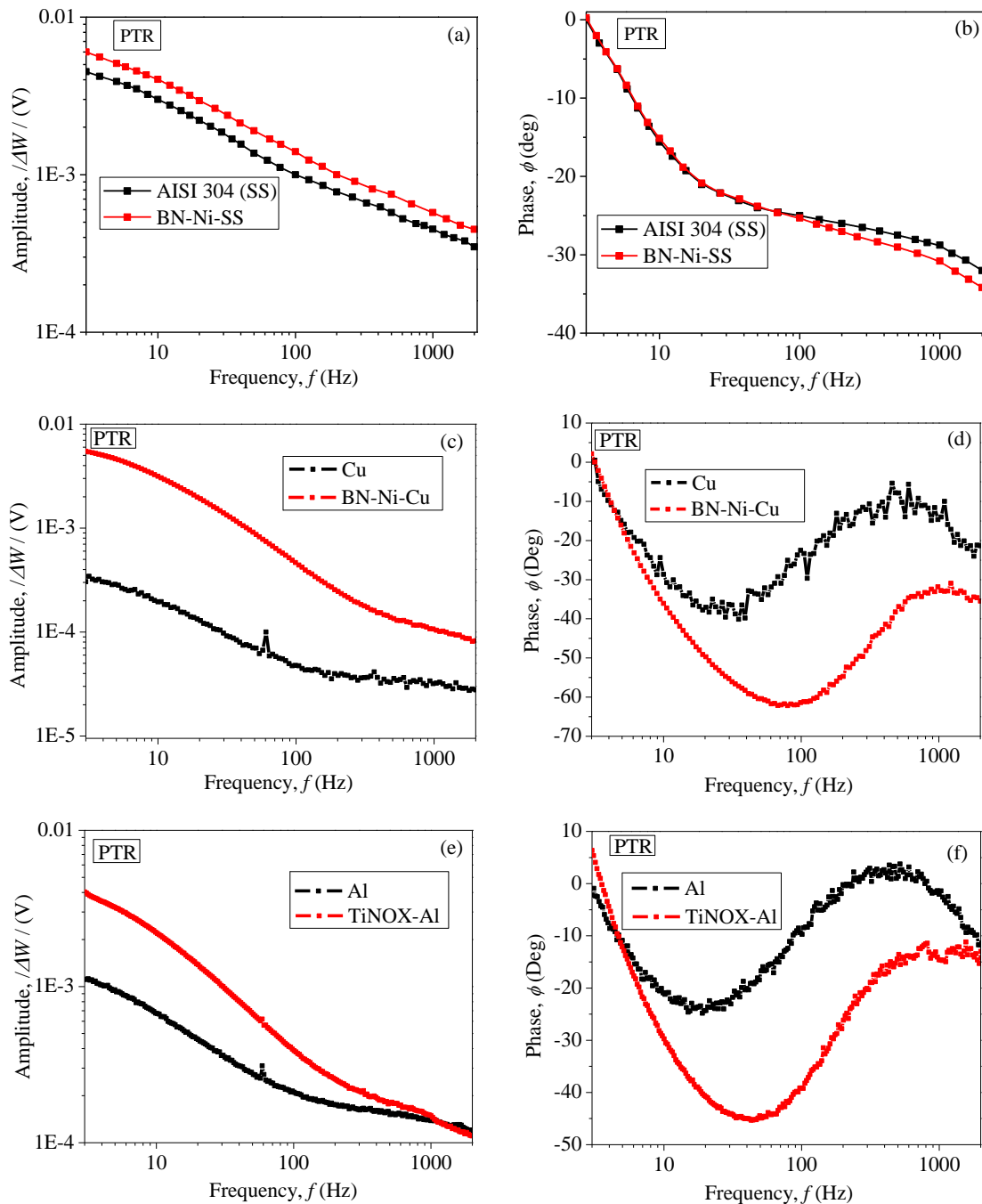
Fig. 3.3. PTR amplitude and phase signals obtained for the (a-b) BN-Ni-SS, (c-d) BN-Ni-Cu and (e-f) TiNOX-Al selective coatings (red lines), compared with those for the corresponding substrates (black lines).

The amplitude and phase signals, in the frequency range of 3 to 2000 Hz, obtained for the BN-Ni-SS (SS), BN-Ni-Cu (Cu) and TiNOX-Al (Al) samples (substrates) by using PTR technique are shown in Fig. 3.3.

The phase signal of stainless steel substrate (black line) in Fig 3.3(b) presents a monotonous change as the modulation frequency increases, such as the one-dimensional propagation model of Eq. (3.23c) predicts, for a low thermal diffusivity layer such as the AISI 304 ($\alpha = 3.48$ mm^{2}s^{-1}) [13]. The BN-Ni-SS sample (Thin film+substrate) shows identical behavior to the substrate, because the penetration depth of the thermal wave (μ) is much higher than the coating thickness (L). Therefore, the behavior of the photothermal signal for this sample in the considered modulation frequency range is dominated by the thermal properties of the substrate. Taking into account the behavior of the phase signal, it is possible to guarantee that the differences in the amplitude signals of the AISI 304 (SS) and BN-Ni-SS samples [See Fig. 3.3(a)] are directly related to the optical properties of the substrate (SS) and BN-Ni (coating) surfaces.

On the other hand, Fig. 3.3(d) and 3.3(f) show the behavior for those selective coatings deposited on substrates of high thermal diffusivity ($\alpha_{Cu} = 117$ mm^{2}s^{-1}, $\alpha_{Al} = 94$ mm^{2}s^{-1}) [14], which agrees with the prediction of Eq. (2.18) (chapter 2) for three-dimensional heat propagation in a one-layer sample [13,15]. In contrast to the 1D heat propagation case of the AISI304 (SS) susbstrate, the BN-Ni (TiNOX) thin film modifies the phase signals of copper (aluminum) substrate. The nature of these changes, such as will be shown in chapter 4 for several composed samples, are related with its surface structure, homogeneity and stoichiometry composition.

In order to achieve a nonambigous interpretation of the photothermal signals, these must be normalized with a reference signal (dividing the amplitudes and subtracting the phases), to eliminate any dependences with the sensor time response, optical configuration and electronic of the experimental setup. The normalized amplitude and phase signals of the solar selective coatings are shown in Fig. 3.4. For simplicity, the reference signals of each sample are the corresponding substrate.

In the Fig. 3.4(a), it can be observed that the normalized amplitude for the BN-Ni-SS sample is constant in the entire measured range of frequencies. In contrast, the amplitude measured for the BN-Ni-Cu and TiNOX-Al samples decreases upon lowering the frequency until reaching a constant value at 300 and 500 Hz, respectively.
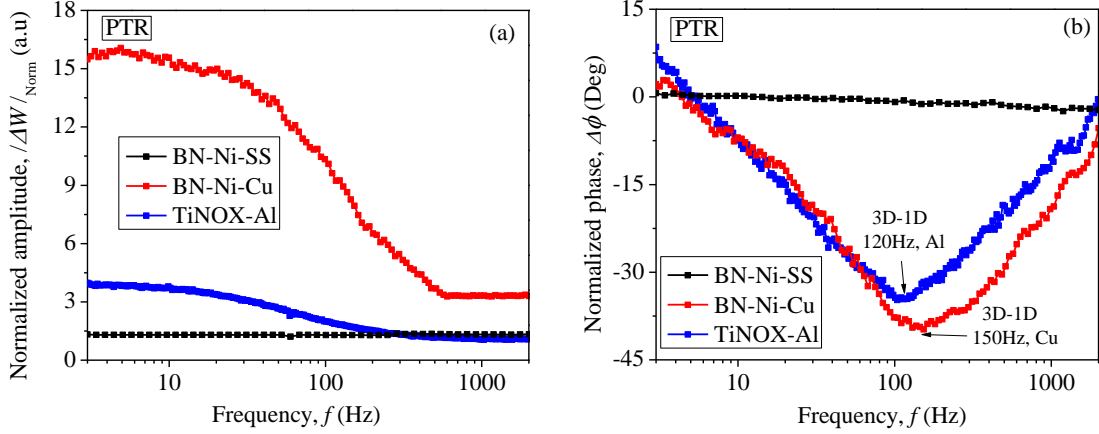
Fig. 3.4. PTR (a) normalized amplitude and (b) normalized phase signals of BN-Ni-SS (black line) BN-Ni-Cu (red line) and TiNOX-Al (blues line) selective coatings. The corresponding substrate signal has been used as reference for each case.

Fig. 3.4(b) shows a similar tendency for the phase signals. The BN-Ni-SS sample shows a nearly constant phase value, while for BN-Ni-Cu and TiNOX-Al at low modulation frequencies the lateral heat propagation (3D) dominates, and the phase shows the typical decay behavior (see Fig. 2.5 and 2.6). In contrast, for higher frequencies the phase increases to reach a constant value because at those frequencies the one-dimensional propagation regime is dominant. The change in the phase signal is at 120 Hz for TiNOX-Al and at 150 Hz for BN-Ni-Cu as predicted by the relation $10 \leq d/\mu$ for a diameter spot of 5 mm [16,17].

Assuming that both modulated temperatures (Thin film+substrate and substrate) in the one-dimensional heat propagation regime depend only on the thermal properties of the substrate [18,19], the normalized amplitude of the PTR signal should be constant, which only happens for the TiNOX-Al and BN-Ni-Cu samples at sufficiently high frequencies. Then, using Eq. (2.23c) in Eq. (3.1) the normalized amplitude under 1D heat propagation is given by

$$|\Delta W|_{Norm} = \frac{\epsilon_{sam}(1 - R_{sam})}{\epsilon_{ref}(1 - R_{ref})} \frac{\eta_{NR-sam}}{\eta_{NR-ref}}, \tag{3.2}$$

where ϵ_{sam} (ϵ_{ref}), $R_{sam}(R_{ref})$ and η_{NR-sam} (η_{NR-ref}) are the emissivity, optical reflectance, and light-into-heat conversion factors of the sample (reference), respectively. Eq. (3.2) predicts that if the coating is very thin, the PTR amplitude signal in the 1D heat propagation regimen must remain constant even when the modulation frequency of the laser is changed. Eq. (3.2) would allow the determination of the ratio of the emissivity of the sample and reference, if the reflectance and light-into-heat conversion factor quotient is known.

3.4. Optical reflectance spectroscopy

The emissivity calculation of the solar selective coatings by using Eq. (3.2), requires the values of optical reflectance of each surface to the incident laser wavelength (R_{sam}, R_{ref}), and the emissivity of the substrate (ϵ_{ref}). In this section, it will be shown how these optical parameters have been determine experimentally, and finally the results for the emissivity obtained with the optical (FTIR) and photothermal methodologies are compared.

3.4.1. Visible spectrum

Optical reflectance spectroscopy was performed by using a spectrometer (AVANTES, model AVASpec 2048) in the wavelength range from 400 to 900 nm using an integrating sphere (Ocean Optics, model ISP-50-8-R-GT, Spectral range: 200 to 2500 nm). The samples were illuminated with a Deuterium-Halogen light source (AVANTES, AvaLight-DH-S-BAL) with a wide spectrum from 200 to 2500 nm.

In Fig. 3.5, the optical reflectance spectrum in the range from 400 to 900 nm, for typical samples of the substrates of aluminum, stainless steel and copper, as well as for the coatings of BN-Ni and TiNOX are presented. It can be observed that the coatings have a significant absorbance, resulting in a decrease of the reflectance in all cases [4]. Moreover, the substrates of Cu and stainless steel (SS) show low reflectance for wavelengths below 600 nm, which is most likely related to oxides on the surface. For this work, given that the light beam used was a diode laser with wavelength of 808 nm, the reflectance at that wavelength was determined from the spectra and is indicated by a vertical line.
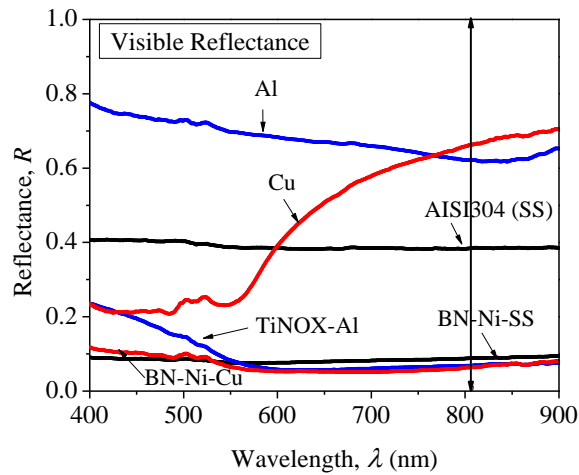
Fig. 3.5. Optical reflectance spectra obtained for Al, Cu and AISI304 (SS) substrates and TiNOX-Al, BN-Ni-Cu and BN-Ni-SS selective coatings.

3.4.2. Infrared spectrum

FTIR is the conventional optical methodology to characterize samples in the IR range [20,21]. In this case, a Perkin Elmer Spectrometer (FTIR), Model Frontier NIR-MED, equipped with an integrating sphere of 76.2 mm, with the interior surface coated with gold (Mid-IR integratIR of Pike technologies) has been used. The IR reflectance spectra obtained for the three selective coatings are shown in Fig. 3.6.
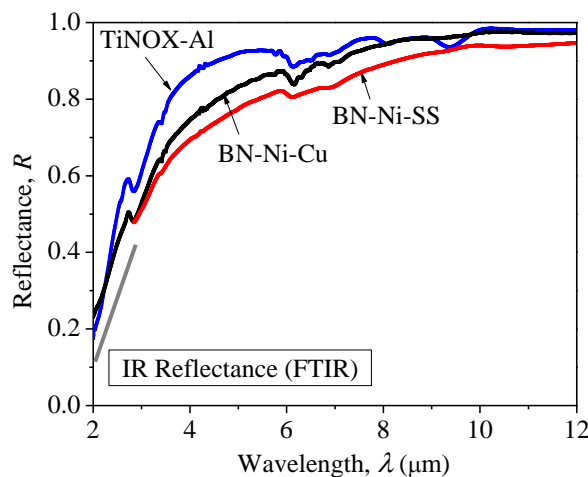

Fig. 3.6. FTIR reflectance spectrum of TiNOX-Al, BN-Ni-Cu and BN-Ni-SS selective coatings.

The emissivity of each sample in the spectral range of λ_1 to λ_2 is calculated by using Eq. (3.3) [6,22]

$$\epsilon = \frac{\int_{\lambda_1}^{\lambda_2}[1 - R(\lambda) - T_r(\lambda)]\Theta(\lambda,T)d\lambda}{\int_0^\infty \Theta(\lambda,T)d\lambda},$$ (3.3)

which compares the power emitted by the surface with the black body spectral radiance given by the Planck`s law $\Theta(\lambda,T) = C_1\lambda^{-5}/(e^{C_2/\lambda T} - 1)$ where $C_1 = 1.48 \times 10^{-15}\text{Wm}^2$, $C_2 = 1.43 \times 10^{-2}\text{m K}$, and $\sigma = 5.67 \times 10^{-8} \text{ Wm}^{-2}\text{K}^{-4}$.

Moreover, the factor $[1 - R(\lambda) - T_r(\lambda)]$ according to Kirchhoff`s law is the absorptance, which dependence on the spectral reflectance $R(\lambda)$ and transmittance $T_r(\lambda)$. In this case for the samples considered (Thin film+substrate) $T_r(\lambda) = 0$.

The light reflected by our samples studied by conventional optical spectroscopy in the visible and IR regimes showed that the surface of the samples is nearly specular, with minimal contributions of scattering and roughness [11,12]. This is in agreement with the manufacturer´s specifications of the TiNOx sample [18]. However, these are subjects deserving additional experimental and theoretical studies mostly in the IR spectra, in which both scattering and roughness are able to modify the photon trajectory and its interaction with the material's surface. This topic will be analyzed experimentally by using the PTR technique in chapter 4 by using the Kubelka-Munk function.

3.5. Emissivity measurements: PTR vs FTIR

Using the normalized PTR amplitude of each sample in Fig. 3.4, in the zone where it is independent of the modulation frequency, the optical reflectance at 808 nm [see Fig. (3.5)] and assuming that the light-into-heat conversion factor is equal to one for all the surfaces, the emissivity of each selective coating can be determined and compared with those obtained by the FTIR technique.

From Table. (3.1), it can be seen that the values for the emissivity from PTR and FTIR are in good agreement for the BN-Ni-SS sample, however, there is a clear discrepancy for the TiNOX-Al and BN-Ni-Cu samples: the values obtained from PTR are larger than those obtained from FTIR. These results suggest that the light-into-heat energy conversion efficiency is not equal to

1 for all cases, and that a determination of this factor is necessary for a correct interpretation of PTR signals. In the next sections, it will be shown how the combination of PTR with another photothermal technique, allows a correct determination of the emissivity.

Table 3.1. Normalized PTR signal, optical reflectance at 808 nm for the coating and substrate, the emissivity obtained by means of PTR, and those derived from FTIR for the TiNOX-Al, BN-Ni-Cu and BN-Ni-SS selective coatings. The emissivity of the reference samples ϵ_{Al} =7%, ϵ_{Cu} =4 %, ϵ_{SS} =15.4%, was measured with FTIR. The emissivity was calculated at room temperature in all cases. The experimental error was calculated by error propagation of each measurement.

| Selective coating | $\|\overline{\Delta W}\|_{Norm}$ | $R(808\ nm)$ | | PTR Emissivity (%) | FTIR Emissivity (%) |
		Selective coating	Substrate	$\eta_{NR-sam} = \eta_{NR-ref} = 1$	
TiNOX-Al	1.08	0.068	0.62	9.1 ± 0.3	5.0
BN-Ni-Cu	3.31	0.063	0.66	12.9 ± 0.9	7.5
BN-Ni-SS	1.31	0.088	0.38	16.4 ± 2.5	17.3

3.6. Photoacoustic spectroscopy (PAS) signals

The photoacoustic spectroscopy technique (PAS) consists in the measurement of the changes in the pressure of a gas in contact with a surface heating up periodically by a modulated heat source. A schematic diagram of the experimental setup for the PAS measurements is shown in Fig. 3.7. For these measurements we use a cell with two openings: on one side the cell is closed with a transparent quartz window, while on the opposite side the sample is attached with thermal paste closing the cell, in such a way that the coating faces the window.

The sample is illuminated through the window using a modulated laser light beam (808 nm) of spot diameter 8 mm. Some of the light is absorbed by the surface, resulting in the heating of the sample; as a consequence, a thin layer of air close to the surface is heated periodically at the same frequency of the light source. This effect known as thermal piston generates sound, which can be measured using a sensitive electret microphone attached to the air chamber [23,24]. The signal of microphone is sent to a lock-in amplifier (SR-830 DSP), and finally is stored as amplitude and phase in a computer.
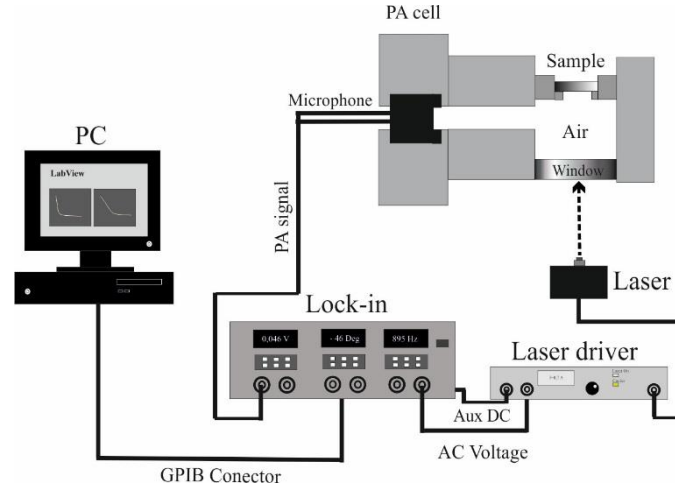
Fig. 3.7. Conventional experimental setup for photoacoustic spectroscopy (PAS) technique, and the photoacoustic (PA) cell.

The changes in the pressure of the photoacoustic signal are given by [see Eq. (1.8)] [25,26]

$$\Delta P = \gamma \frac{P_0}{l_g} \mu_{air} \frac{\theta}{\sqrt{2}(T + \theta_{dc})},$$

(3.4)

where P_0 [Nm^{-2}] is the pressure inside the cell, l_g (m) the thickness of the air layer heated by the sample, γ is the specific heat ratio of air and T (K) corresponds sample temperature, θ_{dc} is the dc temperature rise of the surface due to energy source, and θ is the modulated temperature, which depends on the absorption and light-into-heat conversion efficiency, and the thermal properties of the layers that compose the sample (see chapter 2). The photoacoustic measurements of the three solar selective coatings, normalized with the corresponding substrate signals are shown in Fig. 3.8.

Similar to the results from PTR [see Fig. 3.4(b)], the normalized amplitude of the PAS signals shows different behavior for BN-Ni-SS as compared to TiNOX-Al and BN-Ni-Cu, which can be explained by non-negligible 3D heat propagation in the Al and Cu substrates. In this case the laser wavelength was also 808 nm but with a spot diameter of 8 mm; therefore, the one-dimensional heat propagation condition $10 \leq d/\mu$ is satisfied for frequencies higher than 50 Hz for the TiNOX-Al and higher than 60 Hz for the BN-Ni-Cu sample, as seen in Fig. 3.8(b) [16,17]. Then, using the Eq. (2.23c) in Eq. (3.4) the normalized amplitude of Fig. 3.8(a) under 1D heat propagation is given by
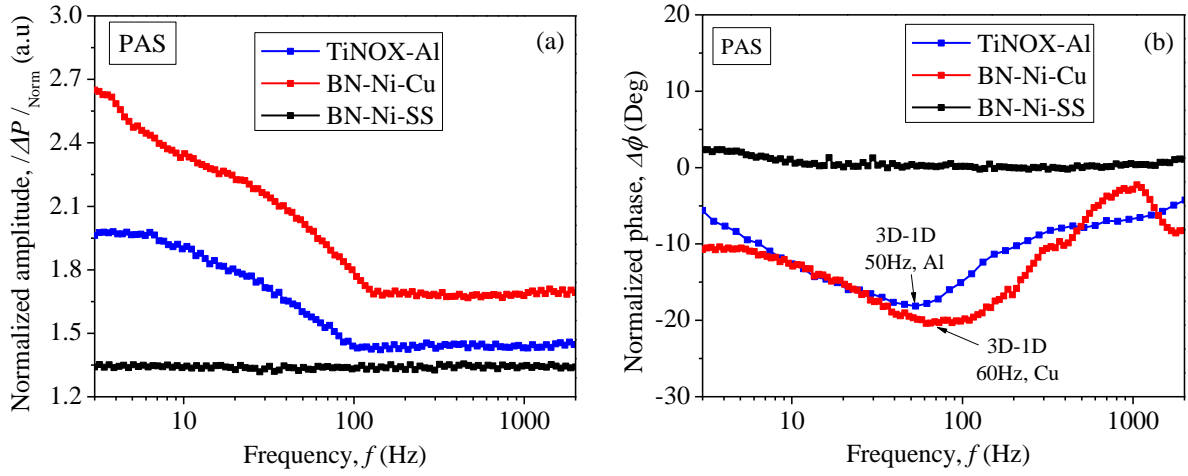
Fig. 3.8. PAS (a) normalized amplitude and (b) normalized phase signals of BN-Ni-SS (black line) BN-Ni-Cu (red line) and TiNOX-Al (blue line) selective coatings. The substrate signal has been used as reference for each case.

$$|\Delta P|_{Norm} = \frac{(1 - R_{sam})}{(1 - R_{ref})} \frac{\eta_{NR-sam}}{\eta_{NR-ref}}, \tag{3.5}$$

where R_{sam} and R_{ref} correspond to the optical reflectance of the sample and reference, respectively, at the pump wavelength of 808 nm. In this case, Eq. (3.5) does not depend on emissivity, but it is possible to determine another important optical property for a selective coating, which is the light-into-heat conversion factor. Similar to the situation for PTR, the normalized photoacoustic signal is constant when the substrate is thermally thick, and the coating is very thin, such that $L_1 \ll \mu_1$ [27]. At the modulation frequencies at which we are working, and for typical values of metal oxides, we can estimate that this behaviour occurs for films with thickness of a few microns or less.

It is worth mentioning that in obtaining Eq. (3.2) and (3.5), it is necessary that the quantity $T + \theta_{dc}$ is very similar for the sample and the reference. In our case this is a good approximation because T is around 300 K, and θ_{dc}, for sample and reference, is close to 3 K and 5 K, respectively, for a laser beam intensity of 500 mW. The error introduced by this approximation is within the total experimental error of our measurements.

3.6.1. Light-into-heat conversion efficiency and emissivity calculation: PTR-PAS vs FTIR

From the experimental values of the normalized amplitude signals presented in Fig. 3.9(a), where are independent of the modulation frequency, and using the measured optical reflectance at 808 nm for each surface (Fig. 3.5), the ratio between the quantum efficiency of the selective coating and the substrate is obtained using Eq. (3.5) [20,28], and the results are summarized in Table. 3.2.

Table 3.2. Values of the normalized PAS signal, the optical reflectance for the coatings and substrates, and the relative optical-to-thermal (non-radiative) energy conversion efficiency between selective coatings based on TiNOX and BN-Ni and a metallic substrate of Al, Cu and stainless steel. The experimental error was calculated by error propagation using the parameters involved in the measurements.

Selective coating	$|\overline{\Delta P}|_{Norm}$	$R(808\ nm)$		$\eta_{NR-sam}/\eta_{NR-ref}$
		Selective coating	Substrate	
TiNOX-Al	1.43	0.068	0.62	0.58 ± 0.04
BN-Ni-Cu	1.68	0.063	0.66	0.61 ± 0.04
BN-Ni-SS	1.34	0.088	0.38	0.91 ± 0.03

The normalized PAS signal is a number in the range from 1 to 2, and the quotient of the optical-to-thermal (non-radiative) energy conversion efficiency of the sample and the reference $\eta_{NR-sam}/\eta_{NR-ref}$ is found to be close to 1 for the BN-Ni-SS sample, but significantly lower than 1 for the TiNOX-Al and BN-Ni-Cu samples. It should be noted that a pure metal surface generally has a low optical absorption quantum yield (radiation induced) across the visible and infrared wavelength range and, as consequence, is a low light emitter; hence, the optical-to-thermal energy conversion efficiency is near unity and the amount of heat generated is related to the optical absorption [29]. In our case, the substrates have been exposed to normal ambient conditions resulting in the presence of oxides, which reduces the optical reflectance as shown in Fig. 3.5 and, as a consequence, the light-into-heat conversion factor. This happens especially with the copper reference, which has a strong tendency to form oxides on the surface, as compared with the AISI 304 substrate. These are key factors defining the light-into-heat conversion efficiencies of the Cu and AISI 304 surfaces and, therefore, the values of $\eta_{NR-sam}/\eta_{NR-ref}$ for BN-Ni-Cu and BN-Ni-SS samples cannot be equal. Additionally, possible structural differences during electrodeposition of the BN-Ni coating on the different

substrates have not been taken account, which can generate additional effects in the light-into-heat conversion process.

In order to obtain the emissivity of the samples, we use the obtained ratios of the light-into-heat conversion efficiencies of the coatings and substrates to incorporate these in Eq. (3.2). The results are presented in Table. 3.3.

Table 3.3. Emissivity determined by, the quotients of the light-into-heat conversion factor from PAS, the PTR-PAS emissivity and the ones obtained by means of FTIR for the TiNOX-Al, BN-Ni-Cu and BN-Ni-SS selective coatings. The emissivity of the references is $\varepsilon_{Al} = 7$ %, $\varepsilon_{Cu} = 4$ %, $\varepsilon_{Steel} = 15.4$ %, and was measured with FTIR. The experimental error was calculated by error propagation of the parameters involved in each measurement.

Selective coating	$\|\overline{\Delta W}\|_{Norm}$	Only PTR Emissivity (%) $\eta_{NR-sam} = \eta_{NR-ref} = 1$	$\dfrac{\eta_{NR-sam}}{\eta_{NR-ref}}$	PTR-PAS Emissivity (%)	FTIR Emissivity (%)
TiNOX-Al	1.08	9.1 ± 0.3	0.58 ± 0.04	5.31 ± 0.25	5.0
BN-Ni-Cu	3.31	12.9 ± 0.9	0.61 ± 0.04	7.87 ± 0.96	7.5
BN-Ni-SS	1.31	16.4 ± 2.5	0.91 ± 0.03	15.0 ± 2.4	17.3

The results in Table (3.3) show that by introducing the light-into-heat conversion factors obtained from PAS measurements, the emissivity is very similar to the results obtained from FTIR reflectance spectroscopy for all these diverse selective coatings on different substrates. Note that all values obtained for the emissivity are strongly dependent on the light-into-heat conversion ratio, and the agreement between the FTIR results and the photothermal results confirms that the quantity $\eta_{NR-sam}/\eta_{NR-ref}$ can be far from unity for real samples.

These last results show that photothermal measurements that depend on the multiplicative factor appearing in Eq. (3.2) and Eq. (3.5) can only approximate realistic values when considering the values of the ratio η_{sam}/η_{ref} equal to 1. These results open the possibility of performing a rigorous study of optical-to-thermal energy conversion efficiency factors for real systems, which would require measurements of different samples and surfaces considering factors such as the presence of oxides [30].

3.7. Emissivity of cermet-based solar selective absorber of molybdenum and aluminum oxide by using PTR technique.

In order to confirm the dependence of the amplitude signal with the light-into heat conversion efficiency (η_{NR}) multi-layer cermet based on molybdenum (Mo) and alumina (Al$_2$O$_3$) samples has been studied optically, by using PTR in transmission configuracion (rear illumination).

Figure. 3.9(a) shows the structure of the multilayer coating under study. In this case a Mo layer of 300 nm deposited on borosilicate glass is used as IR-reflector. The absorber coating is a bilayer metal-dielectric composite (cermet) of 100 nm, which consists of two ceramic matrices with molybdenum nanoparticles impregnate in Al$_2$O$_3$ at the volumetic fraction of 40% for the first layer and 10 % for the second one. This coating is nearly transparent in the IR region (> 3 µm), and highly absorbent in the solar spectrum due to interference effects between the two absorber layers [34,35]. On the top of the sample 40 nm of alumina is included as anti-reflective and protective layer.

The samples were prepared by RF magnetron sputtering technique. The IR reflective layer of Mo (300 nm) was deposited at 7 mTorr of argon preasure and 400 W of power by using a molybdenum target (20 x 5 cm^2) of 99.999 % purity. The cermet-based layers have been grown by the co-sputtering method, in which both materials (Mo and Al$_2$O$_3$) are deposited simultaneously while the substrate (Mo-Glass) rotates at 30 rpm to improve the homogenity of the layer. The first cermet (40%) uses a power of 70 W for 2 minutes while the second one (10%) 40 W for 3 minutes.
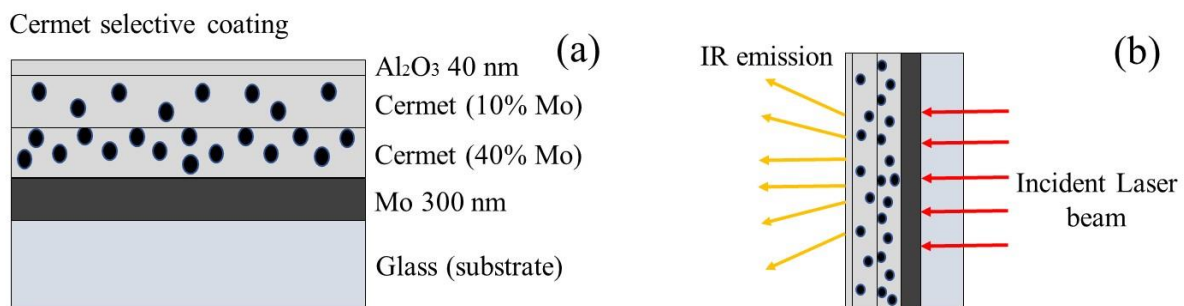

Fig. 3.9. (a) Scheme of the cermet-based sample studied and (b) rear illumination used in PTR technique for emissivity calculation.

As the borosilicate glass is transparent in the visible spectrum, it is possible to illuminate the Mo layer for all samples (and reference) as shown in Fig. 3.9(b). This allows to associate the normalized amplitude signal directly with the emissivity differences of each surface [see Eq. (3.6)] due to $\frac{1-R_{sam}}{1-R_{ref}} = 1$ and $\frac{\eta_{NR-ref}}{\eta_{NR-sam}} = 1$

$$|\Delta W|_{Norm} = \frac{\epsilon_{sam}}{\epsilon_{ref}}.$$ (3.6)

The Fig. 3.10 shows the phase and amplitude signals of three cermet-base samples, which are composed as follows: 1. Cermet-1 (Cermet 40% - Mo – Glass), 2. Cermet-2 (Cermet 40%+Cermet 10% - Mo - Glass) and 3. Cermet selective coating [see Fig. 3.10(a)].
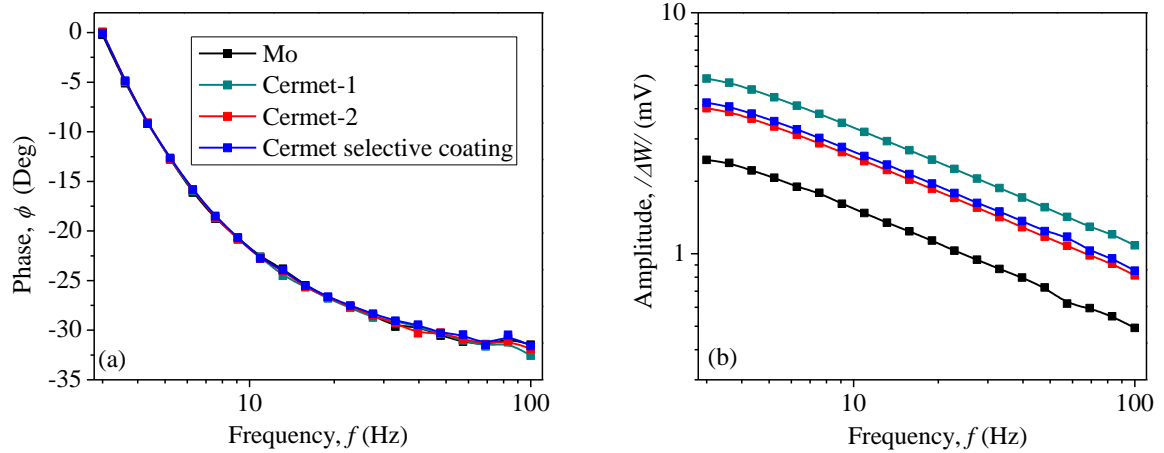
Fig. 3.10. PTR (a) phase and (b) amplitude signals for rear illumination, obtained for the reference (Mo-Glass), Cermet-1, Cermet-2 and cermet selective coating samples.

The phase signals of the reference (Mo-Glass) and samples present identical behavior, with a monotonous change as the modulation frequency increases, which, such as for the BN-Ni sample deposited on AISI 304 [see Fig. 3.3(b)], is due to the one-dimesional heat propagation of the substrate ($\alpha_{Glass} = 0.57$ mm^{2}s^{-1}) [13]. Taking into account this behavior, it is possible to guarantee that the differences in the amplitude signal of Fig. 3.10(b) are directly related to the optical properties of each surface.
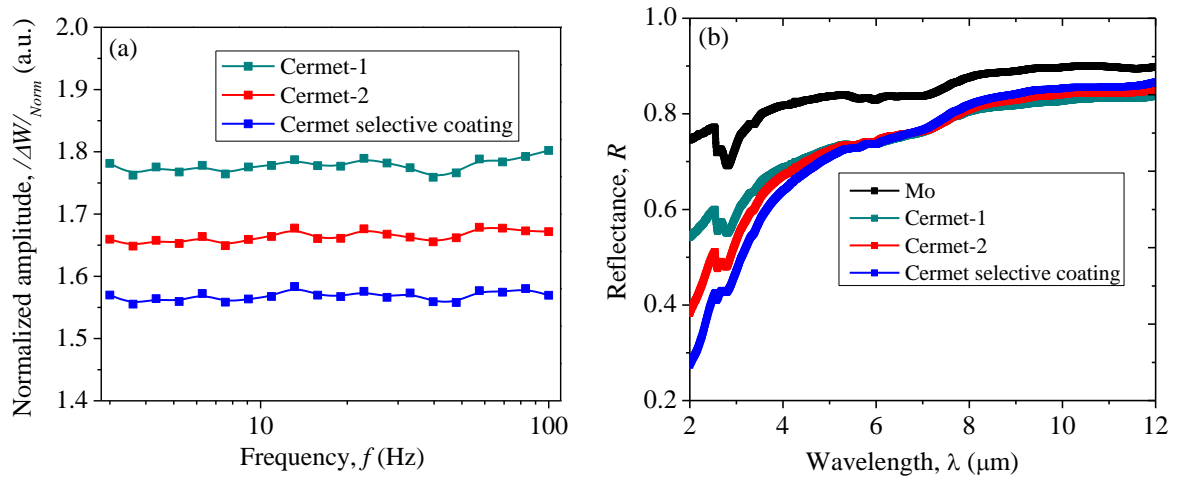
Fig. 3.11. (a) PTR normalized amplitude signals for rear illumination and (b) IR reflectance spectra obtained for Cermet-1, Cermet-2 and Cermet selective coating samples (and reference).

The normalized signals obtained by dividing the amplitude signal of each sample with the reference sample (Mo-Glass) are shown in Fig. 3.11(a). The normalized signals are independent of the modulation frequency, which allows to determine directly the emissivity of each surface by using Eq. (3.6). Moreover Fig. 3.11(b) shows the IR reflectance spectra of samples and reference in order to compare the results.

Table 3.4. Normalized PTR signal, emissivity obtained by mean of PTR, and that derived from FTIR for the cermet selective coatings. The emissivity of the references is $\varepsilon_{Mo} = 12.3$ % and was measured with FTIR. The experimental error was calculated by error propagation of the parameters involved in each measurement.

Sample	$|\overline{\Delta W}|_{Norm}$	PTR emissivity (%)	FTIR emissivity (%)
Cermet-1	1.77	21.7 ± 1.3	19.7
Cermet-2	1.65	20.3 ± 1.1	18.9
Cermet selective coating	1.55	19.1 ± 1.2	18.1

The emissivities calculated by PTR and FTIR are shown in Table. 3.4. As expected, these values show good agreement, which confirm that by using the PTR technique in transmission configuration, under the one-dimensional heat propagation approximation, the dependence of the normalized amplitude signal with the other optical properties of the selective coatings is eliminated.

3.8. Conclusions

The emissivity of selective coatings for solar-to-thermal energy conversion have been determined for a wide range of coatings and substrates using photothermal characterization. The methodology involves two photothermal techniques, photothermal radiometry and photoacoustic spectroscopy, which allows to determine the relative light-into-heat conversion factor and the emissivity of the selective coatings. The crucial role of the light-into-heat conversion factor in the determination of optical properties of materials has been illustrated. This methodology is useful for samples with one-dimensional heat propagation in the thermally thick region, which can be identified by performing the measurements as a function of frequency. The results for the emissivity from the combined PTR and PAS measurements show very good agreement with the results from FTIR reflectance spectroscopy, indicating that this methodology can be a good alternative for measuring optical properties of selective coatings of relevance in solar thermal energy systems. From the phase signal it has been shown that selective coatings modify the photothermal signals of substrates of high thermal diffusivity (Al and Cu) in a specific frequency range, which is related with the structure, homogeneity and composition of the thin film and will be analyzed in chapter 4 in more detail.

References.

[1] Kalogirou, S. A. (2004). Solar thermal collectors and applications. *Progress in energy and combustion science*, *30*(3), 231-295.

[2] Erben, E., & Tihanyl, B. A. (1984). Solar-selective absorber coatings for high-temperature application. *Industrial & engineering chemistry product research and development*, *23*(4), 659-661.

[3] Valleti, K., Krishna, D. M., & Joshi, S. V. (2014). Functional multi-layer nitride coatings for high temperature solar selective applications. *Solar Energy Materials and Solar Cells*, *121*, 14-21.

[4] Jaworske, D. A., & Shumway, D. A. (2003, January). Solar selective coatings for high temperature applications. In *AIP Conference Proceedings* (Vol. 654, No. 1, pp. 65-70). AIP.

[5] Niklasson, G. A., & Granqvist, C. G. (1984). Optical properties and solar selectivity of coevaporated $Co-Al_2O_3$ composite films. *Journal of applied physics*, *55*(9), 3382-3410.

[6] Ienei, E., Milea, A. C., & Duta, A. (2014). Influence of spray pyrolysis deposition parameters on the optical properties of porous alumina films. *Energy Procedia*, *48*, 97-104.

[7] Zambrano-Arjona, M. A., Medina-Esquivel, R., & Alvarado-Gil, J. J. (2007). Photothermal radiometry monitoring of light curing in resins. *Journal of Physics D: Applied Physics*, *40*(19), 6098.

[8] Walther, H. G. (2002). Surface roughness influence on photothermal radiometry. *Applied surface science*, *193*(1-4), 156-166.

[9] Othonos, A., Nestoros, M., Palmerio, D., Christofides, C., Bes, R. S., & Traverse, J. P. (1998). Photothermal radiometry on nickel (pigmented aluminium oxide) selective solar absorbing surface coatings. *Solar energy materials and solar cells*, *51*(2), 171-179.

[10] Cahen, D., Bults, G., Garty, H., & Malkin, S. (1980). Photo acoustic in life sciences. *Journal of biochemical and biophysical methods*, *3*(5), 293-310.

[11] Almeco Group, TiNOX energy. http://www.almecogroup.com/uploads/1172-ALMECO_TinoxEnergy_ENG_S402_07_2014_mail.pdf. Accessed 12 October 2015.

[12] Rosencwaig, A., & Gersho, A. (1976). Theory of the photoacoustic effect with solids. *Journal of Applied Physics*, *47*(1), 64-69.

[13] Lizama-Tzec, F. I., Macías, J. D., Estrella-Gutiérrez, M. A., Cahue-López, A. C., Arés, O., De Coss, R., & Oskam, G. (2015). Electrodeposition and characterization of nanostructured

black nickel selective absorber coatings for solar–thermal energy conversion. *Journal of Materials Science: Materials in Electronics*, *26*(8), 5553-5561.

[14] Touloukian, Y. S., & Ho, C. Y. (1970). Specific heat. Nonmetallic solids. *Thermophysical properties of matter-The TPRC Data Series, New York: IFI/Plenum, 1970-, edited by Touloukian, YS e (series ed.); Ho, CY e (series tech. ed.)*.

[15] Almond, D. P., & Patel, P. M. (1996). Photothermal Science and Techniques in Physics and its Applications vol 10, ed ER Dobbs and SB Palmer.

[16] Garcia, J. A., Mandelis, A., Farahbakhsh, B., Lebowitz, C., & Harris, I. (1999). Thermophysical properties of thermal sprayed coatings on carbon steel substrates by photothermal radiometry. *International journal of thermophysics*, *20*(5), 1587-1602.

[17] Paoloni, S., & Walther, H. G. (1997). Photothermal radiometry of infrared translucent materials. *Journal of applied physics*, *82*(1), 101-106.

[18] Yanguas-Gil, A., & Wormeester, H. (2013). Relationship between surface morphology and effective medium roughness. In *Ellipsometry at the Nanoscale* (pp. 179-202). Springer, Berlin, Heidelberg.

[19] Mandelis, A. (2013). Green Functions of One-Dimensional Thermal-Wave Fields. In *Diffusion-wave fields: mathematical methods and Green functions*. Springer Science & Business Media.

[20] Ramírez-Rincón, J. A., Ares-Muzio, O., Macias, J. D., Estrella-Gutiérrez, M. A., Lizama-Tzec, F. I., Oskam, G., & Alvarado-Gil, J. J. (2018). On the use of photothermal techniques for the characterization of solar-selective coatings. *Applied Physics A*, *124*(3), 252.

[21] Gomez-Heredia, C. L., Ramirez-Rincon, J. A., Ordonez-Miranda, J., Ares, O., Alvarado-Gil, J. J., Champeaux, C., & Joulain, K. (2018). Thermal hysteresis measurement of the VO_2 emissivity and its application in thermal rectification. *Scientific reports*, *8*(1), 8479.

[22] Trotter, D. M., & Sievers, A. J. (1980). Spectral selectivity of high-temperature solar absorbers. *Applied optics*, *19*(5), 711-728.

[23] Rosencwaig, A., & Hildum, E. A. (1980), *Phys. Rev. B*, 22, 3301-3307.

[24] Martínez-Torres, P., & Alvarado-Gil, J. J. (2011). Photoacoustic monitoring of thermal wave interference effects during the formation of polymeric thin films from solutions. *Applied Physics A*, *105*(4), 975-986.

[25] Vales-Pinzon, C., Ordonez-Miranda, J., & Alvarado-Gil, J. J. (2012). Photothermal characterization of the thermal properties of materials using four characteristic modulation frequencies in two-layer systems. *Journal of Applied Physics*, *112*(6), 064909.

[26] Almeco Group, Product specifications TiNOX energy. http://www.almecogroup.com/uploads/1117-Specification_TiNOX_energy_EN_RD_V020614_rev1.pdf. Accessed 12 October 2015

[27] Gomez-Heredia, C. L., Macias, J., Ordonez-Miranda, J., Ares, O., & Alvarado-Gil, J. J. (2017). Diffusive-to-ballistic transition of the modulated heat transport in a rarefied air chamber. *AIP Advances*, *7*(1), 015032.

[28] Pawlak, M., Gibkes, J., Fotsing, J. L., Zakrzewski, J., Malinski, M., Bein, B. K., & Marasek, A. (2004, October). Study of optical properties of Zn-Be-Te mixed crystals by means of combined modulated IR radiometry and photoacoustics. In *Journal de Physique IV (Proceedings)* (Vol. 117, pp. 47-56). EDP sciences.

[29] Mandelis, A., Vanniasinkam, J., Budhudu, S., Othonos, A., & Kokta, M. (1993). Absolute nonradiative energy-conversion-efficiency spectra in $Ti_{3+}:Al_2O_3$ crystals measured by noncontact quadrature photopyroelectric spectroscopy. *Physical Review B*, *48*(10), 6808.

[30] Richardson, H. H., Carlson, M. T., Tandler, P. J., Hernandez, P., & Govorov, A. O. (2009). Experimental and theoretical studies of light-to-heat conversion and collective heating effects in metal nanoparticle solutions. *Nano letters*, *9*(3), 1139-1146.

[31] Mandelis, A. (2013). Cartesian Thermal-Wave Fields in Three and Two Dimensions. In *Diffusion-wave fields: mathematical methods and Green functions*. Springer Science & Business Media.

[32] Chan, I. C. W., & Beaudoin, M. (2009). Extension of the Rosencwaig–Gersho–Fernelius photothermal deflection spectroscopy model to account for multiple reflections in epitaxial samples. *Journal of Applied Physics*, *106*(10), 103510.

[33] Matvienko, A., Mandelis, A., Jeon, R. J., & Abrams, S. H. (2009). Theoretical analysis of coupled diffuse-photon-density and thermal-wave field depth profiles photothermally generated in layered turbid dental structures. *Journal of Applied Physics*, *105*(10), 102022.

[34] Sakurai, A., Tanikawa, H., & Yamada, M. (2014). Computational design for a wide-angle cermet-based solar selective absorber for high temperature applications. *Journal of Quantitative spectroscopy and radiative transfer*, *132*, 80-89.

[35] Zhao, S., & Wäckelgård, E. (2006). Optimization of solar absorbing three-layer coatings. *Solar energy materials and solar cells*, *90*(3), 243-261.

4. Analysis of composite materials by means of photothermal radiometry technique

4.1. Introduction

In chapter 3 we analyzed the changes induced by selective coatings ($<$ 1 µm), in the photothermal signals (amplitude and phase) of metallic substrates. At the modulation frequencies where the one-dimensional propagation model is valid for a specific material, it has been possible to associate the normalized amplitude to the optical properties of the surfaces (thin film and substrate), allowing us determining with good accuracy the emissivity of layers, which is a crucial paramenter in solar thermal energy applications. In this chapter, the nature of the optical phenomena that modify the thermal profiles of substrates will be studied, with a special emphasis on the morphology and composition of its surfaces.

4.2. Photothermal characterization of carbonyl iron/polyester composites

The correlation of the photothermal signals with the structural composition of a material is analyzed in polyester resin samples filled at different volumetric fractions (V_f) with iron

carbonyl (FeCO), by using photothermal radiometric technique (PTR) in the front illumination configuration.

4.2.1. Structural characteristics

The samples were prepared dispersing iron carbonyl powder, which is composed of spheres of 97% iron coated with 3% of carbon, of a size of about $2\,\mu$m (Sigma Aldrich), in a polyester resin matrix (RP-RESINMEX). The liquid composite was mixed with a catalyst using an ultrasonic tip to obtain a homogeneous composite, to be subsequently deposited in a cylindrical mold. After polymerization, the samples were polished on both faces in order to obtain a thickness of about 1 mm.

Six different volumetric fractions (V_f) of FeCO were prepared (0.05, 0.12, 0.27, 0.33, 0.41, 0.5, 054) to monitor the evolution of the PTR signals as the iron carbonyl fills the structure of the polyester resin. Figure 4.1 shows several SEM profiles micrographs at different magnifications of the matrix and samples under study.
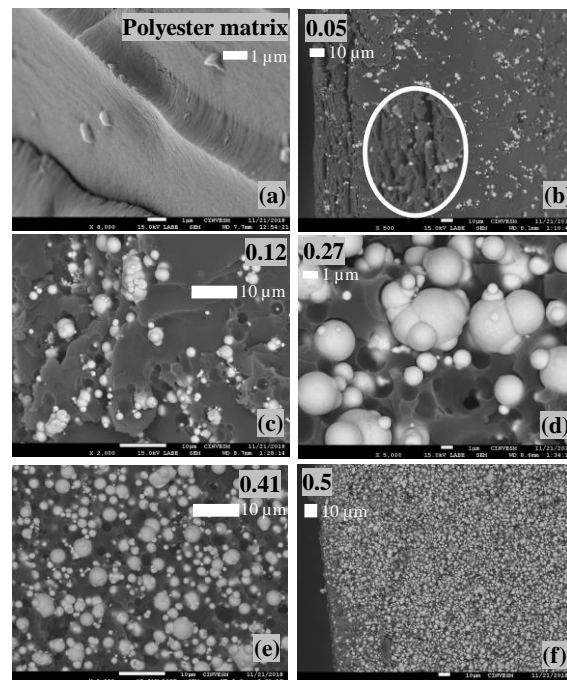

Fig. 4.1. Profiles SEM micrographs of polyester resin filled with several concentration of iron carbonyl.

According to the images of Fig. 4.1, the polyester resin (a) is composed of nanometric fibers (ester chains) forming flakes of different randomly distribution sizes, making the generation of frontal thermal waves difficult [see Figures 4.1(b) and 4.1(c)]. As the concentration of FeCO is increased, the spheres connect forming chains (d), which additionally modify the thermal and electrical conductivity of the polyester resin [1]. Changes in microstructure can been seen comparing images 4.1.(c) and 4.1.(e), where flakes are not clearly identifyied. For the highest concentration [see Fig. 4.1.(f)], the resin looks uniformly filled by the carbonyl iron, therefore, samples of homogeneous structure with different optical and thermal properties compared with those of the lowest carbonyl iron concentration are expected [2,3].

4.2.2. Thermal properties by means of flash method

Thermal properties of the samples were obtained by using the well-known flash method in front configuration. This technique consists in the fast and uniform heating up of the sample surface with a short pulse (~ 20 ms), followed by the monitoring of the cooling profile by using a thermal camera [4]. The heat source is a flash lamp (Speedotron 206VF) working at 4.8 KJ per pulse which illuminates all sample surface (front heat propagation), while the detection is performed using an IR camera (In-fraTec 8320) of spectral range 3-5 µm.

By solving the heat diffusion equation in the Laplace domain for one-dimensional heat propagation, the thermal diffusivity and thermal effusivity of the material can be obtained [4,5]. For the first case, the sample is in thermal contact with a medium of low effusivity (air), while for the second one, the back face is put in contact with a liquid (water) in order to generate a better thermal contrast. A summary of the thermal properties of the samples is shown in Table 4.1. More details about thermal characterization can be found in Ref [6].

Table 4.1. Thermal properties of carbonyl iron/polyester composites for several volumetric concentrations. Values have been obtained by the flash method described in Ref [6].

V_f	Thickness (mm)	Thermal diffusivity (mm^2s^{-1})	Thermal Effusivity 10^3 [$Ws^{1/2}m^{-2}K^{-1}$]	Thermal Conductivity ($Wm^{-1}K^{-1}$)
0.05	1.01	0.12	0.70	0.25
0.12	1.0	0.16	0.92	0.37
0.27	0.65	0.22	1.31	0.61
0.33	1.05	0.26	1.46	0.74
0.41	1.05	0.35	1.77	1.04
0.5	1.0	0.52	2.11	1.52
0.54	1.45	0.59	2.26	1.72

4.2.3. PTR signals of carbonyl iron/polyester

Based on the thermal diffusivity (α) and thickness (L) values of each sample, at the lower modulation frequency used in this work (3 Hz), the thermal diffusion length (μ) satisfies that: 1) all samples are in the thermally thick regime i.e. $2\mu < L$, and 2) they satisfy the one-dimensional heat propagation condition obtained in chapter 1 ($5\mu < 2a$). Therefore, for front illumination ($z = 0$), using Eq. (1.4) and (2.23), the photothermal signal is given by,

$$\Delta W = 4\epsilon\sigma_B(T + \theta_{dc})^3 \frac{I_0(1-R)\eta_{NR}}{k\,\sigma}\left[\frac{1+e^{-2\sigma L}}{1-e^{-2\sigma L}}\right], \tag{4.1}$$

and taking into account that $2\mu < L$, which implies that $e^{-2\sigma L} \ll 1$, Eq. (4.1) reduces to

$$\Delta W = 4\epsilon\sigma_B T^3 \frac{I_0(1-R)\eta_{NR}}{2\varepsilon}(1-i), \tag{4.2}$$

where ϵ is the emissivity of the surface, σ_B [$Wm^{-2}K^{-4}$] the Stefan-Boltzmann constant, T [K] ($T \gg \theta_{dc}$) the sample temperature, I_0 [Wm^{-2}] laser intensity, R and η_{NR} are the optical

reflectance and light-into-heat conversion efficiency of the surface at the laser wavelength (808 nm) respectively; ε (k/α) [$Ws^{1/2}$ $m^{-2}K^{-1}$] is the thermal effusivity, and i the complex unity.

According to Eq. (4.2), the argument [$\phi = \tan^{-1}(-Re\,[\Delta W]/Im\,[\Delta W])$] of the photothermal signal is independent of the optical and thermal properties of the sample, therefore, the phase signal of those materials that satisfy the thermally thick limit and the one-dimensional heat propagation are expected to show the same behavior.
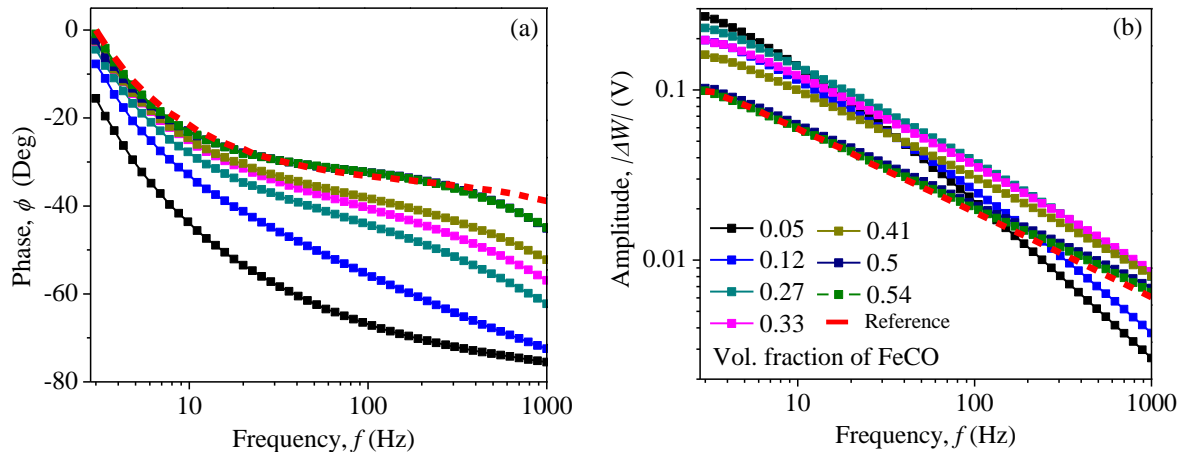

Fig. 4.2. (a) phase and (b) amplitude signals of iron carbonyl/polyester composites for several volumetric concentrations. PTR reference signal correspond to glassy carbon Sigradur-K.

Fig. 4.2 shows the phase and amplitude signals of the polyester resins at different volumetric fractions (V_f) of carbonyl iron (FeCO), as well as of a thermally thick reference (Sigradur-K: Glassy Carbon, L =1.9 mm, $\alpha = 1.86\,mm^2s^{-1}$, $k = 7.96\,Wm^{-1}K^{-1}$) [7], which has been included to compare the thermal profiles. In Fig. 4.2(a), only the highest concentrations of FeCO has a similar phase signal compared with the phase of the reference, i.e. those samples that, according to SEM micrographs of Fig. 4.1, present the most homogeneous structures. This implies that samples with volume fractions of 0.5 and 0.54 satisfy Eq. (4.2), which can be confirmed from amplitude signals of Fig. 4.2(b), because according to the model, these differences should be independent of the modulation frequency, and are proportional to the multiplicative optical and thermal factors, $\epsilon\,(1-R)\eta_{NR}$ and $1/\varepsilon$, respectively. As the volume fraction (V_f) of the filler decreases ($V_f < 0.41$), the phase delay between samples and reference increases, mostly at the highest modulation frequencies.

The anomalous differences in the photothermal profiles of polyester resins at low concentrations of FeCO can be qualitatively understood by analyzing the propagation of the thermal wave (TW) generated at the sample surface, as shown in Fig. 4.3.
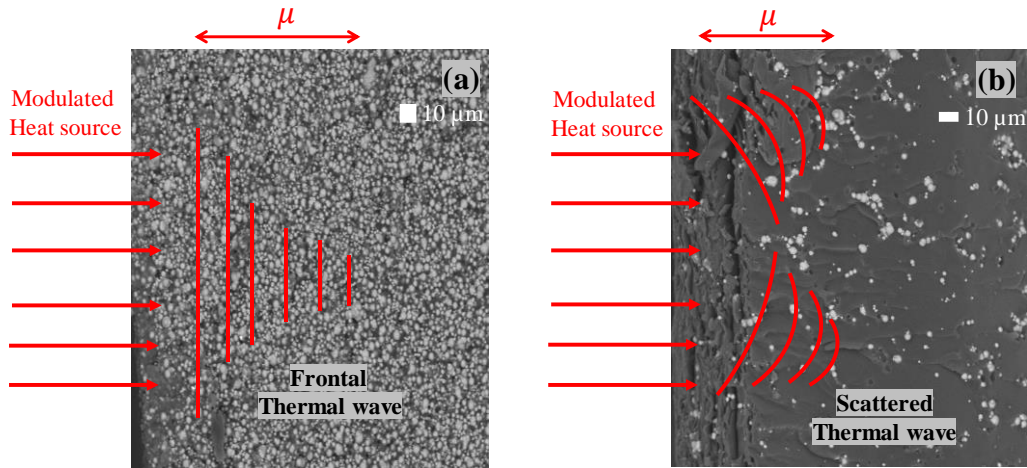

Fig. 4.3. Scheme of the thermal wave propagation in materials of (a) homogeneous and (b) irregular structure. Black and white images correspond to SEM micrographs of polyester resin for volumetric fraction of 0.5 (left) and 0.05 (right) of FeCO.

In the one-dimensional heat propagation regime, for homogeneous structures as shown in Fig 4.3(a), the thermal wave generated by the heat source propagates across the material as a smooth "wavefront", with a thermal diffusion length given by $\mu = \sqrt{\alpha/\pi f}$. In the case of polyester resin, at low FeCO concentrations [Fig 4.3(b)], the irregularity of the structure generates in the TW a tendency to propagate in different directions, with a non-smooth "wavefront", which reduces the effective value of μ, increasing the phase delay in relation to the reference, such as observed in Fig. 4.2(a). As the FeCO fills the polyester structure (see Fig. 4.2), the thermal diffusion length increases, and the one-dimensional heat propagation is satisfied.

The thermal characterization of composite materials by using PTR technique has been reported by Diaz. *et. al.* in Ref [8]. In this case, the FeCO was dispersed in an agar matrix at several mass fractions between 0 - 30%. In contrast to a polyester matrix, it has been reported that Agar shows a compact structure when forming a composite, allowing a smooth propagation (front propagation) of the thermal wave, even at low FeCO concentrations, and therefore in that case the characterization of the samples can be performed using a simple model. In the case of the flash method used to obtain the thermal properties of the polyester resin composites of Table.

4.1, the heat source (flash lamp) induces mostly (1D) heat propagation through the material, and structural anomalies are not detected [5,6]. In contrast, PTR measurements exhibit a modulation frequency dependence in the thermal wave diffusion length (μ), which has to fulfill the inequality relationship with the size of the laser spot (2a), to be close or far from the 1D behavior as discussed in chapter 2.

4.2.4. Optical properties

In addition to the changes in the thermal properties of polyester resin as the volumetric fraction of carbonyl iron increases (see Table 4.1), those samples also exhibit changes in the optical properties (visible and IR spectra) due to the presence of the filler. Figure 4.4 shows the reflectance spectra as a function of volumetric fraction of FeCO at (a) 808 nm (laser wavelength), and (b) in the IR region. Both measurements have been done by using the spectrometers described in Sec. 3.4 of chapter 3.

The presence of carbonyl iron in the matrix increases the optical reflectance of each sample due to the presence of the metallic particles in the surface of the polyester composites. Fig. 4.4 (c) shows the average emissivity (2-12 µm) of the polyester resin as a function of the V_f of FeCO calculated from the IR reflectance by means of Eq. (3.3) [9,10]. The changes shown ($\Delta\epsilon = 10\%$) are lower than expected for a concentration of 0.5 of metal. This can be attributed to the carbon that coated the iron spheres surface, which increases the IR emission of the filler.
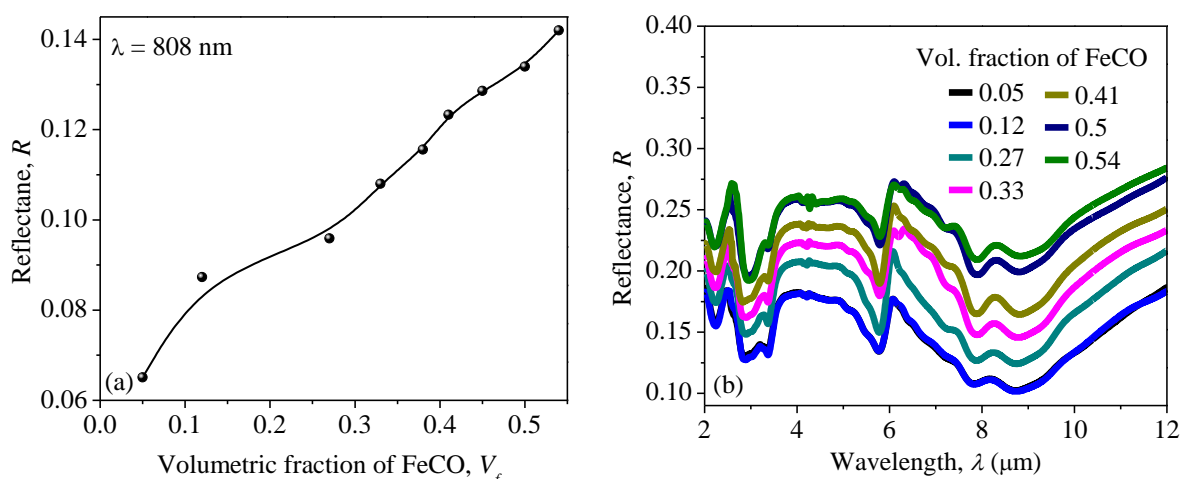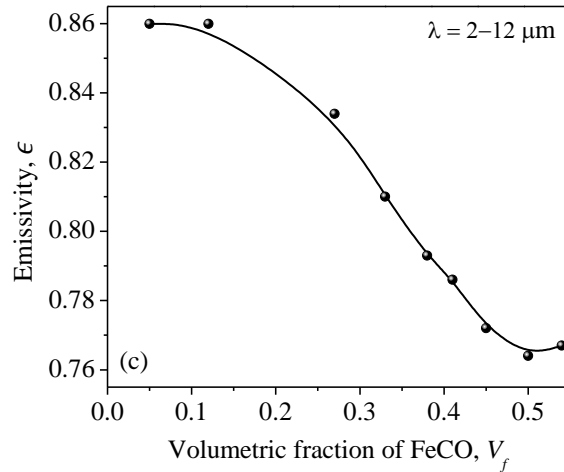
Fig. 4.4. Optical properties of iron carbonyl/polyester composites for several volumetric concentrations. (a) reflectance at 808 nm, (b) spectral IR reflectance and (c) emissivity calculated with IR reflectance by using the Eq. (3.3) in the spctral range of 2-12 µm.

Fig. 4.5 shows the normalized amplitudes of those resins, in which heat transfer satisfies the one-dimensional propagation model of Eq. (4.2). These have been obtained by dividing the amplitude signal for volume fractions of 0.5 and 0.54 by the amplitude of the reference (glassy carbon).

As expected, the normalized amplitude for samples of the highest concentrations is nearly independent of the modulation frequency, therefore, similarly to the analysis of the data performed for the selective coatings deposited on metallic substrates of chapter 3, the average normalized amplitude $|\overline{\Delta W}|_{Norm}$ is given by

$$|\overline{\Delta W}|_{Norm} = \frac{\epsilon_{sample}}{\epsilon_{Ref}} \frac{\left(1 - R_{sample}\right)}{\left(1 - R_{ref}\right)} \frac{\eta_{NR-sample}}{\eta_{NR-Ref}} \frac{\varepsilon_{Ref}}{\varepsilon_{sample}}, \tag{4.2}$$

where ϵ_{sam} (ϵ_{ref}), R_{sam} (R_{ref}), η_{NR-sam} (η_{NR-ref}) and ε_{sample} (ε_{Ref}) are the emissivity, optical reflectance, light-into-heat conversion factors and thermal effusivity of the sample (reference), respectively.
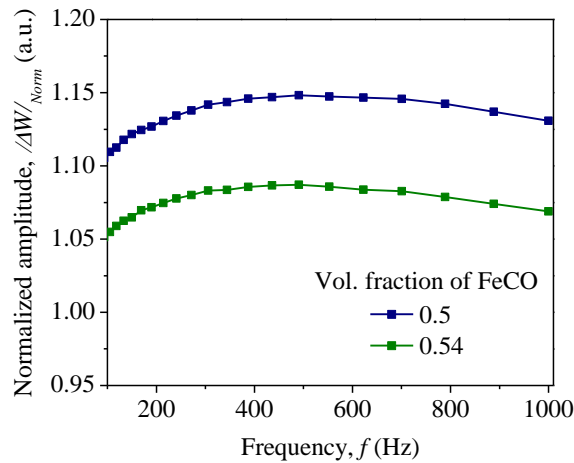
Fig. 4.5. Normalized amplitude of iron carbonyl/polyester composites for volumetric concentrations of 0.5 and 0.54. The glassy carbon signal has been used as reference.

Table. 4.2. PTR Normalized amplitude, optical reflectance at 808 nm, emissivity obtained by FTIR, thermal effusivity and relative optical-to-thermal (non-radiative) energy conversion efficiency, obtained for carbonyl iron/polyester composites for volumetric concentrations of 0.5 and 0.54. As reference, glassy carbon Sigradur-K has been used.

V_f	$|\overline{\Delta W}|_{Norm}$	R (808 nm) (%)	FTIR Emissivity (%)	Effusivity 10^3 ($Ws^{1/2}m^{-2}K^{-1}$)	$\eta_{NR-sam}/\eta_{NR-ref}$
0.5	1.12	13.4	76.4	2.11	0.29 ± 0.06
0.54	1.08	14.2	75.7	2.26	0.30 ± 0.04
Reference	***	15.8	56.0	5.83	***

By using these results, and those shown in Table. 4.1 and Fig. 4.4 (a)-(c), the ratio of light-into-heat conversions $\eta_{NR-sam}/\eta_{NR-ref}$ of sample and reference can be determined. Table 4.2 summarizes the optical and thermal properties of reference material, and polyester resins of volumetric fractions 0.5 and 0.54 of iron carbonyl.

The values of $\eta_{NR-sam}/\eta_{NR-ref}$ obtained are significantly lower than one, which implies that glassy carbon surface has a better efficiency to convert the incident light into-heat than the polymers. Moreover, these results confirm the importance of the optical properties for the correct characterization of materials by using photothermal techniques.

4.3. Infrared scattering effects of nanostructured solar selective coatings

Additional to the effects on heat propagation generated by an inhomogeneous microstructure, such as presented in the last section, in chapter 3 it has been found that thin films can modify the thermal profiles of metallic substrates, mostly for those materials that satisfy the relation $10\mu > 2a$ (3D heat propagation). In this section the nature of these phenomena will be analysed using PTR signals, SEM micrographs and the Kubelka-Munk function for light scattering.

4.3.1. Molybdenum thin film deposited on silicon and copper substrates

In order to establish the role of the thin film structure in the photothermal signals of thick materials, molybdenum 30 nm (Mo) thin films, deposited on silicon (Si) and copper (Cu) via sputtering (see Sec. 3.7) have been studied. Figure 4.6 shows the phase signal recorded for both samples in the modulation frequency (f) range from 3 to 1000 Hz, where the substrates present three-dimensional heat propagation (see chapter 2).

Figure 4.6(a) shows that the Mo thin film does not generate significant changes in phase signals of silicon substrate, compared with those observed for unpolished Cu at $f \geq 30$ Hz [see Fig. 4.6(b)]. Even when both films have been deposited under the same conditions, the substrate plays a fundamental role on the layer characteristics, such as shown in the SEM micrographs of Figure 4.7, performed by means of a Field Emission Scanning Electron Microscope (FESEM JEOL 7600F).
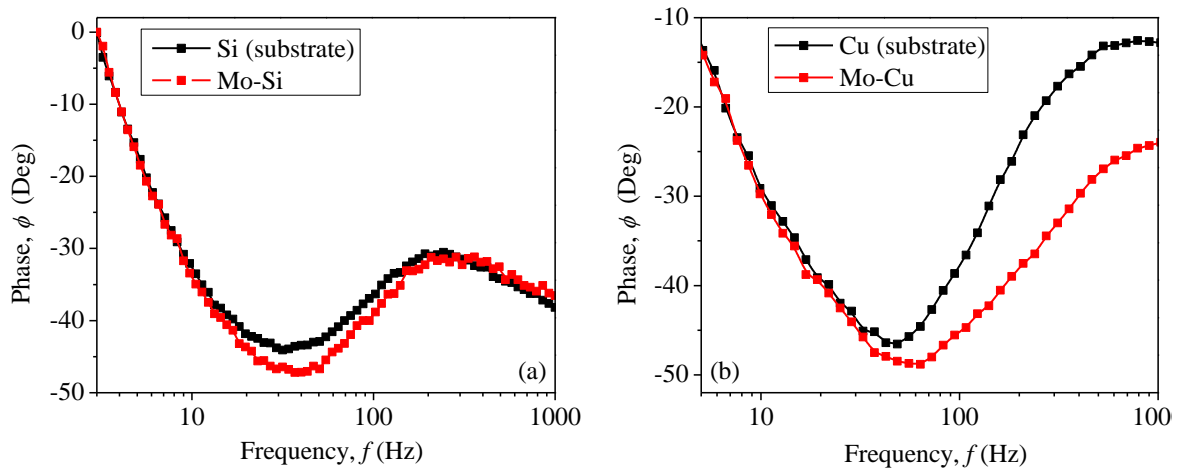
Fig. 4.6. PTR phase signals obtained for (a) Mo-Silicon and (b) Mo-Cu samples (red lines) compared with those for the corresponding substrate (black lines).
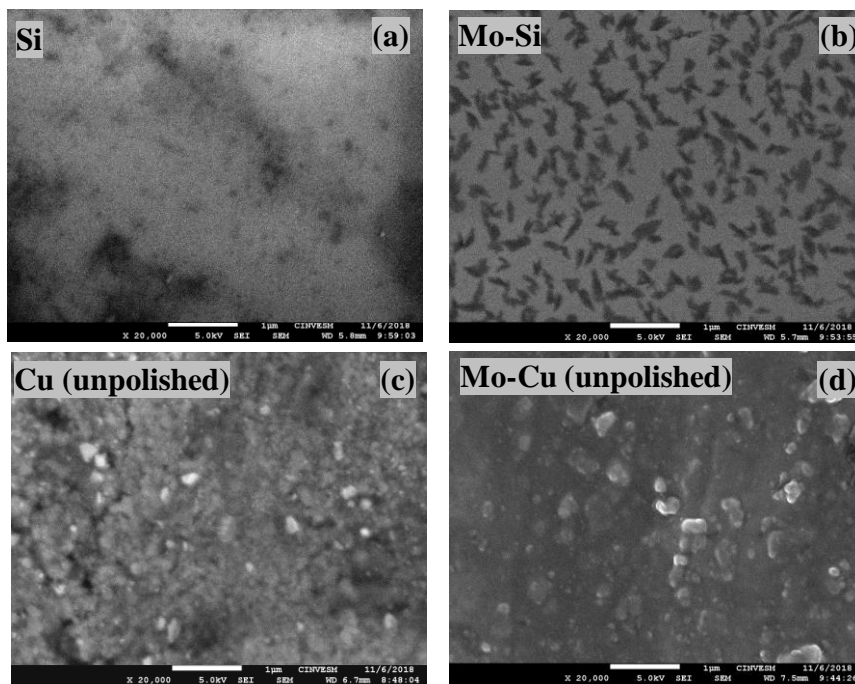
Fig. 4.7. SEM micrographs of (a) silicon (b) Mo-Si, (c) Cu and (d) Mo-Cu samples.

The polished surface of silicon (100) can be observed in the SEM micrograph of Fig. 4.7(a). This image shows a homogeneous surface, with non-observable texture, and dark zones that can be associated with silicon dioxide (SiO_2). This surface allows deposition of Mo, forming uniform grains well distributed on the whole area, such as shown in Fig. 4.7(b). In this last

image the back surface is the silicon substrate, which can be observed because the grown layer is very thin.

In contrast to samples grown on silicon, the copper substrate [Fig. 4.7(c)] shows a inhomogeneous surface due to the presence of oxides, which appears in the image as bright and dark points that generates a remarkable roughness. The same pattern repeats once the Mo layer has been deposited because, as shown in Fig. 4.7(d), this film forms grains of different sizes, which additionally have different optical characteristics due to the presence of oxides (Cu_2O) and metal (Mo) on the surface. According to Fig. 4.7, the differences of the phase signals of substrate and layer+substrate, can be mainly associated to the differences between the structures of both surfaces, which tend to modify the thermal profile of the substrate.

From the thermal point of view, it is not possible that a film of 30 nm of Mo modifies the heat propagation of 350 µm of copper within the range of modulation frequencies studied (see chapter 2), unlike the results obtained with polyester resins in Sec. 4.2 for low concentrations of iron carbonyl. This behavior is a consequence of purely optical effects, related to grain size, surface composition, and velocity of the processes of energy absorption and re-emission (IR).

4.3.2. Kubelka-Munk function for scattered light.

Paul Kubelka and Franz Munk in 1931 [11] proposed a group of semiempirical differential equations to explain the decrease of the light flux due to scattering in optically diffuse and absorber samples such as powders and paper. They suggested that scattering phenomena are a generalization of the optical absorption process given by Beer-Lambert law [12]. Wiszecki and Styles solved these equations in terms of the spectral diffuse reflectance $R_L(\lambda)$ and transmittance $T_L(\lambda)$ as shown in Eq. (4.3) [13]

$$R_d(\lambda) = \frac{1 - R_B[a - b\coth(bSL)]}{a - R_B + b\coth(bSL)}$$

(4.3a)

$$T_d(\lambda) = \frac{b}{a\sinh(bSL) + b\cosh(bSL)},$$

(4.3b)

where R_B is the back-surface reflectance of the sample, $a = \frac{S+\beta}{S}$ relates the scattering coefficient S [m^{-1}] and optical absorption coefficient β [m^{-1}], $b = \sqrt{a^2 + 1}$ and L [m] is the sample thickness.

For opaque samples, $L \gg \beta^{-1}$ (i.e infinite thickness), the back-surface reflectance is zero, then $R_B = 0 = T_d(\lambda)$, therefore Eq. (4.3a) solved for $\frac{\beta}{S}$ factor reduces to:

$$\frac{\beta}{S} = \frac{[1 - R_\infty(\lambda)]^2}{2R_\infty(\lambda)} = f(R_\infty). \tag{4.3c}$$

This last expression, known as the Kubelka-Munk function, is a quantity very useful in optical infrared spectroscopy to quantify the amount of light scattered and determine the real transmittance spectra of composed samples [14,15]. However, due to the difficulty in measuring the spectral diffuse reflectance, experimentally $R_d(\lambda)$ is replaced by the ratio of the total reflectance of sample (e.g. powder dispersed in a KBr or KCl matrix) and a non-absorbing reference (KBr or KCl), i.e. $R_d(\lambda) \rightarrow R_\infty(\lambda) = R_{sample}/R_{ref}$. Therefore, if $R_{sample} = R_{ref}$, then $R_\infty(\lambda) = 1$ and $f(R_\infty) = 0$, which implies that the sample does not produce light scattering.

Both optical and photothermal radiometry spectroscopy are based in the measurement of photons, in the first case those reflected by a surface illuminated with a light source, while in the second one, the photons emitted by a surface when it is heated up with a modulated heat source. In the case of PTR, additional to the optical characteristics, these photons, described by a periodic function, carry information on thermal properties of sample.

Additionally, based on the heat propagation model shown in chapter 2, the phase of the PTR signal is expected to depend only on the heat diffusion properties of the substrate, while the amplitude signal (proportional to the quantity of photons detected) depends on both optical properties of the surface and thermal properties of the substrate. Therefore, in order to establish a connection between PTR, optical spectroscopy and Kubleka-Munk theory, the ratio of the amplitude signal (normalized amplitude) of the sample (layer+ substrate) and reference (substrate) could be used to represent the optical factor R_∞ (R_{sample}/R_{ref}), and quantify the

scattered emitted light as a function of the modulation frequency in the spectral range of 2 to 12 microns (spectral range of IR sensor).
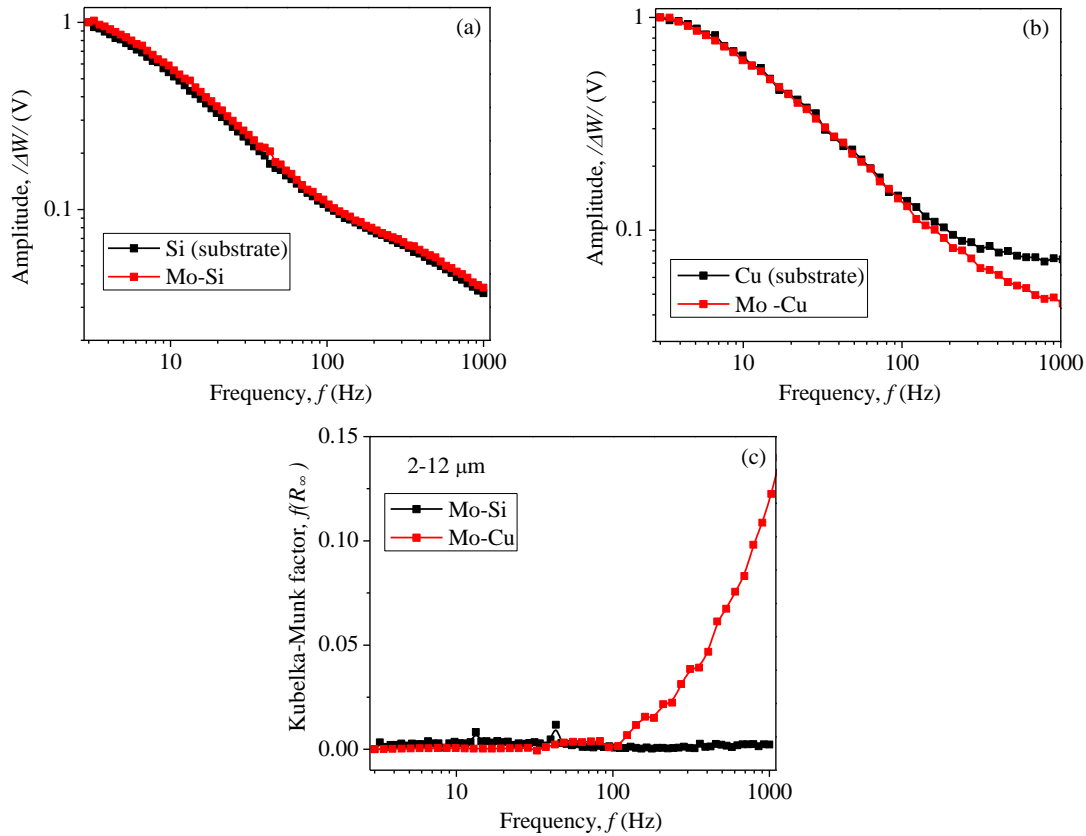
Fig. 4.8. Amplitude signals normalized to one of (a) silicon substrate, Mo-Si sample and (b) copper substrate, Mo-Cu sample. (c) Kubelka-Munk function calculated using Eq. (3.3c).

Figure 4.8 (a) shows the amplitude signals of silicon and Mo+silicon samples, which have been normalized to one, in order to eliminate its differences due to optical properties of absorption (reflectance and light-into-heat convertion efficieny) and emission (emissivity). In this case, as was also shown by phase signal of Si and Mo+silicon [see Fig 4.6(a)], both present identical behavior, while for copper and Mo+copper samples [Fig. 4.8(b)], the amplitudes show a difference for frequencies above 100 Hz, which can be associated with light scattering processes. This implies that the phase of the signal is more sensitive to inhomogeneous surfaces than the amplitude, because the thermal profile of the Mo+copper sample differs from the reference from 30 Hz [see Fig 4.6(b)]. The scattering functions shown in Fig. 4.8(c) for both samples have been calculated by means of Eq. (4.3c), where the factor R_∞ has been obtained dividing the amplitude signal of samples with that of its corresponding substrate. In this case,

since Si and Mo+silicon amplitude signals are the same, $R_\infty \sim 1$, therefore $f(R_\infty) \sim 0$ in the entire frequency range and spectrum evaluated.

The difference in the response of photothermal signals (amplitude and phase) to scattering phenomena can be understood from Fig. 4.9. For one-dimensional heat propagation, infrared radiation is emitted mainly normally to the surface (blue beam) following the optical path δ_1, while in the three-dimensional case, this emission presents an aperture (green beam), which is corrected by the parabolic mirrors before being sent to the IR sensor (optical path δ_2). In the scattering process, with increasing the modulation frequency the aperture of light emitted increases, as well as its optical path δ_3 (orange beam), which generates a negative delay in the phase signal.
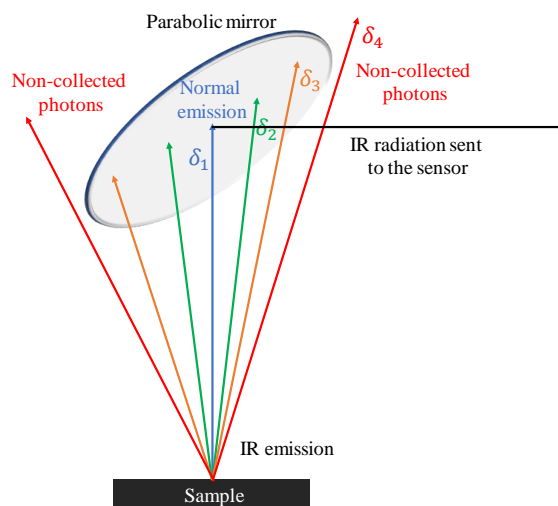
Fig. 3.9. Scheme of the optical path followed by infrared radiation emitted by a surface for (blue) null (green) low, (orange) medium and (red) high scattering processes induced by a modulated heat source.

Although the optical path followed by emitted light increases for three cases considered ($\delta_1 < \delta_2 < \delta_3$), the quantity of photos detected by sensor is the same, therefore the amplitude does not change. This implies that scattering phenomena only affects this signal at enough high modulation frequencies, when the quantity of IR photons collected by the mirrors decreases (red beam), which generates a decrease in the amplitude [see Fig 4.8(b)]. In the case of selective coatings presented in chapter 3 for aluminum and copper substrates (see Fig. 3.4), for the modulation frequencies at which heat transfer satisfies the one-dimensional heat propagation

condition, the emitted light is "more focused", which allowed the optical characterization of these samples by using the amplitude of the photothermal signal, even when the phase delay was not zero.

4.3.3. Kubelka-Munk function of solar selective coatings.

In this section, solar selective coatings similar to those studied in chapter 3 will be analyzed by using the Kubelka-Munk function. Figure 4.10 shows the SEM micrographs and phase signal of the absorber nickel oxide (BN) coating deposited on nickel (Ni-Cu) with two different thicknesses (0.2 and 2 µm), in order to observe the dependence of scattering phenomena on the grain size of the deposited layer.

In Figure 4.10(a) the surface structure of unpolished copper substrate is strongly influence by oxides. In the case of BN (nickel oxide), the thinner film [Fig. 4.10(b)] generates well-interconnected uniform flakes around 150 nm in size, while the other film presents a completely different structure with crystals of around 600 nm [Fig. 4.10(c)].

The difference in the behavior of heat transfer between both samples can be observed in the phase signal of Fig. 4.10(d), where the BN(2 µm)-Ni-Cu shows an identical thermal profile compared with the copper substrate, unlike the BN(0.2 µm)-Ni-Cu. The same pattern is observed for other selective coatings of cobalt oxide as shown in Fig. 4.11. In this case, the metallic nickel Ni(1 µm)-Cu [Fig. 4.11 (a)] shows a uniform layer with grains of 100 nm, as can be observed in Fig 4.11 (b), the cobalt oxide (0.2 µm) deposited on Ni-Cu. Based on these results it is possible to establish a relation between grain size and scattering process generated, which tends to disappear as the grains deposited are bigger.
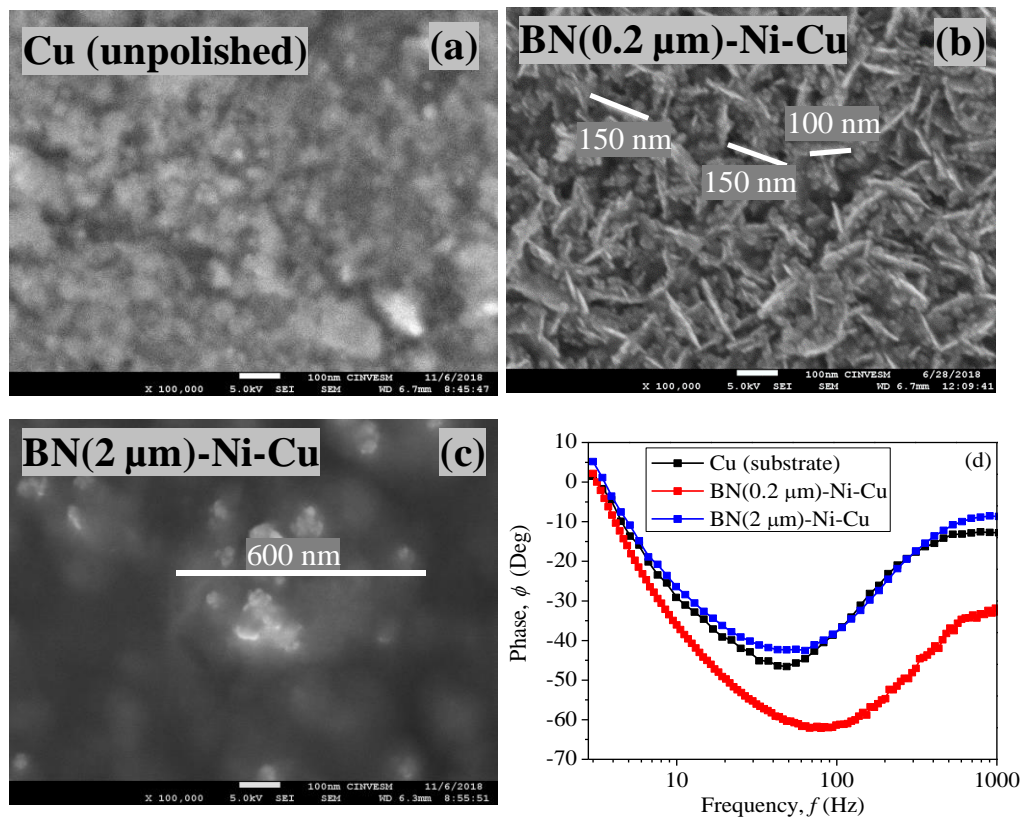
Fig. 4.10. SEM micrographs of (a) copper and BN-Ni-Cu samples with thickness of (b) BN 0.2 microns and (c) BN 2.0 microns. (d) PTR phase signal of copper substrate and BN-Ni-Cu samples.

Additionally, even when both Ni and Co surfaces show similar structure and grain size, the latter shows a larger scattering effect. This could be associated with the presence of additional phases in the structure of the cobalt oxide (CO), which can be observed in the SEM micrograph as brighter zones. In the next section, it will be shown that the presence of dielectric and metallic materials on a surface generates stronger scattering effects than those produced by different grain sizes.
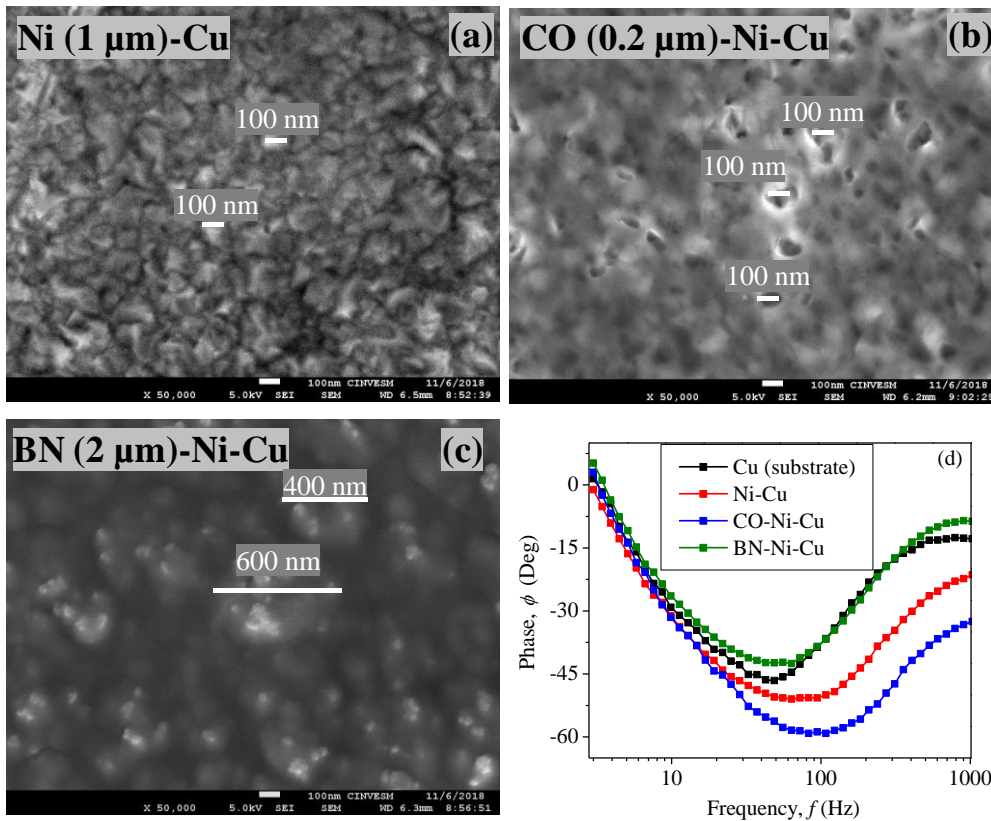
Fig. 4.11. SEM micrographs of (a) Ni-Cu (b) CO-Ni-Cu and (c) BN-Ni-Cu samples. (d) phase signals of samples and copper substrate.
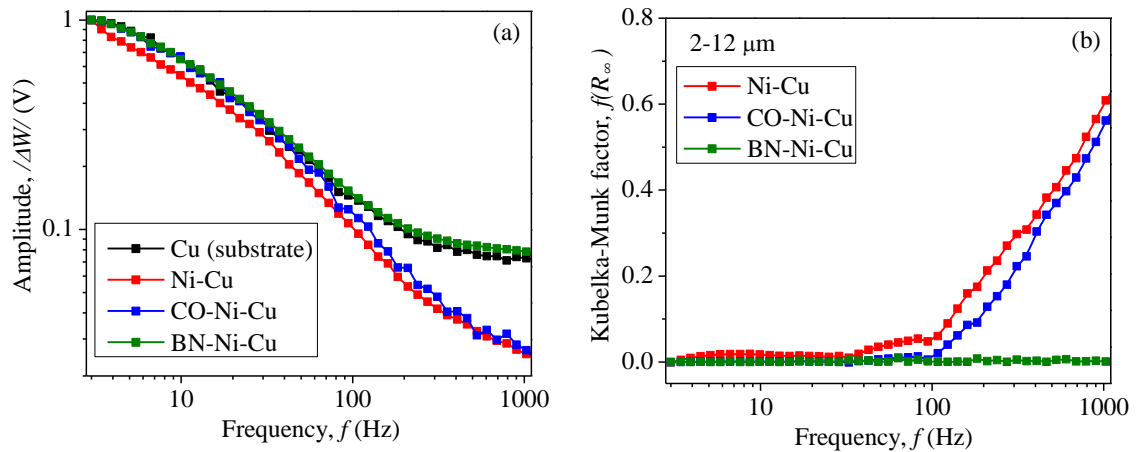
Fig. 4.12. (a) Amplitude signals normalized to that of the Cu substrate, Ni-Cu, CO-Ni-Cu and BN-Ni-Cu samples. (b) Kubelka-Munk function calculated by using Eq. (4.3c).

Figure 4.12 shows the amplitude signal normalized to one, and the Kubelka-Munk factor obtained by using Eq. (4.3c). As expected, the BN of 2 µm does not produces scattering effects, while the metallic nickel (Ni) and cobalt oxide produces a higher one than the obtained with

molybdenum [Fig. 4.8 (c)]. Moreover, although the phase shows that the cobalt oxide layer induced a larger light scattering than nickel, both scattering factors are similar, which confirms that phase signal is more sensitive to inhomogeneities of surfaces than the amplitude.

4.4. PTR signals of vanadium dioxide (VO$_2$) thin films across its metal-to-insulator transition (MIT)

The work developed by Morin some decades ago [16] on the metallic behavior of some oxides of titanium and vanadium under temperature changes, opened investigation fields focused on the understanding of the properties of these thermochromic materials. Vanadium dioxide (VO$_2$) has received special attention due its reversible metal-to-insulator transition (MIT) at a relative low transition temperature ($T_C = 67$ºC) [17], in which it presents a first order reversible phase change from monoclinic (M1) to tetragonal (R) structure. This structural transition [18,19] modifies the insulator behavior of VO$_2$ at low temperatures ($T \ll T_C$), to a metallic one at high temperatures [20] ($T \gg T_C$) and this is accompanied of huge changes in the optical, [21,22] electrical [23,24] and thermal [25,26] properties.

Studies of the thermophysical properties of VO$_2$ across its MIT have been performed using thermoreflectance and PTR by Oh *et. al.* and Hamaoui *et. al.,* respectively [27,28]. In both cases, modulation frequencies up to 10 THz (10^{12} Hz) were used, which allowed the analysis of the VO$_2$ thin films (100-300 nm) with the conventional heat propagation models for multilayered systems. Therefore, in the low modulation frequencies range used in this work (<1000 Hz), all changes in the photothermal signals will be analyzed under the assumption that the optical phenomena are the most dominant.

Typically, the VO$_2$ optical properties have been characterized by using reflectance spectroscopy techniques [29,30], such as those described in Sec. 3.4 of chapter 3. In the dielectric phase the VO$_2$ thin films exhibit high absorption/emittance in the IR region with emissivity ~70% [31], while in the metallic state the films are highly reflective (IR-opaque), which decreases the emissivity below 15% [32]. In chapter 5 all these characteristics will be analyzed in more detail by using ellipsometry.

4.4.1. Deposition process and structural characteristics of VO₂ thin films

The VO$_2$ thin films have been deposited via pulsed laser deposition (PLD) technique, which uses a pulsed high-power laser beam to evaporate material from a solid target. A KrF pulsed excimer laser (λ = 248 nm), pulsed width of 25 ns, and repetition rate of 25 Hz has been employed to grow a VO$_2$ film of 120 nm (200 nm) on r-plane (c-plane) sapphire of thickness 0.5 mm at the temperature of 600ºC, within an ultra-high vacuum chamber with oxygen pressure of 2.2 Pa [33]. The thickness of each layer has been measured by profilometry (KLA-Tencor AlphaStep D-120).

The crystalline structure of samples was analyzed by X-Ray Diffraction (XRD), whose room-temperature pattern is shown in Fig. 4.11(a-b). These patterns were determined by a diffractometer D-8 advance operating with a Bragg-Brentano geometry and CuK$_{\alpha1}$ radiation. According to the International Centre for Diffraction Data (Card 04-003-2035), the XRD peaks correspond to the monoclinic phase of VO$_2$ and are consistent with those found for a VO$_2$ thin film deposited on r-plane and c-plane sapphire [34].

The Raman spectra measured by means of a Confocal Raman Witec Alpha300 spectrometer are shown in Fig. 4.12(c) for three relevant different temperatures across its MIT. In the insulating state ($T \ll T_C$), the spectrum exhibits nine characteristic peaks (194, 225, 255, 309, 343, 390, 440, 500 and 620 cm^{-1}) associated with the different vibration modes of the VO$_2$ monoclinic structure, as was previously identified. [35,36,37] This dielectric phase is mainly characterized by the V-V mode at $\sim$620 cm^{-1} and the V-O modes at 194 cm^{-1} and 225 cm^{-1} [38]. As the VO$_2$ sample temperature increases ($T{\sim}T_C$), the intensity of the Raman peaks decreases as a result of the appearance of the metallic domains due to the MIT. Finally, at higher temperatures ($T \gg T_C$) for which the VO$_2$ film reaches its metallic phase (tetragonal structure), the Raman spectrum becomes featureless, as expected for the Raman spectra of metals.
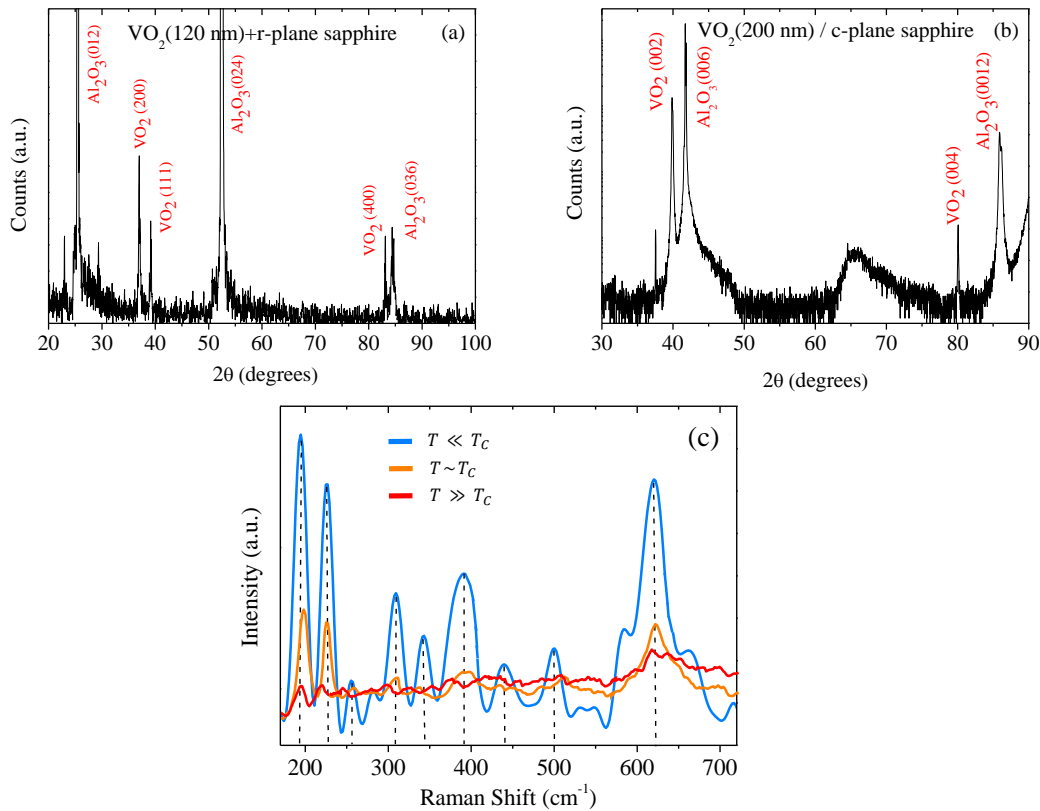
Fig. 4.12. Room temperature XRD pattern of VO$_2$ film deposited on (a) r-plane and (b) c-plane sapphire substrate. (c) Raman spectra for the insulator (blue), insulator-metal (orange), and metallic (red) phases of VO$_2$ thin film grown r-plane sapphire.

In order to analyze the differences on the VO$_2$ film microstructures induced by the substrate, Figure 4.13 show the SEM and AFM images of the surface morphology of both samples which have been respectively performed by means of a Field Emission Scanning Electron Microscope (FESEM JEOL 7600F), and an Atomic Force Microscope integrated with a Confocal Raman Witec Alpha300 spectrometer. Figures 4.13(a)-(b) show that the grains formed on the r-plane sapphire substrate are well interconnected in a columnar type growth, exhibiting mainly elongated shapes with a grain height of 28 nm. In contrast, the c-plane sapphire substrate induces single spherical-like crystals (grain height 40 nm) with a remarkable separation between them. These differences in the structure of the surface of both samples have been previously reported and are mainly attributed to the plane of growth orientation, which strongly influences the density of defects, grain boundaries, nucleation barrier and the strain, which are fundamentals factors affecting in the macroscopy properties of VO$_2$ across its MIT [31]. Surface roughness of VO$_2$+r-plane sapphire (13 nm) and VO$_2$+c-plane sapphire (20 nm), was obtained

from the arithmetical mean height (Sa: 5 nm, 19 nm), the mean root square height (Sq: 7 nm, 18 nm) and the maximum height (Sz: 28 nm, 40 nm), respectively.

VO_2+r-plane sapphire

VO_2+c-plane sapphire
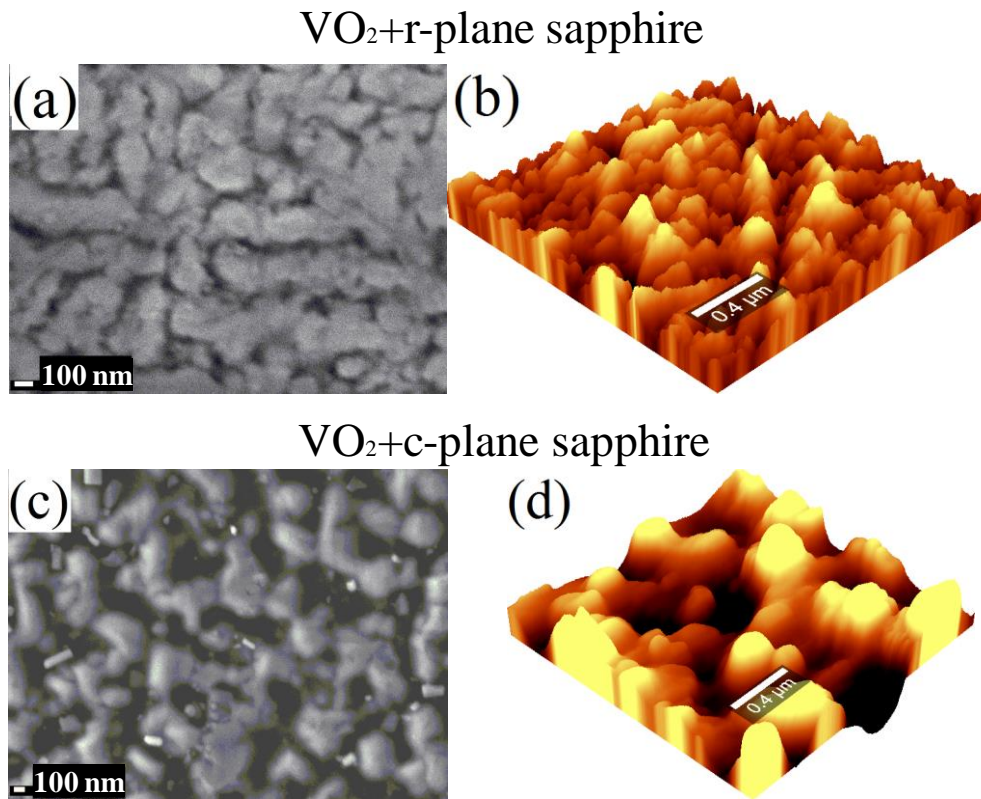
Fig. 4.13. SEM micrograph and three-dimensional AFM images of (a)-(b) VO_2+r-plane sapphire and (c)-(d) VO_2+c-plane sapphire.

Films thicknesses have been determined using a Dektak Profilometer of accuracy ±2 nm, however the real error values in the thickness are related with the deposition process. The inhomogeneity in the surface is intrinsically linked to the PLD process such that on a 1×1 cm^2 sample area, the accuracy is ±15% of the maximum of the thickness measured at the center. To overcome this problem, a PLD process has been developed based on a "moving" plasma plume in the referential – (coordinate systems) of the substrate, the plume is moving on a 1×1 cm^2 surface without fluence (Energy/surface) variation. This methodology reduces the variation in thickness to around 8%.

4.4.2. Phase signals of VO₂+Sapphire samples

Figure 4.14 shows the phase signal of (a) VO₂+r-plane sapphire and (b) VO₂+c-plane sapphire samples, measured at the insulating (black lines) and metallic (red lines) states of the VO₂ thin film, in the modulation frequency range of 1 to 100 Hz. These signals have been obtained by using the same PTR setup as presented in Fig. 3.2, along with a Peltier cell controlled with a power supply to heat the sample. It is important to remark that the electrical response of the IR-sensor depends only on the AC component of the sample temperature [39], which is induced by the modulated heat source.
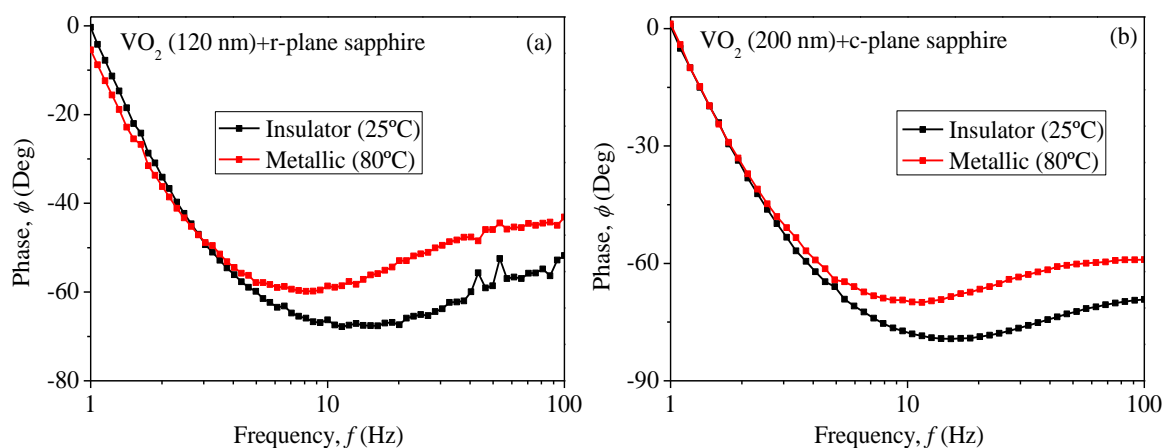
Fig. 4.14. PTR phase signals of VO₂ thin film deposited on (a) r-plane and (b) c-plane sapphire substrate, in the insulator (black lines) and metallic states (red lines).

The metallic structure (rutile-R) of both VO₂ samples induced by the heating, modify the VO₂(M1)+sapphire phase signal obtained at room temperature, similar to the solar selective coating effects on the phase signal of aluminum and copper substrates shown in chapter 3 (see Fig. 3.3) and Sec. 4.3. According to analysis previously performed on scattering effects, this means that metallic surfaces scatter less IR light that dielectric ones, as has been observed for nickel (Ni) and cobalt oxide (CO) coatings of Fig. 4.11.

In order to analyze the dependence of photothermal signals with the structural evolution of VO₂, the PTR measurements have been carried out BY fixing the modulation frequency taking as parameter the sample temperature across the insulator-to-metal (heating) and metal-to-insulator (cooling) transitions. Figure 4.15 shows the phase signal of both VO₂ samples at three different modulation frequencies.
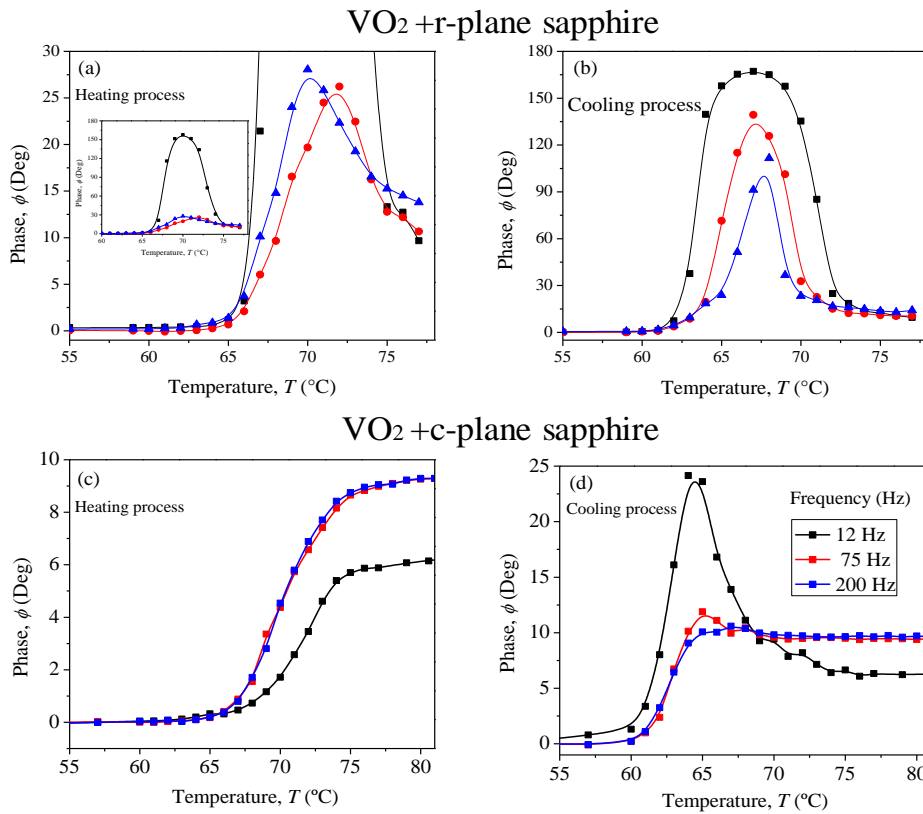
Fig. 4.15. PTR signals of VO$_2$ thin film deposited on (a-b) r-plane and (c-d) c-plane sapphire substrate during the heating and cooling processes at several modulation frequencies.

In the insulator ($T \ll T_C$) and metallic ($T \gg T_C$) states, phase signals show near constant values, which represents the stability of the monoclinic and rutile structures at the beginning and end of the transition. At the intermediate state ($T \sim T_C$), the signals show an increase for $T > 65°$C ($T < 72°$C) in the heating (cooling) process, as a consequence of metallic (insulator) domains that emerge in the surface [40,41,42], whose maximum phase values are remarkable higher for VO$_2$ thin film deposited on r-sapphire in all cases. In chapter 5, we will show that this is related with the optical properties of VO$_2$ at the point where the volumetric fraction of metal in the surface is around 50%, i.e. when the surface presents the highest structural inhomogeneity. Additionally, the phase change shows a strong dependence on modulation frequency, similar to the results reported by Pekker *et.al.* for a VO$_2$ thin film analyzed by means of PTR [43]. Based on the analysis of the solar selective coatings in Sec. 4.3, these last differences are a consequence of the heat propagation in the sapphire substrate ($\alpha = 10.26$ mm^{2}s^{-1}), in which

the heat flux tends to become one-dimensional as the modulation frequency increases, decreasing the scattering effects (see Fig 3.9).

4.4.3. Amplitude signals and Kubelka-Munk scattering factor of VO₂+sapphire samples

The amplitude signals of VO₂+sapphire samples across the MIT in the heating and cooling processes can be seen in Figures 4.16(a) and 4.16(b). Theses ones show linear behavior in the insulator $T < 65$ºC and metallic $T > 75$ºC states, because the increase (decrease) of the power emitted by the sample, when the DC temperature increases (decreases), such as predicted by

$$\Delta W = 4\epsilon\sigma_B T^3 \theta, \tag{4.4}$$

where ϵ is the emissivity of the surface, σ_B [5.67×10^{-8} Wm^{-2}K^{-4}] is the Stefan-Boltzmann constant, T [K] is the DC temperature of the sample measure by a thermocouple in contact with the surface, and θ [K] is the modulated temperature which dependence on the absorption, light into heat conversion efficiency of the VO₂, and thermal properties of the sapphire substrate (see chapter 2) [44], which are expecting to remain constants across the MIT.
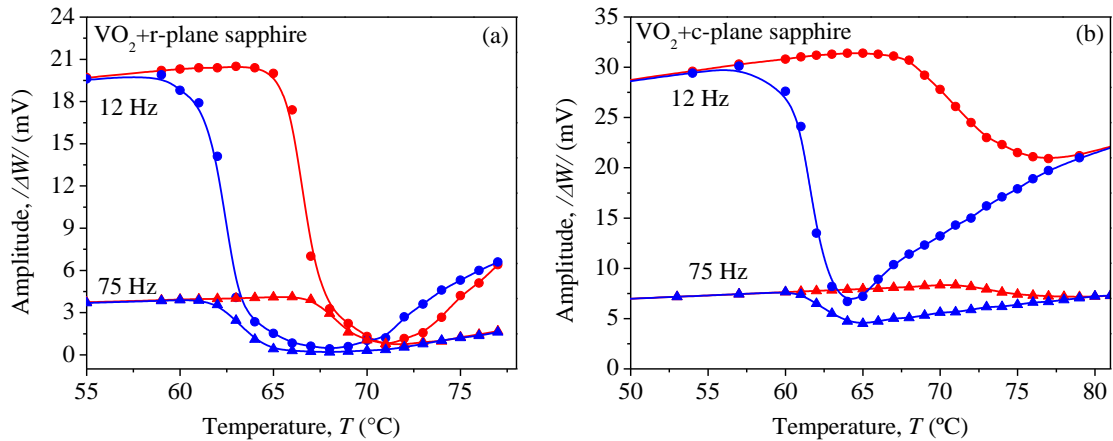
Fig. 4.16. PTR amplitude of VO₂ thin film deposited on (a) r-plane and (b) c-plane sapphire substrate, during the heating (red lines) and cooling (blue lines) processes at (circles) 12 Hz and (triangles) 75 Hz.

At the intermediate state, amplitude signals decrease during the heating and increase during the cooling process, following a different path to form the characteristic hysteresis loop of VO₂. These changes are related with the emissivity of the surface across the MIT and the scattering

effects (see Fig.4.15), whose minimum values match with the maximum of phase signals. The emissivity changes of both samples are shown in Fig. 4.17, which has been measured by using the thermal wave resonant cavity following the methodology described in Ref [31].
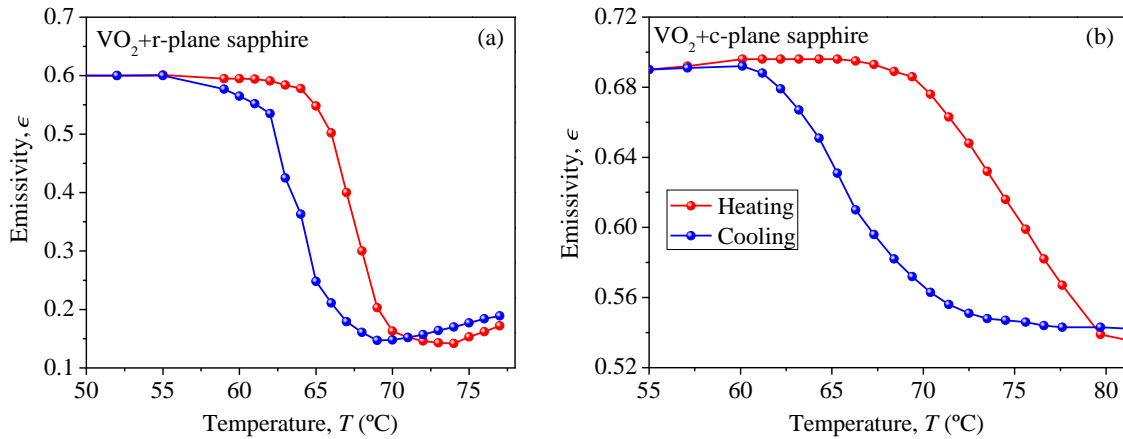
Fig. 4.17. Infrared emissivity of VO_2 thin film deposited on (a) r-plane and (b) c-plane sapphire substrate by using the thermal wave resonant cavity (TWRC) described in Ref [31].

In the insulator state, the emissivity of VO_2+r-sapphire is lower than in VO_2+c-sapphire, due to the lower thickness of VO_2 film, but it shows better metallic properties at high temperature with an emissivity around 15%, compared with 54% of the thicker one. This is because the structural morphology of VO_2 grown in r-plane sapphire shows well connected grains (see Fig. 4.12) that promotes the percolation process, strongly affecting the optical properties of the surface [40,41], inducing infrared light scattering phenomena, which can be observed during the metal insulator transition, because of its effects on the phase signals of VO_2+r-sapphire sample.

Figure 4.18 shows the normalized amplitude signals for VO_2+sapphire samples at modulation frequencies of 12 Hz and 75 Hz during the heating and cooling processes. These has been obtained taking into account that factors such as light absorption $(1 - R)$ and light-into-heat conversion efficiency (η_{NR}) of VO_2 thin film at 808 nm (laser's wavelength), which remain constant through the MIT (see chapter 5), the effect of DC temperature in the PTR signals, and the changes in the emissivity values (see Fig. 4.17).
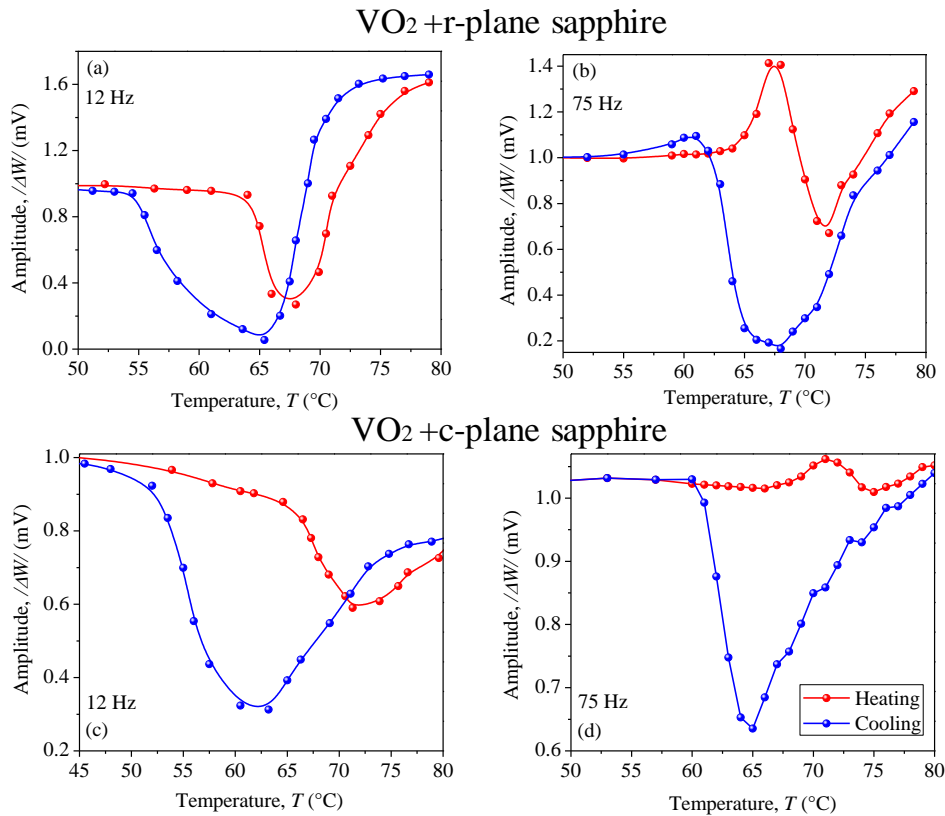
Fig. 4.18. PTR amplitude signals normalized to one of (a-b) VO$_2$+r-plane and (c-d) VO$_2$+c-plane sapphire substrates at 12 Hz and 75 Hz during heating and cooling processes.

These amplitudes show near constant values in the insulating and metallic states, associated to stability of the structure and therefore of VO$_2$ optical properties, such as shown in Fig. 4.14. In the intermediate state, at 12 Hz [Fig. 4.18 (a-c)] both signals decrease, when the insulating and metallic domains coexist. The minima of the amplitude agree with those found during the heating and cooling processes for the phase. Moreover, at 75 Hz during the heating processes, both samples show a maximum in the amplitude, which could be related with scattering phenomena of infrared radiation, already reported for VO$_2$ thin films deposited on sapphire. This produces a directionally temperature driven emission of light by the VO$_2$-sapphire interface [45,46]. The dependence of this phenomena with the modulation frequency still remains unexplored.

In order to observe the dependence of the scattering factor in Eq. (3.3c) with the volumetric fraction of metal (V_f) in the VO$_2$ surface (see chapter 5), The scattering factor is calculated by means of the amplitudes of the PTR signals presented in Fig 4.18.

Figure 4.19 shows that the Kubelka-Munk function tends to zero in the insulating and metallic states. This could be expected according to photothermal signals of Figures 4.15 and 4.18. In the heating process this factor shows its maximum around a volume fraction (V_f) of 0.65 for VO_2 deposited on r-sapphire [Fig. 4.19(a)] while for the one deposited on c-sapphire this happens at V_f =0.5 [Fig. 4.19(c)]. This difference is a consequence of the optical properties of the metallic domains in the percolation process, which in the first case, induces stronger scattering effects, as mentioned previously based on SEM micrographs shown in Fig. 4.13.
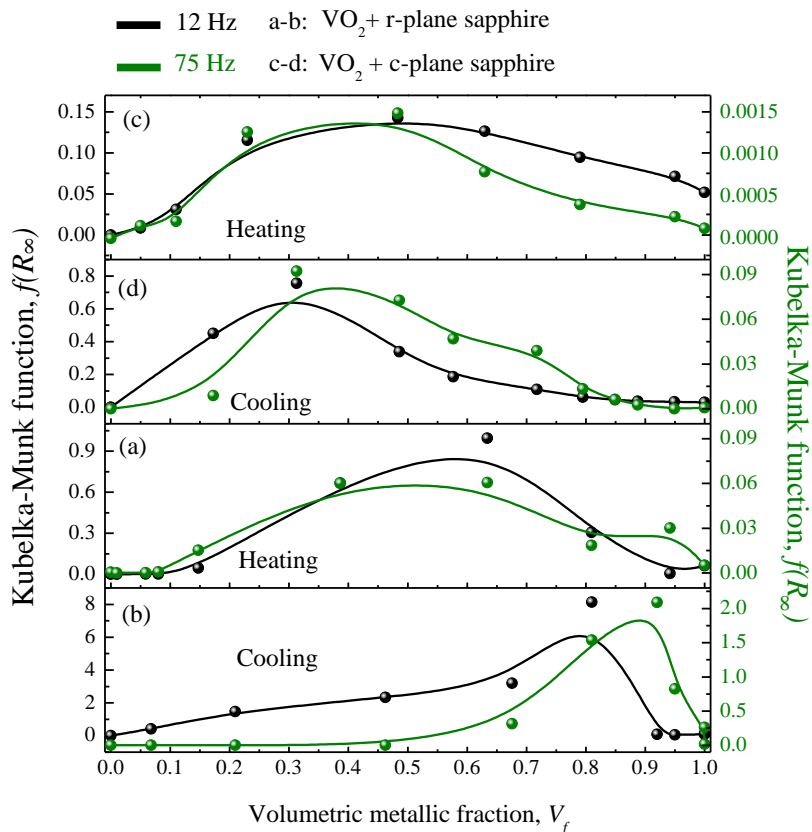
Fig. 4.19. Kubelka-Munk factor calculated by using amplitude signals and Eq. (4.3c) for VO_2 thin films deposited on (a-b) r-plane and (c-d) c-plane sapphire, as a function of the volumetric metallic fraction in the VO_2 (see chapter 5).

The scattering factors calculated are up to 10 times higher at 12 Hz than 75 Hz, and even much higher for the cooling than for the heating processes. This last observation can be associated to evolution of metallic domains during the transition, which reaches its final metallic properties

only at high temperature. Therefore, at the beginning of the cooling process as shown in Fig 4.19(d), the insulating domains that are appearing induce remarkable differences in the optical properties, increasing the scattering factor up to the highest values registered in this work, even when the volumetric fraction of metal is higher than 0.8. This implies that the optical properties of the grains that coexist on the surface induce a stronger influence than the volumetric concentration on the global optical properties of the material.

4.5. Conclusions

Photothermal radiometry has been used to analyze the thermal profiles of materials with inhomogeneous internal structures and surfaces. Polyester resin samples filled with iron carbonyl (FeCo), showed that photothermal signals satisfy the one-dimensional heat propagation model only at highest volumetric concentration of FeCo, just when the internal structure of resin is sufficiently modified by iron carbonyl, to allow a frontal propagation of thermal waves.

Moreover, solar selective coatings deposited on different substrates showed that grain size (film thickness) and morphology of the surface induce a strong dependence on the photothermal signals. These process are affected by light scattering effects, which can be studied by means of the Kubelka-Munk approach.

Finally, vanadium dioxide thin films deposited on sapphire substrates showed that composition of surfaces (dielectric and/or metallic) also plays a fundamental role in scattering effects.

References

[1] Kim, H. S., Kim, J. H., Kim, W. Y., Lee, H. S., Kim, S. Y., & Khil, M. S. (2017). Volume control of expanded graphite based on inductively coupled plasma and enhanced thermal conductivity of epoxy composite by formation of the filler network. *Carbon*, *119*, 40-46.

[2] Yu, A., Ramesh, P., Itkis, M. E., Bekyarova, E., & Haddon, R. C. (2007). Graphite nanoplatelet− epoxy composite thermal interface materials. *The Journal of Physical Chemistry C*, *111*(21), 7565-7569.

[3] Shenogina, N., Shenogin, S., Xue, L., & Keblinski, P. (2005). On the lack of thermal percolation in carbon nanotube composites. *Applied Physics Letters*, *87*(13), 133106.

[4] Pech-May, N. W., Vales-Pinzón, C., Vega-Flick, A., Cifuentes, Á., Oleaga, A., Salazar, A., & Alvarado-Gil, J. J. (2016). Study of the thermal properties of polyester composites loaded with oriented carbon nanofibers using the front-face flash method. *Polymer Testing*, *50*, 255-261.

[5] Pech-May, N. W., Cifuentes, Á., Mendioroz, A., Oleaga, A., & Salazar, A. (2015). Simultaneous measurement of thermal diffusivity and effusivity of solids using the flash technique in the front-face configuration. *Measurement Science and Technology*, *26*(8), 085017.

[6] Forero-Sandoval, I. Y., Cervantez-Alvarez, F., Ramírez-Rincón, J. A., Pech-May, N. W., Ordonez-Miranda J., & Alvarado-Gil, J. J., Thermal percolation in random microparticles composites, *under review*.

[7] HTW Germany, Thermophysical properties of Glassy Carbon - Sigradur K. http://www.htw-germany.com/technology.php5?lang=en&nav0=2&nav1=16. Accessed 15 October 2018.

[8] Diaz-Bleis, D., Vales-Pinzón, C., Freile-Pelegrín, Y., & Alvarado-Gil, J. J. (2014). Thermal characterization of magnetically aligned carbonyl iron/agar composites. *Carbohydrate polymers*, *99*, 84-90.

[9] Ienei, E., Milea, A. C., & Duta, A. (2014). Influence of spray pyrolysis deposition parameters on the optical properties of porous alumina films. *Energy Procedia*, *48*, 97-104.

[10] Lizama-Tzec, F. I., Macías, J. D., Estrella-Gutiérrez, M. A., Cahue-López, A. C., Arés, O., De Coss, R., & Oskam, G. (2015). Electrodeposition and characterization of nanostructured black nickel selective absorber coatings for solar–thermal energy conversion. *Journal of Materials Science: Materials in Electronics*, *26*(8), 5553-5561.

[11] Kubelka, P., & Munk, F. (1931). An article on optics of paint layers. *Z. Tech. Phys*, *12*(593-601).

[12] Barbarić-Mikočević, V. D. M. Ž., & Itrić, K. (2011). Kubelka-Munk theory in describing optical properties of paper (I). *Technical Gazette*, *18*(1), 117-124.

[13] Wyszecki, G, Stiles,W, S. Color Science, 2nd edition, J. Wiley & Sons, NewYork, 2000.

[14] Saunderson, J. L. (1942). Calculation of the color of pigmented plastics. *JOSA*, *32*(12), 727-736.

[15] Shimadzu excellence in science, Diffuse reflection method. https://www.shimadzu.com/an/ftir/support/ftirtalk/talk1/intro.html Accessed 10 November 2018.

[16] Morin, F. J. (1959). Oxides which show a metal-to-insulator transition at the Neel temperature. Physical Review Letters, 3(1), 34.

[17] Imada, M., Fujimori, A., & Tokura, Y. (1998). Metal-insulator transitions. *Reviews of Modern Physics*, *70*(4), 1039.

[18] Jones, A. C., Berweger, S., Wei, J., Cobden, D., & Raschke, M. B. (2010). Nano-optical investigations of the metal− insulator phase behavior of individual VO_2 microcrystals. *Nano letters*, *10*(5), 1574-1581.

[19] Atkin, J. M., Berweger, S., Chavez, E. K., Raschke, M. B., Cao, J., Fan, W., & Wu, J. (2012). Strain and temperature dependence of the insulating phases of VO_2 near the metal-insulator transition. *Physical Review B*, *85*(2), 020101.

[20] Yang, M., Yang, Y., Hong, B., Wang, L., Hu, K., Dong, Y., & Song, L. (2016). Suppression of structural phase transition in VO 2 by epitaxial strain in vicinity of metal-insulator transition. *Scientific Reports*, *6*, 23119.

[21] Verleur, H. W., Barker Jr, A. S., & Berglund, C. N. (1968). Optical properties of VO_2 between 0.25 and 5 eV. *Physical Review*, *172*(3), 788.

[22] Kumar, S., Strachan, J. P., Kilcoyne, A. D., Tyliszczak, T., Pickett, M. D., Santori, C., & Williams, R. S. (2016). The phase transition in VO_2 probed using x-ray, visible and infrared radiations. *Applied Physics Letters*, *108*(7), 073102.

[23] Stefanovich, G., Pergament, A., & Stefanovich, D. (2000). Electrical switching and Mott transition in VO_2. *Journal of Physics: Condensed Matter*, *12*(41), 8837.

[24] Kucharczyk, D., & Niklewski, T. (1979). Accurate X-ray determination of the lattice parameters and the thermal expansion coefficients of VO_2 near the transition temperature. *Journal of Applied Crystallography*, *12*(4), 370-373.

[25] Agarwal, R. K., Prasad, S., & Gahlot, N. (2004). Synthesis, spectral and thermal properties of some penta-coordinated complexes of oxovanadium (IV) derived from thiosemicarbazones of 4-aminoantipyrine. *Turkish Journal of Chemistry*, *28*(6), 691-702.

[26] Xie, R., Bui, C. T., Varghese, B., Zhang, Q., Sow, C. H., Li, B., & Thong, J. T. (2011). An Electrically Tuned Solid-State Thermal Memory Based on Metal–Insulator Transition of Single-Crystalline VO_2 Nanobeams. *Advanced Functional Materials*, *21*(9), 1602-1607.

[27] Oh, D. W., Ko, C., Ramanathan, S., & Cahill, D. G. (2010). Thermal conductivity and dynamic heat capacity across the metal-insulator transition in thin film VO_2. Applied Physics Letters, 96(15), 151906.

[28] Hamaoui, G., Horny, N., Gomez-Heredia, C. L., Ramirez-Rincon, J. A., Ordonez-Miranda, J., Champeaux, C., Dumas-Bouchiat, F., Alvarado-Gil, J. J., Ezzahri, Y., Joulain, K., Chirtoc, M., Thermophysical characterisation of VO_2 thin films hysteresis and its application in thermal rectification, *Under review.*

[29] Crunteanu, A., Cornette, J., Colas, M., Orlianges, J. C., Bessaudou, A., & Cosset, F. (2014). Electric field-assisted metal insulator transition in vanadium dioxide (VO_2) thin films: optical switching behavior and anomalous far-infrared emissivity variation. Proceedings SPIE 9364, Oxide-based Materials and Devices VI , SPIE, 2015, Proc. SPIE 9364, Oxide-based Materials and Devices VI, 9364, pp.93640J1-J11.

[30] Choi, H. S., Ahn, J. S., Jung, J. H., Noh, T. W., & Kim, D. H. (1996). Mid-infrared properties of a VO_2 film near the metal-insulator transition. *Physical Review B*, *54*(7), 4621.

[31] Gomez-Heredia, C. L., Ramirez-Rincon, J. A., Ordonez-Miranda, J., Ares, O., Alvarado-Gil, J. J., Champeaux, C., & Joulain, K. (2018). Thermal hysteresis measurement of the VO_2 emissivity and its application in thermal rectification. *Scientific Reports*, *8*(1), 8479.

[32] Trotter, D. M., & Sievers, A. J. (1980). Spectral selectivity of high-temperature solar absorbers. *Applied optics*, *19*(5), 711-728.

[33] Kim, D. H., & Kwok, H. S. (1994). Pulsed laser deposition of VO_2 thin films. *Applied physics letters*, *65*(25), 3188-3190.

[34] Yang, T. H., Aggarwal, R., Gupta, A., Zhou, H., Narayan, R. J., & Narayan, J. (2010). Semiconductor-metal transition characteristics of VO_2 thin films grown on c-and r-sapphire substrates. *Journal of Applied Physics*, *107*(5), 053514.

[35] Benkahoul, M., Chaker, M., Margot, J., Haddad, E., Kruzelecky, R., Wong, B., & Poinas, P. (2011). Thermochromic VO_2 film deposited on Al with tunable thermal emissivity for space applications. *Solar Energy Materials and Solar Cells*, *95*(12), 3504-3508.

[36] Nazari, M., Zhao, Y., Kuryatkov, V. V., Fan, Z. Y., Bernussi, A. A., & Holtz, M. (2013). Temperature dependence of the optical properties of VO_2 deposited on sapphire with different orientations. *Physical Review B*, *87*(3), 035142.

[37] Houska, J., Kolenaty, D., Rezek, J., & Vlcek, J. (2017). Characterization of thermochromic VO2 (prepared at 250°C) in a wide temperature range by spectroscopic ellipsometry. *Applied Surface Science*, *421*, 529-534.

[38] Théry, V., Boulle, A., Crunteanu, A., Orlianges, J. C., Beaumont, A., Mayet, R., & Fabert, M. (2016). Role of thermal strain in the metal-insulator and structural phase transition of epitaxial VO_2 films. *Physical Review B*, *93*(18), 184106.

[39]Teledyne_Judson_Technologies, http://www.teledynejudson.com/prods/Documents/PB2 12.pdf. Accessed 25 November 2016

[40] Huffman, T. J., Lahneman, D. J., Wang, S. L., Slusar, T., Kim, B. J., Kim, H. T., & Qazilbash, M. M. (2018). Highly repeatable nanoscale phase coexistence in vanadium dioxide films. *Physical Review B*, *97*(8), 085146.

[41] Liang, J., Hu, M., Kan, Q., Liang, X., Wang, X., Li, G., & Chen, H. (2011). Infrared transition properties of vanadium dioxide thin films across semiconductor-metal transition. *Rare Metals*, *30*(3), 247.

[42] Qazilbash, M. M., Brehm, M., Andreev, G. O., Frenzel, A., Ho, P. C., Chae, B. G., & Shpyrko, O. G. (2009). Infrared spectroscopy and nano-imaging of the insulator-to-metal transition in vanadium dioxide. *Physical Review B*, *79*(7), 075107.

[43] Pekker, S., & Eyring, E. M. (1986). Measurement of Phase Transitions by Photothermal Radiometry: The Semiconductor-to-Metal Transition of Vanadium (IV) Oxide, VO_2. *Applied spectroscopy*, *40*(3), 397-401.

[44] Ordonez-Miranda, J., Ezzahri, Y., Drevillon, J., & Joulain, K. (2016). Dynamical heat transport amplification in a far-field thermal transistor of VO_2 excited with a laser of modulated intensity. *Journal of Applied Physics*, *119*(20), 203105.

[45] Ramirez-Rincon, J. A., Gomez-Heredia, C. L., Corvisier, A., Ordonez-Miranda, J., Girardeau, T., Paumier, F., & Ares, O. (2018). Thermal hysteresis measurement of the VO_2 dielectric function for its metal-insulator transition by visible-IR ellipsometry. *Journal of Applied Physics*, *124*, 195102.

[46] Kats, M. A., Sharma, D., Lin, J., Genevet, P., Blanchard, R., Yang, Z., & Capasso, F. (2012). Ultra-thin perfect absorber employing a tunable phase change material. *Applied Physics Letters*, *101*(22), 221101.

5. Optical properties of VO₂ thin films for its metal-insulator transition using spectroscopic ellipsometry

5.1. Introduction

In chapters 2 and 3 photothermal techniques have been used to perform theoretical and experimental characterization of thin films deposited on metallic substrates. These analyses showed that for multi-layer samples, the dependence of the photothermal signals with the thermal properties of the layer j is conditioned to satisfied that $\mu_j \sim L_j$, where L_j is the thickness and $\mu_j = \sqrt{2\alpha_j/\pi f}$ is the thermal diffusion length associated with thermal diffusivity (α_j) and modulation frequency (f) [1]. For thin films ($L < 1$ μm) this condition requires modulation frequencies higher than 10^9 Hz [2], therefore, in the opposite range (< 5 KHz), the emissivity and the light into-heat conversion efficiency of solar selective coatings based on metal oxides (BN-Ni and TiNOX), were associated with the amplitude signals measured by using photothermal radiometry (PTR) and photoacoustic spectroscopy (PAS)

In chapter 4, photothermal signals for materials of inhomogeneous internal structures and composition, such as polyester resin, solar selective coatings and VO$_2$ thin films, have been studied. In the case of vanadium dioxide, as a consequence of the inhomogeneity of the surface at the intermediate state [3,4], just when dielectric (monoclinic) and metallic (rutile) domains coexist in the structural change, the VO$_2$ layer presents scattered infrared emission, which modifies the photothermal signals complicating the optical characterization. Therefore, the correct characterizacion of VO$_2$ thin films requires highly accurate optical techniques, in order to describe the evolution of its properties across the insulator-to metal phase transition.

5.2. Framework: Ellipsometry and VO$_2$ measurements

Several recent theoretical and experimental studies have reported the suitability of VO$_2$ thin films for technological applications related to thermal energy management, such as, smart windows [5], infrared (IR) absorbers for sensing process [6], IR reflectors for space devices [7], as well as the modulation, amplification, and rectification of radiative heat currents [8,9,10]. All of these applications require the accurate characterization of the VO$_2$ optical performance in a given spectral range. For instance, in solar energy applications, the reflectance and transmittance in the visible (Vis) and near-infrared (NIR) spectra [5,11] (from 0.3 to 2.5 μm) are of primary interest, while the emissivity for wavelengths longer than 2.5 μm is the most suitable for thermal energy applications [12]. These optical properties have been successfully measured for a VO$_2$ film+substrate system through convectional reflectance spectroscopy in the Vis-IR spectrum [5,13]. This methodology requires a delicate analysis to single out the substrate contribution, whose impact is expected to be strong in the insulating phase of VO$_2$, because of its high transmittance in the IR region [14]. Vis-IR ellipsometry thus emerges as a reliable technique for the direct optical characterization of VO$_2$ thin films at a given temperature, by using robust modelling that takes into account the layered structured of samples, to properly interpret the ellipsometric signals Psi (Ψ) and Delta (Δ) [11]. This chapter is focused on the optical characterization of VO$_2$ (120 nm)+r-plane sapphire and VO$_2$ (200 nm)+c-plane sapphire samples studied in chapter 4, by using spectroscopic ellipsometry in the spectral range of 0.4 to 15 μm.

Optical characterization of VO$_2$ by using spectroscopic ellipsometry has been reported by several authors, mostly in the Visible-NIR spectra (of 0.4 to 2.5 μm). Nasari *et al* [15]. reported measurements for VO$_2$ thin films grown on c-, m-, and r-plane sapphire, below the NIR spectral range (0.2 to 2 μm), and showed that: (1) the main variations of the real and imaginary parts of the dielectric function (ε) of VO$_2$, between its insulating and metallic states, occur for wavelengths longer than 0.5 μm and 0.8 μm, respectively; (2) The transition temperatures of the VO$_2$ films deposited on m- and r-plane sapphire are around 10ºC lower than the one determined for the film grown on c-plane sapphire. This indicates that the substrate, as well as the deposition process characteristics, can modify the VO$_2$ phase transition [16,17]. Furthermore, the metal-insulator variations of the refractive index (*n*) and extinction coefficient (*k*) of about 50% and 97% respectively, were measured by means of Vis-NIR (0.6 - 2 μm) ellipsometry for a VO$_2$ thin film deposited on a silicon substrate [18]. These significant variations involve a change in the sample optical transmittance of about 88% between room temperature (IR transparent) and 70ºC (IR opaque). On the other hand, Qazilbash *et al.* reported the real part of the optical conductivity (i.e. the imaginary part of the dielectric function) of a 100 nm-thick film of VO$_2$ grown on r-plane sapphire, across the MIT and for wavelengths from 0.6 to above 15 μm [19]. Based on the combination of ellipsometric measurements and images of near-field scattering, these authors showed that the surface structure of the VO$_2$ film changes with temperature, as a result of the coexistence of the insulator and metallic phases at temperatures $T{\sim}T_C$. Taking into account that the imaginary part of the optical conductivity (i.e. the real part of the dielectric function) in the IR region still remains unexplored, the complete measurement of the real and imaginary parts of the VO$_2$ dielectric function in a wide interval of visible and IR wavelengths is required, for temperatures within the MIT.

5.3. Visible-IR Ellipsometry

5.3.1. Experimental setup and methodology

The ellipsometric characterization of our VO$_2$ thin films has been performed within its MIT and in the spectral range from 0.4 to 15 μm (incident angle 70º), in two steps: First, the ellipsometric

signals Ψ and Δ have been measured from 0.4 to 1.7 µm using a M-2000 J. A. Woollam Co. Inc Ellipsometer [see Fig. 5.1(a)]. For this experimental setup, the sample temperature (1) is measured with a K-thermocouple (0.05 mm in diameter) connected to thermocouple monitor (2) (2-Channel Handheld Digital Thermometer) and controlled with a Peltier cell (3), which switches the applied voltage with a power supply (4) in steps of 0.1 V every 5 minutes, leading to temperature changes of about 2ºC in the range from 20 to 80ºC. Second, the signals Ψ and Δ are measured in the complementary wavelength interval from 1.7 to 15 µm through the IR-VASE Mark-II J. A. Woollam Co. Inc Ellipsometer [see Fig. 5.1(b)], equipped with a built-in cryostat (5) (CRV-725V Janis Research Co), which allows the incoming (source) and outcoming (reflected) light through two IR windows. The sample temperature is control with a VASE Ellipsometer Control Module (7) (VB-400 J. A. Woollam Co of sensitive 0.1ºC) in steps of 2ºC every 45 minutes, under a pressure of 5×10^{-7} Torr. In both experimental setups, the temperature has been measured on the heated surface, rather than on the VO$_2$ surface, which induces a temperature offset of 3ºC (10ºC) in Vis-NIR (IR) measurements, compared to the real temperature of the sample. These temperature shifts have been taken into account throughout our analysis.
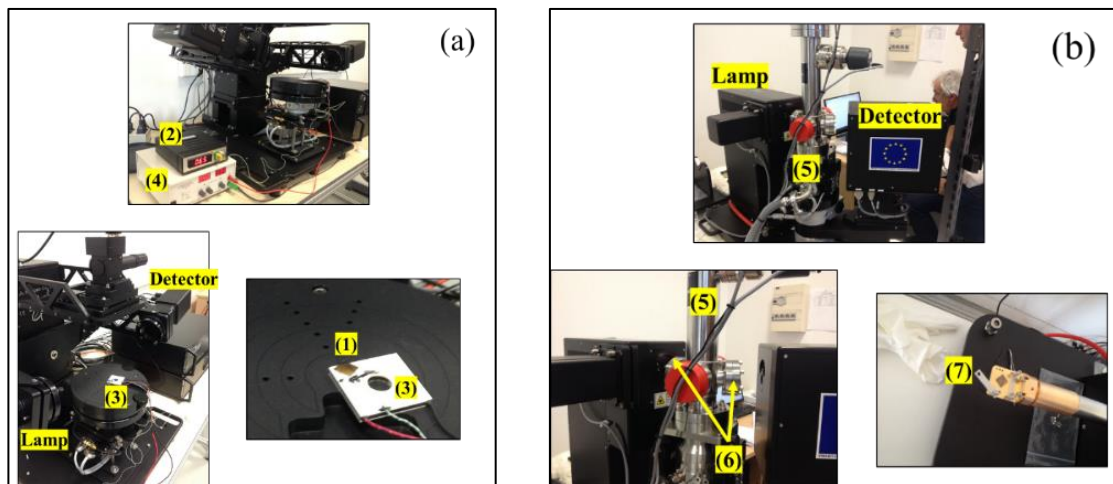

Fig. 5.1. Images of the ellipsometry experimental setup by using (a) M-2000 J. A. Woollam Co. Inc Ellipsometer for the range of 0.4 to 1.7 µm and (b) IR-VASE Mark-II J. A. Woollam Co. Inc Ellipsometer for the range of 1.7 to 15 µm. (1) Sample, (2) thermocouple monitor, (3) Peltier cell, (4) Power supply, (5) Cryostat, (6) IR windows and (7) Temperature control module.

The ellipsometric signals Ψ and Δ measured for the VO$_2$ sample in the spectral range from 0.4 to 15 µm, for different temperatures within the MIT, have been analyzed by means of the CompleteEASE^{TM} data analysis software of *J.A. Woollam Co., Inc*. The samples have been modelled as a three-layer system involving the sapphire substrate, the VO$_2$ thin film, and the interface roughness. Taking into account that the optical properties of sapphire are expected to remain constant for the considered range of temperatures around the VO$_2$ MIT [20], the fitting process consists of assigning different oscillator models (see Sec 1.2) across its insulator-to-metal transition as shown below, in order to determine the spectral refractive index (n) and extinction coefficient (k) for different temperatures. The real ε_R and imaginary ε_I parts of the complex dielectric function ε have then been obtained by using the relation $\sqrt{\varepsilon} = n + ik$ [21].

- Dielectric ($T \ll T_C$): $\varepsilon(E) = [\varepsilon_I(\infty) + \varepsilon_{I-TL}(E)] + \varepsilon_{R-TL}(E)$
- Transition ($T \sim T_C$): $\varepsilon(E) = [\varepsilon_I(\infty) + \varepsilon_{I-TL}(E) + \varepsilon_{I-G}(E)] + [\varepsilon_{R-TL}(E) + \varepsilon_{R-G}(E)]$
- Metal ($T \gg T_C$): $\varepsilon(E) = [\varepsilon_I(\infty) + \varepsilon_{I-D}(E) + \varepsilon_{I-G}(E)] + [\varepsilon_{R-D}(E) + \varepsilon_{R-G}(E)]$

5.3.2. Ellipsometric signals and fitting process

The ellipsometric signals Ψ and Δ measured in the spectral range from 0.4 to 15 µm for the VO$_2$ thin film deposited on r-plane sapphire, are respectively shown in Fig. 5.2(a) and 5.2(b), for three relevant temperatures. In the insulating phase of VO$_2$ ($T \ll T_C$), both Ψ and Δ exhibit a strong dependence on the substrate properties (dashed lines), especially for wavelengths comparable to or higher than 2.0 µm, where VO$_2$ shows its maximum transmittance (i.e. $\varepsilon_I = 0$) [13,22]. In this insulating phase, the VO$_2$ dielectric function is determined by fitting the experimental data (Ψ and Δ) with the Tauc-Lorentz (TL) oscillator model of Eq. (1.16), which has been successfully applied in previous work [15,23,24]. This fitting procedure also enables to calculate the VO$_2$ band gap, whose value for our sample is 0.35 eV, which agrees rather well with many studies reported in the literature [15,19,23].
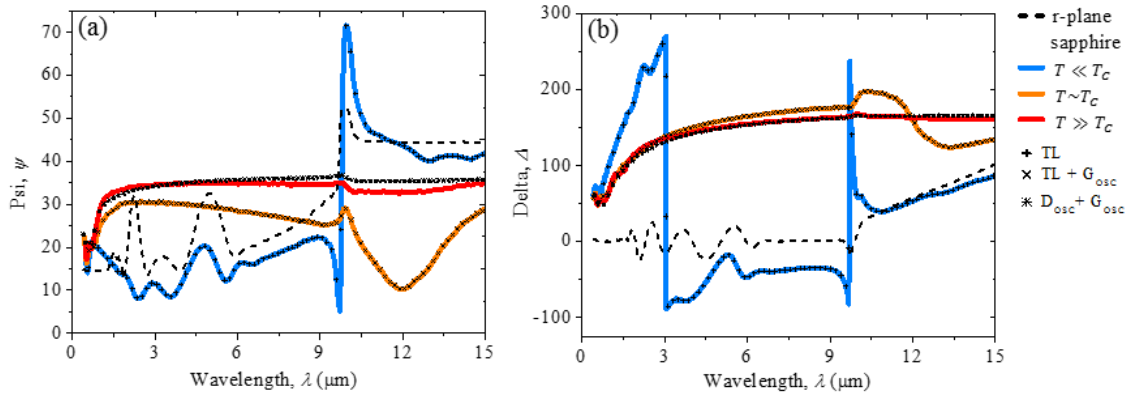
Optical properties of VO$_2$ thin films for its metal-insulator transition using spectroscopic ellipsometry

Fig. 5.2. Temperature dependence of the spectral ellipsometric signals (a) Ψ and (b) Δ of VO$_2$+r-plane sapphire sample. The symbols $+$, $\times$, and $*$ stand for the fitted data obtained using the Tauc-Lorentz (TL), Tauc-Lorentz+Gaussian (TL+G$_{OSC}$), and Drude+Gaussian (D$_{OCS}$+G$_{OSC}$) oscillator models, respectively. Dashed lines correspond to ellipsometric signals of r-plane sapphire substrate at room temperature.

As the sample temperature rises to values $T \sim T_C$, the spectral behavior of Ψ and Δ significantly changes, due to the metallic domains arising inside the insulating layer [4,22,23]. This coexistence of the insulating and metallic phases allows us to describe the VO$_2$ film as a composite material, for which the fitting of both ellipsometric signals has been carried out by including a Gaussian oscillator (G$_{OSC}$) in the Tauc-Lorentz (TL) model. The combination of these oscillators has been previously explored for numerous dielectric compounds and has been demonstrated to provide a suitable description of the optical properties of solid crystalline samples [25,26], through a better simulation of the electronic transitions and electron-phonon scattering in wide ranges of wavelengths [27,28]. Finally, at high temperatures ($T \gg T_C$), as a consequence of the poor optical properties of the metallic VO$_2$ below 1.5 μm compared with the IR region (above 3 µm), the dielectric function has been determined by combining a Gaussian oscillator with the Drude model (D$_{OSC}$ + G$_{OSC}$). Even though we have also investigated other alternative models, such as those related with Lorentzian oscillators [18], the best fits of both spectral signals Ψ and Δ measured for our VO$_2$ sample has been obtained by the combination of the Tauc-Lorentz, Gaussian, and Drude oscillators.

The ellipsometric signals of VO$_2$+c-plane sapphire sample are shown in Fig. 5.3 across its MIT during the heating process. In the insulating and intermediated phases ($T \ll T_C$ and $T \sim T_C$), the

dielectric function is determined using the same Tauc-Lorentnz and Guassian oscillator models, but at high temperatures $(T \gg T_C)$, unlike that obtained for VO$_2$+r-plane sapphire, the ellipsometric signals of VO$_2$ grown on c-plane sapphire do not present metallic-like behavior and therefore it was not possible to apply the Drude oscillator. This difference is related with the structural characteristics of the VO$_2$ crystals on each substrate, as has been shown in Sec 4.4 of chapter 4.
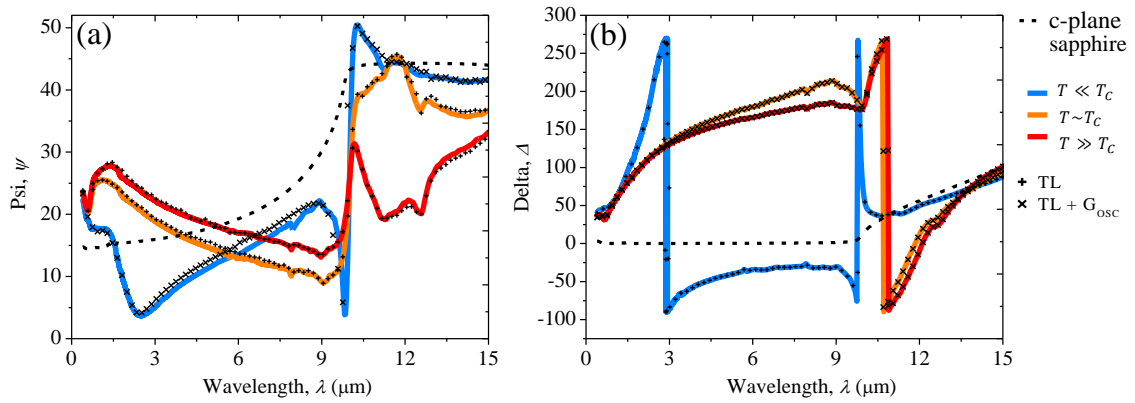

Fig. 5.3. Temperature dependence of the spectral ellipsometric signals (a) Ψ and (b) Δ of VO$_2$+c-plane sapphire sample. The symbols $+$, $\times$, stand for the fitted data obtained using the Tauc-Lorentz (TL) and Tauc-Lorentz+Gaussian (TL+G$_{OSC}$) oscillator models respectively. Dashed lines correspond to ellipsometric signals of c-plane sapphire substrate at room temperature.

Table 5.1. summarizes the fitted parameters using the optical model given by Eqs. (1.16 - 1.18) at $T \ll T_C$ and $T \gg T_C$. The fitting curves shown in Figures 5.2 and 5.3 for VO$_2$+r-sapphire and VO$_2$+c-sapphire, respectively, have been obtained by minimization of the mean square error (MSE) values, which represent the difference between the experimental and theoretical data of the ellipsometric parameters Ψ and Δ. The VO$_2$ thin film thickness (roughness) obtained for both samples show a good agreement $< 8\%$ ($\sim 10\%$) with those obtained by profilometry (AFM analysis). In the insulator phase, the values found for the band gap (E_{gap}) of 0.35 eV and 0.53 eV agree with those reported in the literature for VO$_2$ films grown on r-plane and c-plane sapphire substrates, respectively [8,15,23]. At $T \gg T_C$ the E_{gap} collapses to zero for the VO$_2$+r-sapphire sample, while for the other one it decreases to 0.16 eV. This remarkable difference between the E_{gap} of the samples has been previously reported by Nazari $et.$ $al.$ for VO$_2$ thin films grown via sputtering on the same substrates under study. Therefore, the weak connectivity

of the VO$_2$ crystals induced by the c-sapphire substrate (see Fig. 4.12), make the percolation process difficult, which is transcendental in the metallic properties of VO$_2$ surface.

Table 5.1. TL, G$_{OSC}$ and D$_{OSC}$ models fit parameters of the studied VO$_2$ thin films deposited via PLD on r-plane and c-plane sapphire substrates. MSE is the mean square error of each fit. $\varepsilon_R(\infty)$ is a constant contribution to the dielectric function at higher (shorter) energies (wavelengths). A (A_G), E_0 (E_G) and B (B_G) represent the amplitude, peak central energy and broadening of the amplitude of TL (Gaussian) oscillator. E_{gap} is the optical band gap. ρ and τ represent the resistivity and scattering time of D$_{OSC}$ model respectively.

Parameter	VO₂ / r-plane sapphire		VO₂ / c-plane sapphire	
	$T \ll T_C$ TL	$T \gg T_C$ Drude+G$_{OSC}$	$T \ll T_C$ TL	$T \gg T_C$ TL+G$_{OSC}$
MSE	23.07	27.10	22.48	21.62
Thickness (nm)	111.11 ± 1.03	128.01 ± 2.54	202.74 ± 1.27	200.73 ± 2.46
Roughness (nm)	12.65 ± 0.55	13.12 ± 0.78	23.35 ± 0.75	22.99 ± 0.57
$\varepsilon_R(\infty)$	2.10 ± 0.13	1.93 ± 0.21	3.78 ± 1.24	4.61 ± 0.74
A (eV)	22.84 ± 1.01	***	19.53 ± 0.88	52.50 ± 3.28
B (eV)	1.31 ± 0.12	***	2.07 ± 0.09	3.01 ± 0.61
E_0 (eV)	2.57 ± 0.12	***	1.30 ± 0.06	0.26 ± 0.08
E_{gap} (eV)	0.35 ± 0.01	***	0.53 ± 0.01	0.16 ± 0.04
A_G (eV)	***	97.9 ± 2.01	***	33.07 ± 0.52
B_G (eV)	***	0.13 ± 0.07	***	0.17 ± 0.04
E_G (eV)	***	5.60 ± 0.95	***	0.13 ± 0.01
ρ (Ω μm)	***	2.86 ± 0.62	***	***
τ (fs)	***	$\mathbf{0.98 \pm 0.02}$	***	***

5.4. Dielectric function

The real (ε_R) and imaginary (ε_I) parts of the dielectric function in the spectral range from 0.4 to 15 μm are shown in Figures 5.4(a), 5.4(c) and 5.4(b), 5.4(d), for various temperatures set

during the heating and cooling processes of the VO$_2$/r-plane sapphire sample, respectively. In the insulator phase (heating: 20ºC < T <63ºC and cooling: 20ºC < T < 55ºC), ε_R remains near zero through the whole spectrum [see Fig. 5.4(a)-(b)], as is the typical behavior of dielectric materials, while $\varepsilon_I \approx 0$ in the IR region [Fig. 5.4(c)-(d)], as a result of the low reflectance of the VO$_2$ film surface at $T \ll T_C$ [29]. On the other hand, at high temperatures (T >69ºC), the sample reaches the metallic phase characterized by negative values of ε_R and a monotonous increase of ε_I with the NIR-IR wavelength, which is consistent with the data reported by Qazilbash *et.al.* [19,23], for the real part of the optical conductivity, and induces sizeable changes in the reflectance of VO$_2$ films [27].
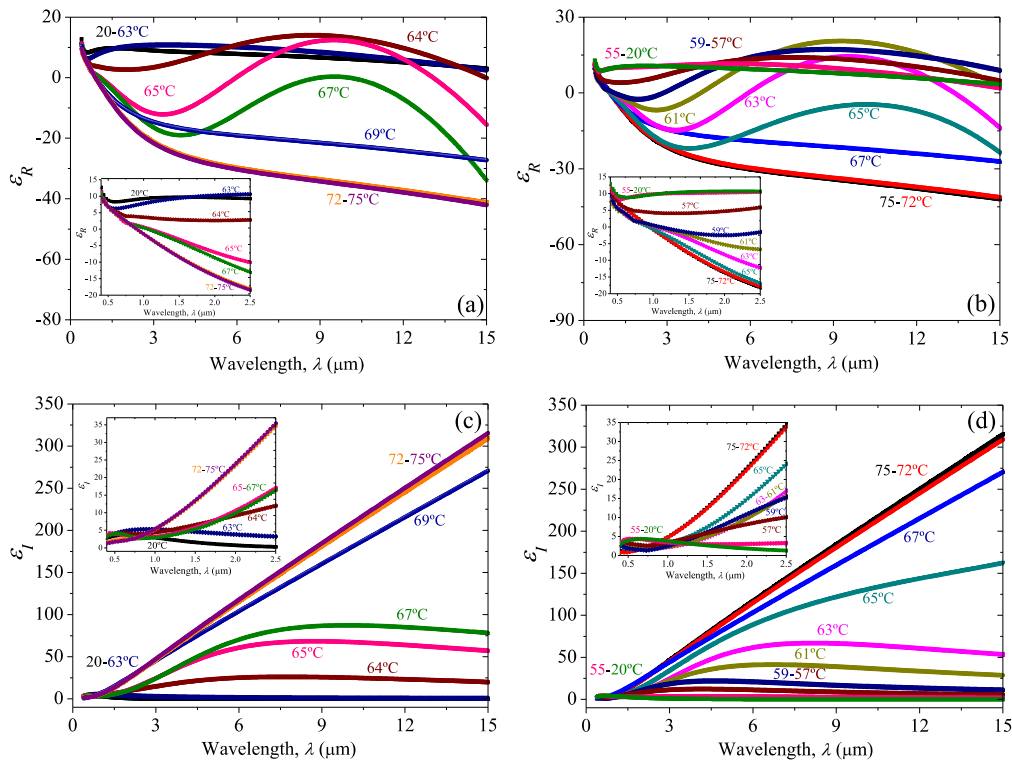
Fig. 5.4. Temperature dependence of the real (ε_R) and imaginary (ε_I) part of the dielectric function of the VO$_2$ deposited on r-plane sapphire, during its heating (a, c) and cooling (b, d) processes, in the spectral range from 0.4 to 15 μm. Insets show the behavior of ε_R and ε_I in the shorter wavelength range (0.4 – 2.5) μm.

At intermediate temperatures (from 64ºC to 67ºC in the heating process and 65ºC to 57ºC in the cooling process), both ε_R and ε_I display a mixed spectrum with a metallic-like behavior for wavelengths smaller than 3 μm and 5 μm, respectively; and an insulator-like phase around 10

µm. This latter behavior, known as anomalous absorptance [6], is due to the interference processes that appear at specific wavelengths, for which the substrate exhibits high reflectivity and the optical constants of the VO$_2$ film satisfy the condition $n \sim k$ [30]. In the present case, this interference shows up during the predominant growth of metallic domains inside the thin film ($T \sim T_C$), which increases the values of ε_I (i.e. $k \neq 0$) around 10 µm, where the sapphire substrate presents the highest IR reflectivity [13,30]. According to the insets of Fig. 5.4, for visible wavelengths (from 0.4 to 0.8 µm) both the real and imaginary parts of the dielectric function exhibit relatively small variations compared to those in the NIR region (above 1.5 µm), for which the film behaves as a metal with $\varepsilon_I \gg 1$, for $T \gg T_C$. These results are consistent with those reported by Nazari *et.al.* and Seal *et.al* for VO$_2$ thin films deposited on sapphire [15,31].

Fig. 5.5. Hysteresis loop of the real ε_R (red) and imaginary ε_I (blue) parts of the VO$_2$/r-sapphire dielectric function at λ= 10 µm, for the heating (full symbols) and cooling (empty symbols) processes.
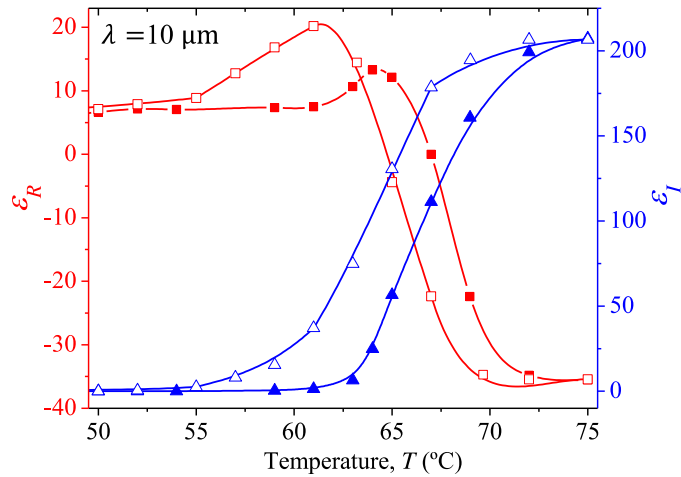
Fig. 5.5 shows the temperature dependence of the real (ε_R) and imaginary (ε_I) parts of the dielectric function at the wavelength of 10 μm. Within the MIT, ε_R (ε_I) decreases (increases) during the heating process and increases (decreases) for the cooling process following a different path, which leads to a hysteresis loop. This behavior of ε_I has also been found for the IR reflectance of VO$_2$ films deposited on sapphire [13,14], while that of ε_R has not been reported before, to the best of our knowledge. The hysteresis curve of ε_R is characterized by: (i) Negative values of ε_R for $T \gg T_C$, which is characteristic of metals due to their usual high

extinction coefficient [27], and (ii) the presence of a maximum related to the anomalous energy absorption of VO$_2$, which for the cooling process is higher than during heating, as a consequence of the relatively longer coexistence of both phases before returning to the insulator phase. Furthermore, the transition temperature (average temperature of the peaks of $\partial \varepsilon_R / \partial T = 0$ and $\partial \varepsilon_I / \partial T = 0$ during the heating and cooling processes [17]) of both ε_R and ε_I is around $T_c \approx 64.5°C$, and the hysteresis width associated to the MIT reversibility is $\Delta H \approx 3.2°C$. These values are consistent with those determined from VO$_2$ integrated emissivity in Ref [32].
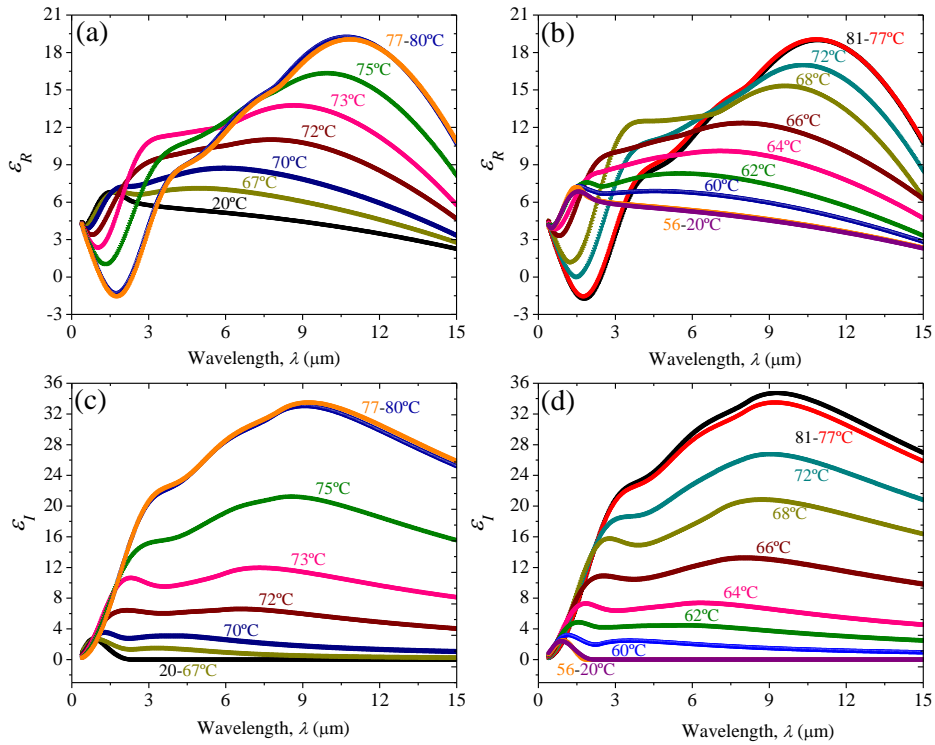
Fig. 5.6. Temperature dependence of the real (ε_R) and imaginary (ε_I) part of the dielectric function of the VO$_2$ film deposited on c-plane sapphire substrate, during its heating (a, c) and cooling (b, d) processes, in the spectral range from 0.4 to 15 μm.

The dielectric function (ε_R and ε_I) of the VO$_2$/c-plane sapphire sample is shown in Fig. 5.6 at various temperatures during the heating and cooling processes. In the insulator phase (heating: 20°C < T < 67°C and cooling: 20°C < T < 62°C), similar to the behavior observed for VO$_2$+ r-plane sapphire, ε_R keeps near zero through the whole spectrum, while $\varepsilon_I \approx 0$ in the IR region, which is the result of the low reflectance of the VO$_2$ film surface. At intermediate temperatures

from 70ºC to 75ºC in the heating process and 72ºC to 64ºC in the cooling process, ε_R displays a small decrease (increase) for wavelengths smaller (longer) than 2 µm , with a peak around 10 µm related with the characteristic anomalous absorptance of VO$_2$ thin films deposited on sapphire (see Fig. 5.5) [30]. On the other hand, ε_I takes higher values as the temperature increases due to changes in the reflectance of the surface. Finally, at high temperatures ($T >$ 75ºC), in contrast to the VO$_2$+r-plane sapphire sample, the dielectric function does not reach the characteristic behavior of metallic surfaces in the IR region ($\varepsilon_R <0$ and $\varepsilon_I >100$) as expected according to the results shown in Fig. 5.3 and Table 5.1.

5.5. Effective medium theory

Taking into account that the MIT of VO$_2$ is driven by the coexistence of metallic and insulating domains [3,4,19,23,33], VO$_2$ can be considered as a composite made up of metallic (insulating) domains embedded in an insulating (metallic) matrix [15], during its heating (cooling) process. The temperature evolution of these domains is characterized by the percolation of the VO$_2$ properties, which, for the case of the VO$_2$ dielectric function ε, can be well described by the Bruggeman symmetrical model [34], as follows

$$f_M \frac{\varepsilon_m(\lambda) - \varepsilon(\lambda)}{q\varepsilon_m(\lambda) + (1-q)\varepsilon(\lambda)} + (1 - f_M) \frac{\varepsilon_i(\lambda) - \varepsilon(\lambda)}{q\varepsilon_i(\lambda) + (1-q)\varepsilon(\lambda)} = 0, \tag{5.1}$$

where f_M and $1 - f_M$ stand for the volumetric fractions of the metallic and dielectric domains during the heating process, respectively, ε_m and ε_i are the respective dielectric functions of VO$_2$ in its metallic and insulating phases, and q is the depolarization factor defined by the of the domains' shape.
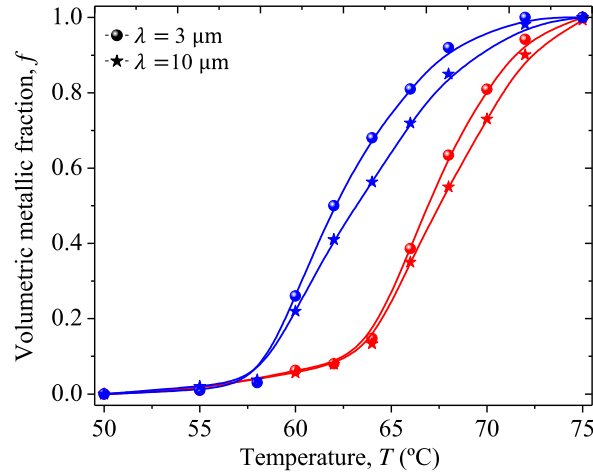
Fig. 5.7. Temperature evolution of the VO$_2$/r-plane sapphire volumetric metallic fraction determined by means of the Bruggeman model at 3 μm (circles) and 10 μm (stars), for the heating (red) and cooling (blue) processes.

Considering the dimensionality of VO$_2$ /r-sapphire sample (thickness=120 nm area=10×10 mm^2), we have taken $q = 0.5$ (flat domains mainly), as was considered previously for this effective medium theory (EMT) [35]. For the cooling process, the insulating domains show up inside the metallic matrix and therefore the volume fractions f_M and $1 - f_M$ must be interchanged in Eq. (5.1). By inserting the experimental values of ε, ε_m and ε_i shown in Fig. 5.4 into Eq. (5.1), the temperature evolution of f_M has been determined and is shown in Fig. 5.7, for two IR wavelengths, wherein VO$_2$ (deposited on r-plane sapphire) exhibits the largest differences between the insulating and metallic phases. Note that for the heating process, f_M increases monotonously from zero, in the insulating phase, to one, in the metallic phase, as expected. At the critical temperature $T_C = 64°C$, $f_M \approx 0.1$, for both wavelengths. In the cooling process, on the other hand, the metallic fraction remains around 0.8 until 66°C and then linearly decreases to zero, leading to the expected hysteresis loop. The similar behavior and values of f_M for both IR wavelengths indicates that volumetric metallic fraction is nearly independent of the wavelength, as established by Eq. (5.1).
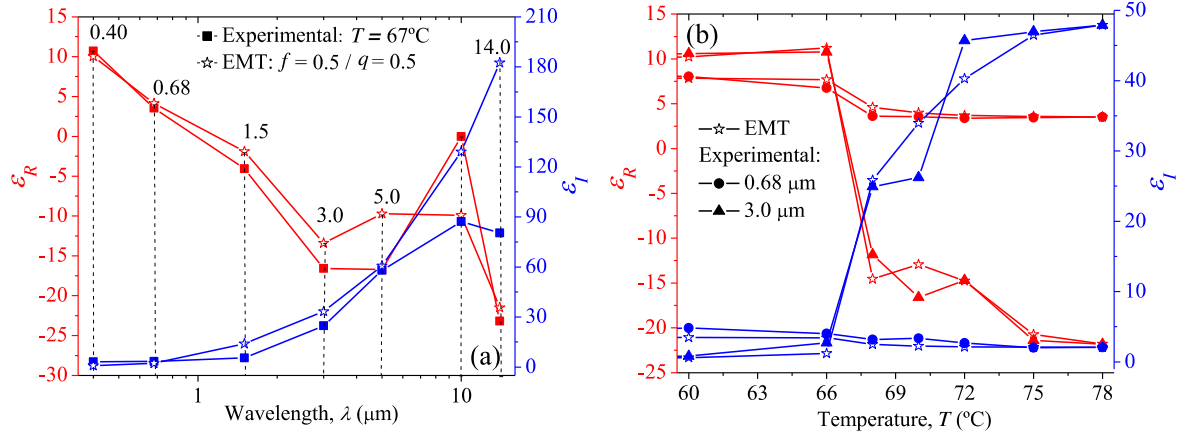
Fig. 5.8. Comparison of the measured real ε_R (red) and imaginary ε_I (blue) parts of the VO$_2$/r-plane sapphire dielectric function (full symbols) with their corresponding theoretical counterparts (stars) predicted by Eq. (5.1), as functions of the (a) wavelength and (b) temperature within the MIT. Calculations have been done with the average volumetric metallic fraction shown in Fig. 5.7 for two representative wavelengths.

Figures 5.8(a) and 5.8(b) show the comparison of the measured real ε_R (red) and imaginary ε_I (blue) parts of the VO$_2$ dielectric function with their corresponding theoretical counterparts predicted by Eq. (5.1), as functions of the wavelength and temperature, respectively. Note that the theoretical values of ε_R are in good agreement with the experimental data in the Vis-NIR region (0.4 to 3 µm), while those of ε_I show a good description of their experimental counterparts in the spectral range 0.4 to 5 µm. It is therefore clear that the Bruggeman EMT can describe well the spectral behavior of the VO$_2$ dielectric function for wavelengths smaller than 3 µm mainly.

5.6. Infrared reflectivity and volumetric metallic fraction

Figure 5.9 shows the temperature evolution of the VO$_2$ surface reflectivity (r) for two IR wavelengths wherein VO$_2$ exhibits the largest differences between the insulating and metallic phases. Moreover, it is compared with the volumetric metallic fraction calculated using the effective medium theory [see Eq. (5.1)]. The reflection has been calculated from the dielectric function presented in Figures 5.4 and 5.6 for VO$_2$+r-sapphire and VO$_2$+c-sapphire samples respectively, by means of the Fresnel reflection coefficient ($r = \left| (\sqrt{\varepsilon} - 1)/(\sqrt{\varepsilon} + 1) \right|^2$). Note

that in both cases the surface reflectivity follows the same behavior as the volumetric metallic fraction across the MIT. This is because high reflectance in the IR region is one of the main characteristics of metals, therefore, as the volume of metal increases in the VO$_2$ film, the reflection of the surface rises. As a result, this macroscopic property could be used to quantify the percentage of metallicity of the composite samples. Finally, making a comparison between the MIT characteristics (critical temperature and hysteresis width) of the VO$_2$ samples as shown in Table 5.2, a strong dependence on the substrate is found [15,32].
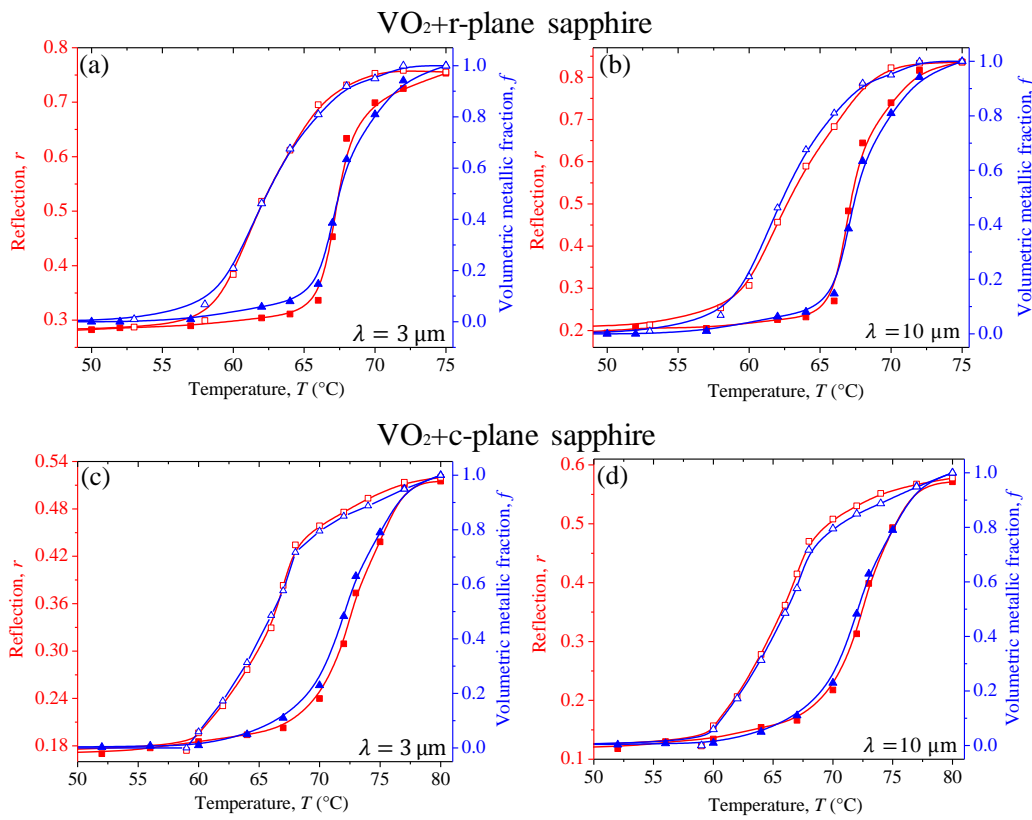

Fig. 5.9. Temperature evolution of the VO$_2$ reflection (red) at 3 μm and 10 μm, compare with volumetric metallic fraction (blue) determined by means of the Bruggeman model of Eq. (1) during the heating (full symbols) and cooling (empty symbols) processes for the VO$_2$+r-plane sapphire (a-b) and VO$_2$+c-plane sapphire (c-d) samples.

Table 5.2. MIT characteristics of VO$_2$ thin films deposited via PLD on r-plane and c-plane sapphire substrates.

Parameter	VO$_2$ / r-plane sapphire	VO$_2$ / c-plane sapphire
Temperature transition, T_c	64.5°C	67.5°C
Hysteresis width, ΔH	3.4°C	5.9°C
Reflection change (10 μm), Δr	76%	79%

5.7. Emissivity calculation across the MIT

The VO$_2$ dielectric function shown in Fig. 5.4 is now used to determine the reflectance $R(\lambda)$ and transmittance $T_r(\lambda)$ of VO$_2$/r-sapphire by means of the Fresnel equations for normal incidence [36]. According to Kirchhoff's law, the spectral emittance is then given by $1 - R(\lambda) - T_r(\lambda)$, whose average value ($\epsilon$) over the spectral wavelengths λ can be calculated by [37]

$$\epsilon = \frac{\int_0^\infty [1 - R(\lambda) - T_r(\lambda)]\Theta(\lambda, T)d\lambda}{\int_0^\infty \Theta(\lambda, T)d\lambda} = \frac{1}{\sigma T^4}\int_0^\infty [1 - R(\lambda) - T_r(\lambda)]\Theta(\lambda, T)d\lambda, \tag{5.2}$$

where $\Theta(\lambda, T) = C_1\lambda^{-5}/(e^{C_2/\lambda T} - 1)$ is the blackbody spectral radiance, $C_1 = 1.48 \times 10^{-15}$Wm^2, $C_2 = 1.43 \times 10^{-2}$m·K, and $\sigma = 5.67 \times 10^{-8}$ Wm^{-2}K^{-4}.

The spectral ratio of emitted power REP $= [1 - R(\lambda) - T_r(\lambda)]\Theta(\lambda, T)/\sigma T^4$ by the VO$_2$ thin film is shown in Fig. 5.10(a), for wavelengths from 2 to 20 μm. The spectral values above 15 μm have been obtained at each temperature by extrapolation. In the insulating phase ($T < 60$ °C), REP increases with temperature and its maximum changes of wavelength, as established by Wien's law. Within the MIT ($T \sim 68$°C), $R(\lambda)$ increases, $T(\lambda)$ decreases and REP falls down until reaching its metallic values. In addition, note that the main contribution to the average emissivity ϵ arises from the spectral range from 3 to 15 μm, where the VO$_2$ dielectric function has been measured. According to Fig. 5.10(b), the values of ϵ become independent of temperature for the pure metallic and insulating phases, as expected. Within the MIT, ϵ

decreases during the heating process and increases for the cooling process, following a different path, which leads to a hysteresis loop similar (T_c = 64.5°C, ΔH =3.1°C) to those found for the real and imaginary parts of the dielectric function (see Fig. 5.5). In the insulating phase, the value ϵ = 0.49 is lower than that measured by the thermal-wave resonant cavity (TWRC) technique [32], while the metallic emissivity ϵ = 0.16 agrees rather well with the value measured with this latter technique. This agreement in the metallic phase is reasonable, given that the VO$_2$ film is totally IR opaque, at high temperature, and hence the substrate effect becomes negligible. On the other hand, the difference in the insulating phase is explained by the IR semi-transparency of the VO$_2$ thin film, and therefore by the sapphire substrate, which is considered by our ellipsometric measurements, but not by the TWRC results, that considered the VO$_2$+substrate as a single effective layer [32]. The emissivity values shown in Fig. 5.10(b) thus correspond to the VO$_2$ thin without the substrate effect.
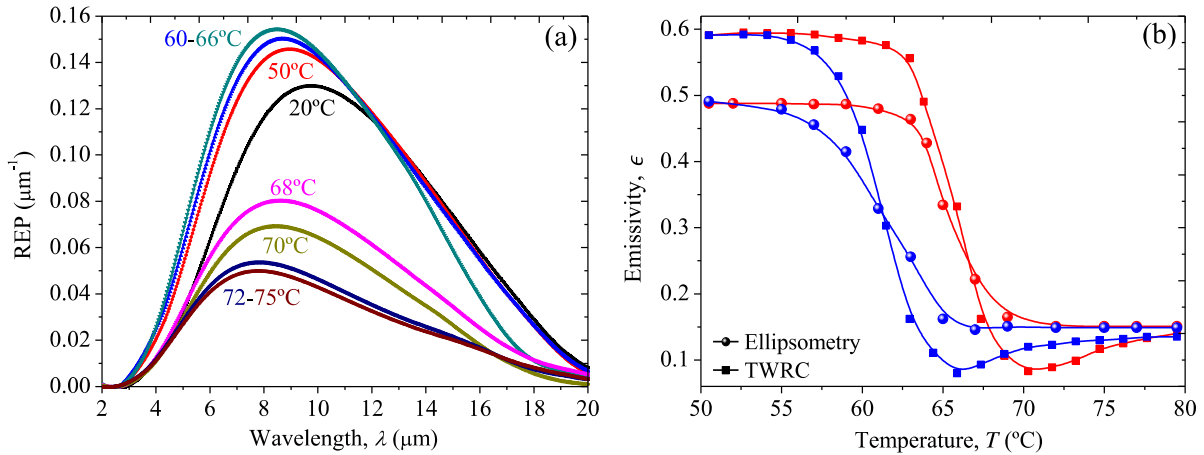
Fig. 5.10. (a) Spectral ratio of power emitted (REP) of a VO$_2$/r-plane film and its (b) average emissivity ϵ obtained for its heating (red) and cooling (blue) processes across the MIT. The spherical and square dots represent the values of ϵ determined by means of ellipsometry Eq. (5.2) and the TWRC technique [32].

5.8. Conclusions

We have measured the real and imaginary parts of the dielectric function of VO$_2$ thin films deposited on r-plane and c-plane sapphire via pulsed laser deposition, by means of visible-IR

Optical properties of VO$_2$ thin films for its metal-insulator transition using spectroscopic ellipsometry

ellipsometry for wavelengths ranging from 0.4 to 15 μm and temperatures within its full phase transition. This first-ever direct measurement of the VO$_2$ dielectric function has been achieved by combining the Tauc-Lorentz, Gaussian, and Drude oscillator models for describing the two ellipsometric signals in the insulating, insulating-metallic, and metallic phases of VO$_2$. The remarkable differences between both samples in the metallic state, confirm the important role of substrate in the optical properties of VO$_2$. By comparing the experimental data with the predictions of the Bruggeman effective medium model, it has been shown that this model is suitable to describe the VO$_2$ dielectric function for wavelengths smaller than 3 μm mainly. Furthermore, we have also determined the VO$_2$ emissivity averaged over a relevant interval of wavelengths for the sample deposited on r-sapphire and found that its values exhibit a hysteresis loop and change by a factor of three between its insulating and metallic phases.

References

[1] Ramírez-Rincón, J. A., Ares-Muzio, O., Macias, J. D., Estrella-Gutiérrez, M. A., Lizama-Tzec, F. I., Oskam, G., & Alvarado-Gil, J. J. (2018). On the use of photothermal techniques for the characterization of solar-selective coatings. *Applied Physics A*, *124*(3), 252.

[2] Oh, D. W., Ko, C., Ramanathan, S., & Cahill, D. G. (2010). Thermal conductivity and dynamic heat capacity across the metal-insulator transition in thin film VO$_2$. Applied Physics Letters, 96(15), 151906.

[3] Jones, A. C., Berweger, S., Wei, J., Cobden, D., & Raschke, M. B. (2010). Nano-optical investigations of the metal− insulator phase behavior of individual VO$_2$ microcrystals. *Nano letters*, *10*(5), 1574-1581.

[4] Kumar, S., Strachan, J. P., Kilcoyne, A. D., Tyliszczak, T., Pickett, M. D., Santori, C., & Williams, R. S. (2016). The phase transition in VO$_2$ probed using x-ray, visible and infrared radiations. *Applied Physics Letters*, *108*(7), 073102.

[5] Li, S. Y., Niklasson, G. A., & Granqvist, C. G. (2014). Thermochromic undoped and Mg-doped VO$_2$ thin films and nanoparticles: Optical properties and performance limits for energy efficient windows. Journal of Applied Physics, 115(5), 053513.

[6] Kats, M. A., Blanchard, R., Zhang, S., Genevet, P., Ko, C., Ramanathan, S., & Capasso, F. (2013). Vanadium dioxide as a natural disordered metamaterial: perfect thermal emission and large broadband negative differential thermal emittance. Physical Review X, 3(4), 041004.

[7] Benkahoul, M., Chaker, M., Margot, J., Haddad, E., Kruzelecky, R., Wong, B., & Poinas, P. (2011). Thermochromic VO$_2$ film deposited on Al with tunable thermal emissivity for space applications. Solar Energy Materials and Solar Cells, 95(12), 3504-3508.

[8] Ordonez-Miranda, J., Ezzahri, Y., Drevillon, J., & Joulain, K. (2016). Dynamical heat transport amplification in a far-field thermal transistor of VO$_2$ excited with a laser of modulated intensity. Journal of Applied Physics, 119(20), 203105.

[9] Joulain, K., Ezzahri, Y., Drevillon, J., & Ben-Abdallah, P. (2015). Modulation and amplification of radiative far field heat transfer: Towards a simple radiative thermal transistor. *Applied Physics Letters*, *106*(13), 133505.

[10] Prod'homme, H., Ordonez-Miranda, J., Ezzahri, Y., Drevillon, J., & Joulain, K. (2016). Optimized thermal amplification in a radiative transistor. Journal of Applied Physics, 119(19), 194502.

[11] Madida, I. G., Simo, A., Sone, B., Maity, A., Kana, J. K., Gibaud, A., & Maaza, M. (2014). Submicronic VO$_2$–PVP composites coatings for smart windows applications and solar heat management. Solar Energy, 107, 758-769.

[12] Leahu, G. L., Li Voti, R., Larciprete, M. C., Belardini, A., Mura, F., Fratoddi, I., & Bertolotti, M. (2014, June). Semiconductor-metal phase transition of vanadium dioxide nanostructures on silicon substrate: Applications for thermal control of spacecraft. In AIP Conference Proceedings (Vol. 1603, No. 1, pp. 62-70). AIP.

[13] Crunteanu, A., Cornette, J., Colas, M., Orlianges, J. C., Bessaudou, A., & Cosset, F. (2014). Electric field-assisted metal insulator transition in vanadium dioxide (VO$_2$) thin films: optical switching behavior and anomalous far-infrared emissivity variation. Proceedings SPIE 9364, Oxide-based Materials and Devices VI , SPIE, 2015, Proc. SPIE 9364, Oxide-based Materials and Devices VI, 9364, pp.93640J1-J11.

[14] Choi, H. S., Ahn, J. S., Jung, J. H., Noh, T. W., & Kim, D. H. (1996). Mid-infrared properties of a VO$_2$ film near the metal-insulator transition. Physical Review B, 54(7), 4621.

[15] Nazari, M., Zhao, Y., Kuryatkov, V. V., Fan, Z. Y., Bernussi, A. A., & Holtz, M. (2013). Temperature dependence of the optical properties of VO$_2$ deposited on sapphire with different orientations. Physical Review B, 87(3), 035142.

[16] Théry, V., Boulle, A., Crunteanu, A., Orlianges, J. C., Beaumont, A., Mayet, R., & Fabert, M. (2016). Role of thermal strain in the metal-insulator and structural phase transition of epitaxial VO$_2$ films. Physical Review B, 93(18), 184106.

[17] Yang, T. H., Aggarwal, R., Gupta, A., Zhou, H., Narayan, R. J., & Narayan, J. (2010). Semiconductor-metal transition characteristics of VO$_2$ thin films grown on c-and r-sapphire substrates. Journal of Applied Physics, 107(5), 053514.

[18] Houska, J., Kolenaty, D., Rezek, J., & Vlcek, J. (2017). Characterization of thermochromic VO$_2$ (prepared at 250°C) in a wide temperature range by spectroscopic ellipsometry. Applied Surface Science, 421, 529-534.

[19] Qazilbash, M. M., Brehm, M., Andreev, G. O., Frenzel, A., Ho, P. C., Chae, B. G., & Shpyrko, O. G. (2009). Infrared spectroscopy and nano-imaging of the insulator-to-metal transition in vanadium dioxide. Physical Review B, 79(7), 075107.

[20] Thomas, M. E., Joseph, R. I., & Tropf, W. J. (1988). Infrared transmission properties of sapphire, spinel, yttria, and ALON as a function of temperature and frequency. Applied optics, 27(2), 239-245.

[21] Herzinger, C. M., Johs, B., McGahan, W. A., Woollam, J. A., & Paulson, W. (1998). Ellipsometric determination of optical constants for silicon and thermally grown silicon dioxide via a multi-sample, multi-wavelength, multi-angle investigation. Journal of Applied Physics, 83(6), 3323-3336.

[22] Liang, J., Hu, M., Kan, Q., Liang, X., Wang, X., Li, G., & Chen, H. (2011). Infrared transition properties of vanadium dioxide thin films across semiconductor-metal transition. Rare Metals, 30(3), 247.

[23] Qazilbash, M. M., Brehm, M., Chae, B. G., Ho, P. C., Andreev, G. O., Kim, B. J., & Kim, H. T. (2007). Mott transition in VO2 revealed by infrared spectroscopy and nano-imaging. Science, 318(5857), 1750-1753.

[24] Qazilbash, M. M., Schafgans, A. A., Burch, K. S., Yun, S. J., Chae, B. G., Kim, B. J., & Basov, D. N. (2008). Electrodynamics of the vanadium oxides VO$_2$ and V$_2$O$_3$. Physical Review B, 77(11), 115121.

[25] Pop, S. D., Hinrichs, K., Wenmackers, S., Cobet, C., Esser, N. & Zahn, D. R. in Ellipsometry of Functional Organic Surfaces and Films, edited by K. Hinrichs, and K. Eichhorn (Springer, Berlin, 2018).

[26] Meneses, D. D. S., Gruener, G., Malki, M., & Echegut, P. (2005). Causal Voigt profile for modeling reflectivity spectra of glasses. Journal of non-crystalline solids, 351(2), 124-129.

[27] Tompkins, H. G., & Irene, E. A. *Handbook of ellipsometry* (William Andrew, New York, 2005).

[28] Orava, J., Wágner, T., Šik, J., Přikryl, J., Frumar, M., & Beneš, L. (2008). Optical properties and phase change transition in Ge$_2$Sb$_2$Te$_5$ flash evaporated thin films studied by temperature dependent spectroscopic ellipsometry. Journal of Applied Physics, 104(4), 043523.

[29] Kang, L., Gao, Y., Luo, H., Chen, Z., Du, J., & Zhang, Z. (2011). Nanoporous thermochromic VO$_2$ films with low optical constants, enhanced luminous transmittance and thermochromic properties. ACS applied materials & interfaces, *3*(2), 135-138.

[30] Kats, M. A., Sharma, D., Lin, J., Genevet, P., Blanchard, R., Yang, Z., & Capasso, F. (2012). Ultra-thin perfect absorber employing a tunable phase change material. Applied Physics Letters, 101(22), 221101.

[31] Seal, K., Sharoni, A., Messman, J. M., Lokitz, B. S., Shaw, R. W., Schuller, I. K., & Ward, T. Z. (2014). Resolving transitions in the mesoscale domain configuration in VO$_2$ using laser speckle pattern analysis. Scientific reports, 4, 6259.

[32] Gomez-Heredia, C. L., Ramirez-Rincon, J. A., Ordonez-Miranda, J., Ares, O., Alvarado-Gil, J. J., Champeaux, C., & Joulain, K. (2018). Thermal hysteresis measurement of the VO$_2$ emissivity and its application in thermal rectification. Scientific reports, 8(1), 8479.

[33] Bruggeman, D. A. G. (1935). DAG Bruggeman, Ann. Phys. (Leipzig) 24, 636 (1935).

 [34] Huffman, T. J., Lahneman, D. J., Wang, S. L., Slusar, T., Kim, B. J., Kim, H. T., & Qazilbash, M. M. (2018). Highly repeatable nanoscale phase coexistence in vanadium dioxide films. Physical Review B, 97(8), 085146.

[35] Carr, G. L., Perkowitz, S., & Tanner, D. B. (1985). Far-infrared properties of inhomogeneous materials. Infrared and millimeter waves., 13, 171-263.

[36] J. D. Jackson, Classical Electrodynamics (John Wiley & Sons, Inc., New Jersey, 2001).

[37] Trotter, D. M., & Sievers, A. J. (1980). Spectral selectivity of high-temperature solar absorbers. Applied optics, 19(5), 711-728.

6. General conclusions

The optical characterization of selective absorption and emission thin films based on metal-oxides useful in solar-to-thermal energy conversion aplications, have been achieve by means of photothermal and ellipsometric spectroscopies. The potential of photothermal techniques in the study of light-into-heat conversion, light scattering as well as emissivity at a surface and heat propagation in several materials was explored. Additionally, using ellipsometry, information carried out by polarized light after being reflected by the surface of vanadium dioxide along its phase transition was studied.

Using photothermal techniques, solar selective coatings of nickel-oxide deposited on stainless steel and copper substrates, as well as titanium-nitride-oxide (TiNOX) deposited on aluminum, have been analyzed by means of a three-dimensional heat propagation model in the modulation frequency range of 3 to 2000 Hz. By using photoacoustic spectroscopy (PAS) and photothermal radiometry (PTR) in the modulation frequency range where the metallic substrate is thermally thick and presents one-dimensional heat propagation, the relative light-into-heat conversion factors at 808 nm have been determined. This approach also provided the average emissivity of the selective coatings in the infrared spectral range of 2 to 12 μm. These last results showed a

very good agreement with those obtained by FTIR reflectance spectroscopy, indicating that this methodology can be a good alternative for measuring optical properties of selective coatings of relevance in solar thermal energy systems.

On the other hand, the phase transition from insulator to metal of vanadium dioxide (VO_2) thin films deposited on sapphire has been monitored by using PTR in the temperature range of 20 to 80ºC. Both photothermal signals showed a strong dependence with the structural transition from monoclinic (M1) at room temperature to rutile (R) at $T > 65°C$. It was shown that due to the inhomogeneity of the surface in the intermediate state, scattering effects appeared, which also are associated to structural morphology such as observed with solar selective coatings. Even though photothermal radiometry allows to observe the phase transition, up to now we do not have thermal wave theoretical framework at hand to perform the adequate analysis of such transition. In view of these facts we therefore resorted to a purely optical technique to analyze the metal semiconductor phase transition.

By means of visible-IR ellipsometry for wavelengths ranging from 0.4 to 15 μm and temperatures within its phase transition, the complex dielectric function of VO_2 thin films has been determined. The measurements were analyzed using a combination of Tauc-Lorentz, Gaussian, and Drude oscillators. The real and imaginary part of the dielectric function of VO_2 showed the typical behavior for dielectric (high transmittance) and metallic (IR opaque) materials at low and high temperatures, respectively. Additionally, the effective medium theory was used to determine the volumetric metallic fraction in the sample, and it has been shown that this model is suitable to describe the VO_2 dielectric function for wavelengths smaller than 3 μm mainly. Finally, by means of Fresnel equations and Kirchhoff's law the emissivity values ware obtained across the transition, exhibiting a hysteresis loop and a difference in a factor of three between its insulating and metallic phases.

Perspectives

Based on the results and conclusions of the work developed during the PhD studies, there are some theoretical and experimental aspects that can be explored, in order to get a deeper understanding of the results obtained with photothermal techniques in the chacterization of thin films and composite materials.

Multi reflection effects:

In the case of semitransparent thin films, part of the incident light travels through the sample to the substrate, where it is reflected, returning to the thin film surface. This phenomenon generates an optical interference effect at low modulation frequencies, which can be analyzed from the mathematical model, considering the adequate heat energy source. This can be potentially used to obtain the optical absorption coefficient of a thin film deposited on opaque substrate.

Spectral absolute light-into-heat-conversion efficiency:

By using photoacoustic spectroscopy, it has been shown that the ratio of conversion of light-into-heat between the coating and substrate has a dependence on the structural characteristics of each surface (dielectric or metal) and the incident wavelength. Therefore, to obtain absolute values for the quantum efficiency at any wavelength for a specific thin film, the photothermal signals must be normalized with the ones obtained for a black thin film (perfect absorption)

deposited on the same substrate than the sample, to avoid any influence of the thermal properties.

<u>Characterization of composite surfaces:</u>

In chapter 4, it has been shown that photothermal radiometry technique is useful to monitoring in real time the insulator-to-metal phase transition of vanadium dioxide thin films. At the intermediate state, when the sample is composed of dielectric and metallic islands in equal parts, amplitude and phase signals present abrupt changes associated to scattering effects due to the different mechanism of emission at the surface. This scattering decreases as the sample tends to be completely metallic or dielectric. Taking this into account, the photothermal signals could be used along with the effective medium theory to predict the evolution of the volumetric fraction of metal across the phase transition.

List of publications

- Ramírez-Rincón, J. A., Ares-Muzio, O., Macias, J. D., Estrella-Gutiérrez, M. A., Lizama-Tzec, F. I., Oskam, G., & Alvarado-Gil, J. J. (2018). On the use of photothermal techniques for the characterization of solar-selective coatings. Applied Physics A, 124(3), 252.

- J. A. Ramirez-Rincon, C.L. Gomez-Heredia, A. Corvisier, J. Ordonez-Miranda, T. Girardeau, F. Paumier, C. Champeaux, F. Dumas-Bouchiat, Y. Ezzahri, K. Joulain, O. Ares & J. J. Alvarado-Gil (2018). Thermal hysteresis measurement of the VO_2 dielectric function for its metal-insulator transition by visible-IR ellipsometry. Journal of Applied Physics, **124**, 195102.

- Gomez-Heredia, C. L., Ramirez-Rincon, J. A., Ordonez-Miranda, J., Ares, O., Alvarado-Gil, J. J., Champeaux, C., & Joulain, K. (2018). Thermal hysteresis measurement of the VO_2 emissivity and its application in thermal rectification. Scientific reports, 8(1), 8479.

- Macias, J. D., Rincon, J. A. R., Tzec, F. I. L., Muzio, O. E. A., Oskam, G., Gomez, R. D. C., & Gil, J. J. A. (2014, November). Optical and Thermal Characterization of High Reflective Surface with Applications in Thermal-Solar Technology. In Latin America Optics and Photonics Conference (pp. LM4A-7). Optical Society of America.

- Tabasco-Novelo, C., May-Crespo, J., Ramírez-Rincón, J. A., Forero-Sandoval, I. Y., Rodríguez-Gattorno, G., Quintana, P., & Alvarado-Gil, J. J. (2018). Effects of Sintering on the Thermal and Optical Properties of Zinc Oxide Ceramic. International Journal of Thermophysics, 39(2), 22.

- G. Hamaoui, N. Horny, C. L. Gomez-Heredia, J. A. Ramirez-Rincon, J. Ordonez-Miranda, C. Champeaux, F. Dumas-Bouchiat, J. J. Alvarado-Gil, Y. Ezzahri, K. Joulain, & M. Chirtoc, Thermophysical characterisation of VO_2 thin films hysteresis and its application in thermal rectification, *Under review*.